X-ray structural characterization of individual as-grown GaAs/(In,Ga)As/(GaAs) based core-multi-shell nanowires

Naturwissenschaftlich Technische Fakultät

Dissertation
zur Erlangung des Grades eines Doktors der Naturwissenschaften

vorgelegt von
M. Sc. Ali Al Hassan

eingereicht bei der Naturwissenschaftlich-Technischen Fakultät
der Universität Siegen

January 22, 2020

Gutachter:

Prof. Dr. Ullrich Pietsch

Prof. Dr. Olivier Thomas

Tag der mündlicher Prüfung: 29.10.2019

Prüfer:

Prof. Dr. Ullrich Pietsch

Prof. Dr. Olivier Thomas

Prof. Dr. Carsten Busse

Prof. Dr. Markus Risse

List of papers

Paper I

P. Schroth, M. Al Humaidi, L. Feigl, J. Jakob, **A. Al Hassan**, A. Davtyan, H. Küpers, A. Tahraoui L. Geelhaar, U. Pietsch, and T. Baumbach. "Impact of the shadowing effect on the crystal structure of patterned self-catalyzed GaAs nanowires". *Nano Lett.*, 2019. Doi

Paper II

J. Lähnemann, M. O. Hill, J. Herranz, O. Marquardt, G. Gao, **A. Al Hassan**, A. Davtyan, S. O. Hruszkewycz, M. V. Holt, C. Huang, I. Calvo-Alaman, U. Jahn, U. Pietsch, L. J. Lauhon, and L. Geelhaar. "Correlated study of the emission from wurtzite versus zincblende (In,Ga)As/GaAs nanowire core-shell quantum wells". *Nano Lett.*, 2019. Doi

Paper III

A. Al Hassan, R. B. Lewis, H. Küpers, D. Bahrami, T. Krause, D.Salomon, A.Tahraoui, M. Hanke, L. Geelhaar and U. Pietsch. "Determination of indium content of GaAs/(In,Ga)As/(GaAs) core-shell(-shell) nanowires by X-ray diffraction and nano X-ray fluorescence". *Journal of Physical Review Materials*, 2018. Doi

Paper IV

A. Al Hassan, A. Davtyan, H. Küpers, R. B. Lewis, D. Bahrami, F. Bertram, G. Bussone, C. Richter, L. Geelhaar and U. Pietsch. "Complete structural and strain analysis of single GaAs/(In,Ga)As/GaAs coreshellshell nanowires by means of in-plane and out-of-plane X-ray nano-diffraction". *Journal of Applied Crystallography*, 2018. Doi

Paper V

A. Davtyan, V. Favre-Nicolin, R. Lewis, H. Küpers, L. Geelhaar, D. Kriegner, D. Bahrami, **A. Al Hassan**, and U. Pietsch. "Coherent X-ray diffraction imaging meets ptychography to study core-shell-shell nanowires". *MRS Advances*, 2018. Doi

Paper VI

A. Davtyan, S. Lehmann, D. Kriegner, R. R. Zamani, K. A. Dick, D. Bahrami, **A. Al Hassan**, S. J. Leake, U. Pietsch and V. Holý. "Characterization of individual stacking faults in a wurtzite GaAs nanowire by nanobeam X-ray diffraction". *Journal of Synchrotron Radiation*, 2017. Doi

Paper VII

A. Davtyan, T. Krause, D. Kriegner, **A. Al Hassan**, D. Bahrami, S. M. Mostafavi Kashani, R. B. Lewis, H. Küpers, A. Tahraoui, L. Geelhaar, M. Hanke, S. J. Leake, O. Loffeld and U. Pietsch. "Threefold rotational symmetry in hexagonally shaped coreshell (In,Ga)As/GaAs nanowires revealed by coherent X-ray diffraction imaging". *Journal of Applied Crystallography*, 2017. Doi

Paper VIII

T. Rieger, P. Zellekens, N. Demarina, **A. Al Hassan**, F. J. Hackemüller, H. Lüth, U. Pietsch, T. Schäpers, D. Grützmacher and M. I. Lepsaa. "MBE growth of Al/InAs and Nb/InAs superconducting hybrid nanowire structures". *Nanoscale*, 2017. Doi

Paper IX

A. Al Hassan, J. Lähnemann, S. Leake, H. Küpers, M. Niehle, D. Bahrami, F. Bertram, R. B. Lewis, A. Davtyan, A. Trampert, L. Geelhaar, U. Pietsch. "Enhanced Optical emission correlated with a mixed crystal phase in single as-grown core-multi-shell nanowires". *Submitted*, 2019.

Paper X

A. Al Hassan, J. Lähnemann, A. Davtyan, J. H. Zamorano, D. Bahrami, F. Bertram, L. Geelhaar, U. Pietsch. "Beam damage of single semiconductor nanowires during X-ray nano beam diffraction experiment". *Submitted*, 2019.

Paper XI

D. Bahrami, S. M. Mostafavi Kashani, **A. Al Hassan**, A. Davtyan, U. Pietsch. "High yield of self-catalyzed GaAs nanowire growth on silicon (111) substrate templated by focused ion beam patterning". *Submitted*, 2019.

Paper XII

A. Algashi, A. Abboud, M. Shokr, A. Tosson, **A. Al Hassan**, M. Klaus, C. Genzel, L. Strüder, U. Pietsch. "Application of polychromatic hard X-rays for energy-dispersive Laue diffraction to analyze GaAs/(In,Ga)As/GaAs core-shell nanowires using pn-CCD detector". *Submitted*, 2019.

Contents

Acronyms

Abbreviation/Definition

NW	Nanowire
nXRD	Nano- X-ray diffraction
nXRF	Nano- X-ray Fluorescence
QW	Quantum well
CL	Cathodoluminescence
RSM	Reciprocal space map
VLS	Vapor-liquid-solid
MBE	Molecular beam epitaxy
ZB	Zincblende
WZ	Wurtzite
SAG	Selective area growth
EBL	Electron beam lithography
FIB	Focused ion beam
SEM	Scanning electron microscopy
TEM	Transmission electron microscopy
ESRF	European synchrotron radiation facility
DESY	Deutsche electron synchrotron
EDX	Energy-dispersive X-ray spectrometry

Zusammenfassung

Dank der herausragenden Innovationen der letzten Jahre auf dem Gebiet der Röntgenoptiken, wie z.B. der Fresnel Zonenplatten und Kirkpatrick-Baez Spiegelsystemen, kann man heute intensive Röntgenstrahlung auf eine SpotgröSSe von hundert Nanometer und weniger fokussieren. Unter Berücksichtigung spezifischer Methoden der Probenpräparation, wie dem Wachstum auf vorstrukturierten Oberflächen, konnten so neuartige Röntgenbeugungsmethoden zur Untersuchung einzelner Nanoobjekten, wie auch Nanodrähten, entwickelt werden. Bisher wurde vor allem die Transmissionselektronenmikroskopie zur Bestimmung der Dicke, Kristallphase und Elementeverteilung in einzelnen Kern- Mantel Nanodrähten verwendet. Diese Parameter, wenn sie präsise kontrolliert werden, spielen im Prozess der Optimierung der optischen Emission von Nanodraht basierten Bauelementen eine herausragende Rolle. In der vorliegenden Arbeit demonstrieren wir einen neuen Weg der vollständigen Charakterisierung individueller GaAs/(In,Ga)As/GaAs Kern-Mantel Nanodrähten in ihrer Position auf dem Substrat unter Verwendung der Röntgen-Nanodiffraktion, inklusive der Korrelation ihrer strukturellen und optischen Eigenschaften.

In einem ersten Schritt wurde die räumliche Verteilung von Indium in der (In,Ga)As Schale einzelner GaAs/(In,Ga)As basierter Kern-Mantel Nanodrähte mittels nano-fokussierter Scanning-Röntgen Fluoreszenzmikroskopie bestimmt. Im Gegensatz zur energie-dispersiven Röntgenspektroskopie in Transmissionselektronenmikroskopen kann man mittels nanoTRF mehrere Nanodrähte in

ihrer Position auf dem Substrat sehr schnell und ohne vorherige Probenprä-
paration untersuchen.

In einem zweiten Schritt wurde die hochauflösende Röntgen- Nanodiffrak-
tion verwendet, um die strukturellen Eigenschaften einzelner, mit Hilfe der
Vapour-Liquid-Solid Epitaxie gewachsenen, GaAs/(In,Ga)As/GaAs Kern-
Mantel Nanodrähte parallel und senkrecht zur [111] Wachstumsrichtung ver-
messen. Damit war es möglich, die Dicke des Kerns und der Schalen und
den Nanodrahtquerschnitt zu bestimmen , was bisher nur mittels Elektro-
nenmikroskopie an der Nanodraht Basalflächen möglich war.

In einem dritten Schritt verfolgten wir mittels Scanning Röntgendiffrak-
tometrie den GaAs 111 Bragg Reflex, um die Verteilung der verschiede-
nen Polytype entlang der Wachstumsachse einzelner Nanodrähte zu bestim-
men. Die gemessene Phasenverteilung wurde mit der Ortsabhängigkeit der
Kathodolumineszenz korreliert. Es zeigte sich, dass die räumliche bestimmte
Erhöhung der optischen Lumineszenz mit einer aus Zinkblende, verzwill-
ingter Zinkblende und Wurtzite Einheiten gemixten Phase zusammenfällt,
die auSSerdem Defektebenen und Stapelfehler enthalten.

Zuletzt bestimmten wir die strukturelle und optische Degeneration als Funk-
tion der absorbierten Strahlungsdosis in einzelnen Halbleiter Nanodrähten,
die bisher als Strahlungsresistent galten. Die beschriebenen Schäden waren
nur dann nachweisbar, wenn ein Nanostrahl über längere Zeit die gleiche Po-
sition auf der Achse des Nanodrahtes beleuchtete. Unsere Erkenntnisse soll-
ten in zukünftigen zeitintensiven Röntgenbeugungsexperimenten mit Nanos-
trahlen Berücksichtigung finden.

Abstract

In recent years, owing to the major development of X-ray focusing optics such as fresnel zone plates and Kirkpatrick-Baez mirrors, highly intense and collimated X-ray beams with spot sizes in the range of a hundred nanometers and below can be achieved. Together with proper sample preparation such as selective area growth, X-ray diffraction techniques can be deployed to study single nanometer-sized objects, in particular nanowires. Typically, transmission electron microscopy based methods are used to investigate the thickness, crystal phase and alloy distribution in individual core-shell nanowires. These properties, if controlled precisely, play the key role in optimizing the optical emission of NW based devices. Nevertheless, in this work, using X-ray nano diffraction based techniques we demonstrate a new path to achieve the complete structural characterization of individual as-grown GaAs/(In,Ga)As/GaAs based core-shell nanowires in addition to correlating their phase structure to their optical properties.

In a first step, the spatial distribution of the In alloy within the (In,Ga)As shell of individual GaAs/(In,Ga)As based core-shell nanowires is inspected by means of nano-focused scanning X-ray fluorescence microscopy. In contrast to energy dispersive X-ray spectroscopy in transmission electron microscopy, using this fast probing technique one can probe several nanowires in their as-grown geometry without the need of a complicated sample preparation procedure.

In a second step, high resolution X-ray nano diffraction is applied along and perpendicular to the NW [111] growth direction to measure the structural properties of individual GaAs/(In,Ga)As/GaAs core-shell nanowires grown by vapor liquid solid epitaxy. There, we were able to calculate the thickness of the core and shells and therefore reconstruct the full NW cross-section which is forever done by means of transmission electron microscopy of the nanowire basal plane.

In a third step, monitoring the GaAs 111 Bragg reflection, scanning X-ray diffraction microscopy was used as a fast scanning technique to reveal the polytype distribution along the growth axes of several individual core-multi-shell nanowires. The phase distribution was then correlated with cathodoluminescence measurements revealing an enhancement in the optical emission of a mixed phase formed of the cubic zinc blende crystal phase and its twin, the hexagonal wurtzite polytype and slabs of defects and stacking faults.

Finally, we reveal induced structural and optical damage of individual semiconductor nanowires, that are supposed to be resistant to radiation, for a threshold absorbed X-ray dose. This was demonstrated only for measurements that require fixing the X-ray nano beam to the same position along the nanowire growth axis. This study will spreads awareness regarding time consuming X-ray diffraction measurements performed on nano-structures.

Chapter 1

Introduction

'Nanotech holds key to the future'

The fact that one day we will be able to manipulate matter at the atomic scale and build structures and devices with atomic scale precision, inspires me as a nanomaterials scientist. It is also the fact that this is pretty much the last frontier in material manipulation - Pulickel Ajayan

One way of fabricating semiconductor nanowires (NW) is the bottom-up technology, where molecules and particles self-assemble, atom by atom, to form a specific structure. Using this approach, NWs can be grown using the so-called self-assisted technique in which the seed particle, which initiates the NW growth process, is formed by the NW material, for example Ga and As in the case of GaAs NWs. Due to their high aspect ratio, NWs are one-dimensional objects that typically grow up to a couple of hundred nanometers in diameter and few microns in length. Due to their high surface to volume ratio, radial strain relaxation takes place and allows for the growth of defect free but lattice-mismatched core shell NW hetero-structures.

Unlike bulk systems adapting the stable zincblende (ZB) phase, semiconductor NWs, regardless if homo- or hetero-structures, may grow with different

crystal structures, mainly ZB and/or wurtzite (WZ). As the two polytypes have different band gaps [1,2], a change in the crystal structure would directly modify the band structure of the material. Therefore, a controlled polytypism would help to manipulate and thus to optimize the optical properties of NW based devices. Switching between the two polytypes is, to a certain extent, feasible by varying specific growth parameters, e.g. the temperature, source-material flux or impurities [3–8]. Immense research has also shown that the phase configuration of the NW depends on the contact angle between seed droplet and the underlying NW interface [9–13]. Nevertheless, the stability of the polytype distribution and physical mechanisms behind switching is still under investigation i.e. different individual NWs grown under the same conditions on the same substrate may possess different crystal phases and structural parameters e.g. diameter and hexagonal symmetry [14]. Therefore, the structural to optical properties should be correlated at the level of single NWs instead of NW ensembles.

Another factor that influences the optical properties of core-shell NW systems is the thickness variation in core or shell(s), as demonstrated by Dimakis et. al. 2014 for GaAs/(In,Ga)As/GaAs NWs [15]. A conventional imaging technique to investigate the polytype distribution [16] and thicknesses [17, 18] in single core-shell NWs is transmission electron microscopy (TEM). However, regardless of the atomic resolution, high precision and direct real space information, this technique can only probe a very thin cross section and often requires invasive sample preparation. On the one hand, planar lamellae of the basal plane, which is required to access the thickness of core and shell(s), can be performed at only one position along the NW growth axis and, moreover, demands the removal of the NW from the substrate. On the other hand, preparing cross-sectional lamellae to inspect the polytype distribution along the NW growth axis demands slicing the NW down to less than a hundred nanometers in order to obtain atomic resolution. Furthermore, it can be very

complicated to apply this technique to "specific" semiconductor NWs that are only couple of micrometers in length. A less destructive probing technique is X-ray diffraction (XRD) using a nano focused beam where one can probe the three-dimensional (3D) internal structure of the NWs [19, 20].

In this work, we investigate these properties in single core-multi-shell NWs using synchrotron based nano focused X-ray diffraction (nXRD) in the as-grown geometry. At the same time, obstacles and technical limitations will be discussed in details. The outline of this thesis is as following:

- The basic concepts concerning crystal phase structure and growth of semiconductor NWs and the scanning modes used experimentally i.e. Bragg reciprocal space mapping (RSM), nano- X-ray fluorescence (nXRF), cathodoluminescence (CL) and scanning X-ray diffraction microscopy (SXDM) are briefly discussed in Chapters 2 and 3.

- In Chapter 4, we report on measurements of radial and axial reflections of NW ensembles by XRD, from which we were able to calculate the average QW thickness and In content of GaAs/(In,Ga)As/(GaAs) core-shell-(shell) NWs. The latter was combined with nXRF acquired from single NWs in order to investigate the In homogeneity and fluctuations with a resolution $< 1\%$.

- Chapter 5 highlights the possibility to reconstruct the core-shell-shell dimensions of individual GaAs/(In,Ga)As/GaAs NWs and to estimate the In content and strain at each side facet with accuracy of 2 nm in thickness and 2% of In content, respectively. This was done by replicating the experimentally measured reciprocal space maps (RSM) of the $2\bar{2}0$ and $22\bar{4}$ Bragg reflections using finite element methods of a NW model with unique dimensions of core and shells.

- Chapter 6 is dedicated to the direct correlation between the structural and optical properties of AlAs/GaAs capped GaAs/(In,Ga)As/GaAs

single core-multi-shell NWs. The first is measured by nXRD whereas the second is measured by CL. An enhancement in the CL emission up to a factor of 80 was observed below the mid-section of the NWs and was attributed to a mixture of the ZB, TZB and WZ polytypes and stacking defects.

- The work presented in Chapter 7 was motivated by the beam damage which was visible for few NWs that have been heavily exposed in the experiment presented in Chapter 6. This chapter demonstrates the impact of the absorbed X-ray dose on the structural morphology and the optical properties of single NWs.

The characterization tools listed in Chapters 4, 5, 6 and 7 were all performed in the as-grown geometry i.e. the contact between the substrate and the NWs was never lost.

Note that, the work presented in Chapters 3, 4, 5 and 6 is based on papers III, IV, IX and X, respectively.

Chapter 2

Nanowires growth and structure

2.1 Nanowire crystal structure and growth

As mentioned in the introduction, NWs are usually fabricated using the bottom-up technique where atoms self-assemble periodically layer by layer to form the 3D crystal lattice which defines the crystal structure of the NW. A change in the repeating pattern will thus change the crystal structure. Regardless of the lattice mismatch at the interface between the template and the NWs on top, epitaxial growth of the NWs takes place. All NWs investigated in this work have been grown at the Paul-Drude-Insitute in Berlin using the Ga-assisted vapor-liquid-solid (VLS) mechanism in molecular beam epitaxy (MBE). In this chapter, basic concepts regarding NW growth, phase structure, Bragg diffraction and strain will be briefly discussed.

2.1.1 Crystal structure

In contrast to bulk semiconductor materials which adapt the ZB crystal structure, 1D semiconductor NWs grow mainly in the cubic ZB with an atomic stacking of ABCABC- [6, 21, 22] and/or the hexagonal ABABAB-stacked WZ phases [6, 23, 24] but usually stacking faults [25] and inclusions of twin planes [26, 27] and intermediate phases like 4H (ABCB-) [28] or a mixture of ZB and WZ (M phase) [29] may modify the crystal structure.

The unit cells and atomic stacking sequences of ZB and WZ are illustrated in Figures 2.1 and 2.2, respectively. Regardless if in pure cores or core-shell III/V semiconductor NWs, ZB to WZ transformation or vice-versa can easily occur [16]. The two polytypes differ in their stacking sequences [30], lattice parameters and band gaps [1, 2].
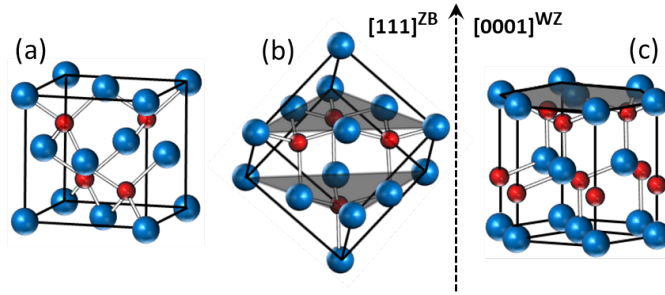
Figure 2.1: (a,b) GaAs Fcc unit cell in two different orientations. Red and blue spheres represent groups V and III, respectively. (c) GaAs WZ unit cell. Planes colored in light black represent the 111 ZB and 0001 WZ lattice planes

Figure 2.2: (a,b) ZB [ABCABC-], WZ [ABAB-] and 4H [ABCB-] atomic stacking from top and side views.

Figure 2.3, taken from Sourribes et al. 2014 [30], shows respective TEM micrographs of ZB, WZ and their rotational twins, in addition to few possible stacking faults that can exist in both polytypes. The authors have traced the atomic stacking sequences and have marked them using black lines with

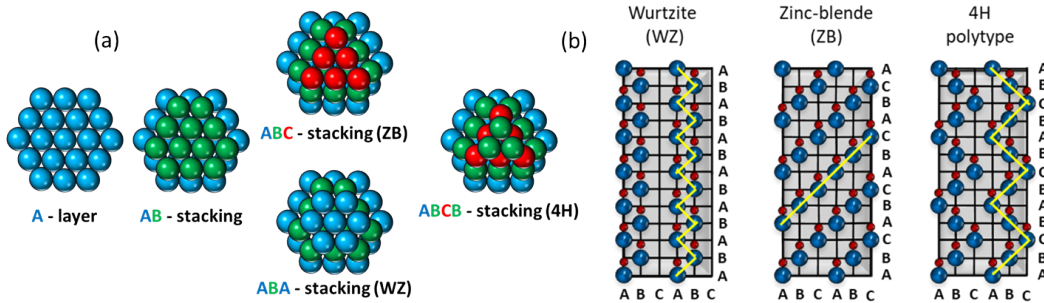dots labeled by A, B and C in correspondence to atomic layers. For example, a twin occurs when there is a misplaced stacking in ZB resulting in a ABC$\underline{A}$CBA sequence which changes direction mirroring the previous stacking sequence with a twin plane $\underline{A}$ at the boundary.
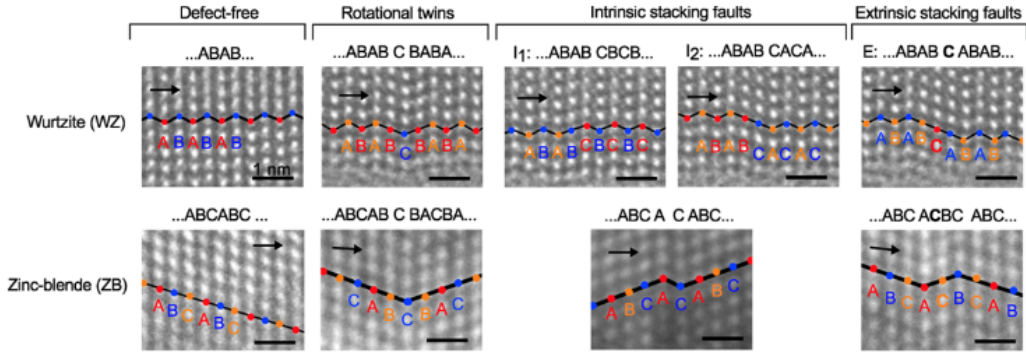

Figure 2.3: TEM images showing stacking sequences of WZ and ZB including rotational twins and stacking faults in InAs and InAsASb NWs.

The opto-electronic properties of different polytypes may alter depending on the segment length and distribution of the polytypes as WZ/ZB segments in the NWs may form type I or type II band alignment (Figure 2.4). For example, in type I, electrons and holes localize at the lower band gap material whereas type II should provide better optical proper-

Figure 2.4: (a) HAADF HRSTEM micrograph of a ZB quantum well in a WZ segment. (b) An atomistic model of a WZ/ZB/WZ heterostructure along with a schematics of the band diagram [97].

ties since electrons and holes could be dragged into opposite directions which decreases the probability of electron-hole recombination. Therefore, the direct correlation of structural and optical properties of different polytypes from the same NW would be essential for rational synthesis of nanomaterials and band gap engineering with predefined structure and functionality.
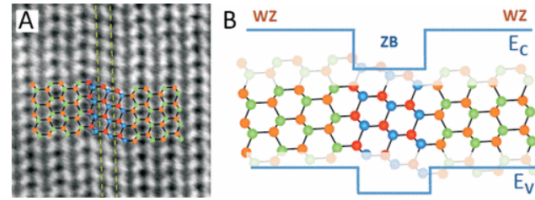
2.1.2 Nanowire growth technique used

Most III-V NW epitaxy are performed by the VLS process, either in MBE or metal organic vapor phase epitaxy, originally suggested and investigated several decades ago by Wagner and Ellis [31]. Self-catalyzed VLS growth of NWs is favored in order to avoid incorporation of impurities at the sidewalls which may deteriorate the opto-electronic properties of the NWs. For example, to synthesize GaAs NWs, beams of Ga and As atoms are directed towards the wafer, where they adsorb and dissolve in the Ga droplets. When supersaturation inside the droplets is reached and due to the difference in the chemical potential between the droplets and the substrate, the NWs begin to form layer by layer below the droplets extending the axial length of the NW, whereby the droplets are gradually pushed upwards (Figure 2.5e). The droplet, located at the NW tip, serves as a seed for NW growth and its diameter also determines the NW diameter.

Using substrates covered with a native oxide layer, the droplets adsorb at randomly located openings, which serve as nucleation centers for NWs, i.e. the growers have no control on the positions and diameters of the NWs (Figure 2.5a,b). An alternative approach of growing NWs with maximized control of both aspects is selective-area growth (SAG) where electron beam lithography (EBL) [15, 32–34] or a focused ion beam (FIB) [35–37] can be used to create holes with predefined diameters, depth and positions on the substrate (Figure 2.5c,d). An example of NWs grown on a substrate with native oxide is displayed in the SEM micrograph in Figure 2.6a. The respective sample is investigated in Chapter 4. It can be clearly seen that the NW density is not homogeneous along the surface of the substrate. Quadratic NW fields with different hole diameter and NW densities are demonstrated in Figure 2.6b i.e. a zoom in of the NW field with 10 µm separation between neighboring NWs is shown in Figure 2.6c. NWs can also be selectively grown in the form of a straight line which can allow for single NW diffraction measurements

using nano-focused X-rays (Figure 2.6d).
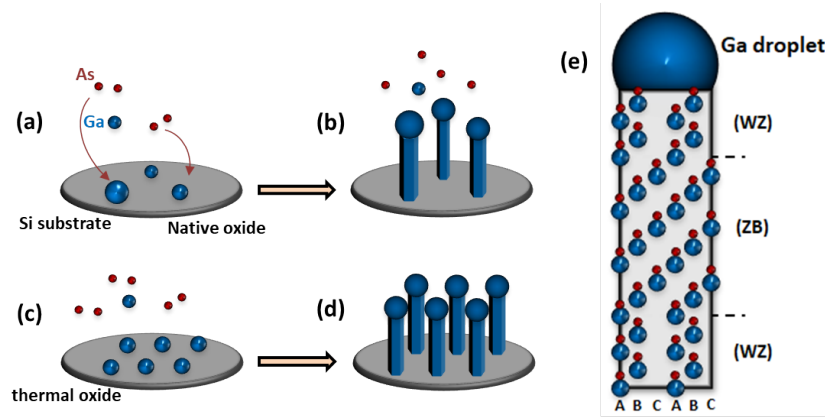
Figure 2.5: Animations (a,b) and (c,d) illustrate the NW growth procedure on Si substrates with native and thermal oxide layers using the self-assisted VLS growth mechanism, respectively. (e) Side view scheme of a NW composed of WZ and ZB polytypes.
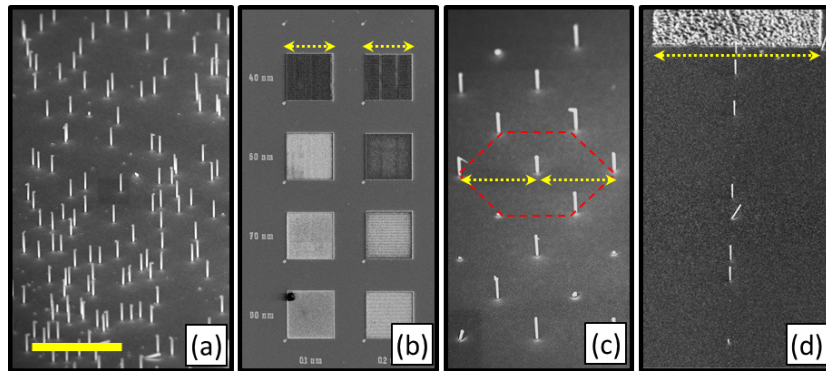
Figure 2.6: (a) NW growth on native oxide Si 111 substrate. (b) SAG quadratic NW fields. (c) SAG NW growth with hexagonal pattern, marked by a red dotted hexagon. (d) selective NW growth along a straight line. The scale bar in (a) and the arrows in (b,c,d) are 15, 100, 10 and 50 µm, respectively.

2.2 Atomic planes in a crystal

The 3D periodic arrangement of lattice points in a crystal defines lattice planes i.e. the orientation of a lattice plane is characterized by its Miller

indices [hkl].

The recipe to obtain these indices is first to determine the intercepts of the plane with the crystal axes in terms of the unit cell vectors $\vec{a}_1$, $\vec{a}_2$ and $\vec{a}_3$. Second, to take the reciprocal of these values and to find integers hkl having the same ratio. A lattice plane parallel to one of the crystal axes holds a corresponding index of 0. Exemplary planes of a cubic crystal, colored in red and green, are demonstrated in Figure 2.7. The distance between two subsequent planes with Miller indices hkl can be calculated, if the lattice constants and type of the underlying Bravais lattice are known. For the cubic and hexagonal lattice, the distances can be calculated according to
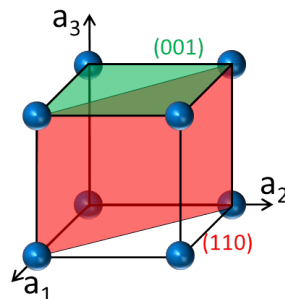
Figure 2.7: Lattice planes and their Miller indices.

$$d^c_{hkl} = \frac{a}{\sqrt{h^2 + k^2 + l^2}} \tag{2.1}$$

$$d^h_{hkl} = \frac{a}{\sqrt{\frac{4}{3}(h^2 + hk + k^2) + (\frac{a}{c})^2 \, l^2}} \tag{2.2}$$

2.2.1 Bragg condition

When monochromatic X-rays with wavelength comparable to atomic spacing irradiate a crystalline system at the Bragg angle, it undergoes constructive interference i.e. Bragg diffraction occurs (Figure 2.8). When the scattered waves of X-rays interfere constructively, they remain in phase since the difference between the path lengths of the two waves is equal to an integer multiple of the wavelength. The path difference between two waves undergoing interference from consecutive planes is given by $2d \sin\theta$, where θ is

the scattering angle. This leads to Bragg's law, which is a measure of the interplanar spacing, d, of a crystal lattice.

$$n\lambda = 2d_{hkl} \sin\theta \qquad (2.3)$$
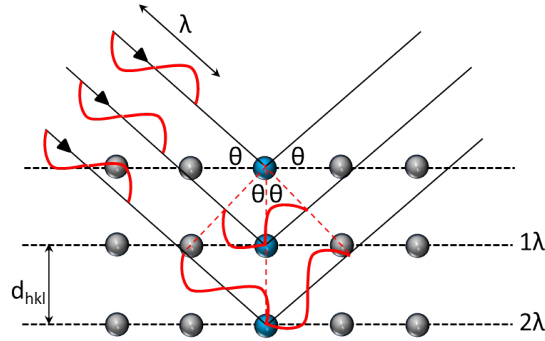
Figure 2.8: Braggs law in an animation. Spheres and red lines represent lattice points and X-rays, respectively. θ is the angle between the incident beam and the crystal planes.

Fulfilling the Bragg condition using XRD, each set of lattice planes is represented by a Bragg reflection in reciprocal space, where the latter one is the Fourier transformation of real space. Rocking the lattice planes around the Bragg angle, the respective Bragg reflection can be recorded, using modern day 2D pixel detectors, and plotted as a function of real space angular coordinates, namely the incident and scattering angles. To avoid confusion, the scattering vector in reciprocal space, measured normal to the lattice planes, will be denoted by Q_z in all what follows and is related to real space d_{hkl} by,

$$Q_z = 2\pi/d_{hkl} \qquad (2.4)$$

This, for example, calculates $Qz = 2.0038 \, \text{Å}^{-1}$ and $1.92505 \, \text{Å}^{-1}$ for the 111 Bragg reflections of unstrained Si and GaAs, respectively. A variation in the Q_z position of a certain reflection gives direct evidence of a variation in the d-spacing of the respective lattice planes.

2.2.2 Axial and radial strain

Due to their high surface to volume ratio, NWs can accommodate strain more efficient than planar structures [38], paving the way for radial hetero-structures that can be formed from lattice-mismatched materials. With the help of nano-focusing optics and instrumentation [39–43], there exist various setups to study the strain state and crystal structure of NWs using XRD. However, throughout all experiments that will be reported in this thesis, a monochromatic beam was used i.e. the wavelength of radiation is fixed and the scattering angle is varied in order to observe diffraction peaks corresponding to reflections from different crystallographic planes, mainly along and perpendicular to the NW growth axis. Fulfilling the Bragg condition and using eqs. 2.3 and 2.4, one can determine the interplanar distance represented by the respective reflection in reciprocal space.

In this work, we investigate the structural parameters, crystal structure and strain behavior of various core-multi-shell NW systems in their as-grown geometry, mainly GaAs/$In_{0.15}Ga_{0.85}As$/GaAs NWs (Figure 2.9b). For unstrained GaAs and $In_{0.15}Ga_{0.85}As$, two Bragg reflections would be visible in Q_z (see Figure 2.9a). However, for a lattice mismatch of $\approx 1.1\%$ between GaAs and $In_{0.15}Ga_{0.85}As$, pseudomorphic growth is expected along the NW growth axis i.e. both materials share the same axial lattice parameter. Therefore, both NW materials will be represented by one Bragg reflection in reciprocal space (Figure 2.9c). Due to energy mass conservation, the compressive and tensile axial strains acting on (In,Ga)As and GaAs are minimized by opposite strains in radial direction, respectively (Figure 2.9d).
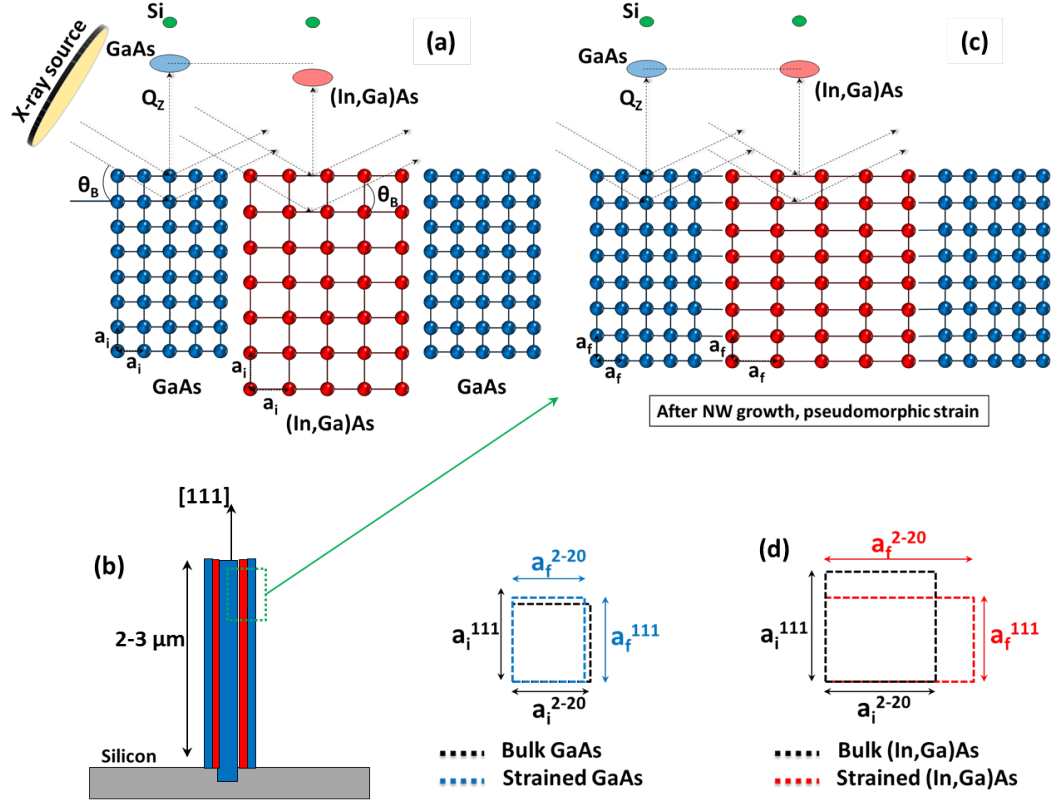
Figure 2.9: Animation (a) crystal lattices of unstrained GaAs and (In,Ga)As, marked by blue and red spheres, respectively, i.e. the lattice parameters of both materials are denoted by a_i. Si, GaAs and (In,Ga)As Bragg reflections are represented by green, blue and red circles, respectively. (b) Scheme of a single core-shell-shell NW from side view. (c) marked by a green dotted rectangle in (b) showing pseudomorphic growth i.e. the lattice parameters of both materials are denoted by a_f. (d) 2D unit cells of the two materials. Compressive and tensile strain acting on GaAs and (In,Ga)As along the 111 growth direction are faced by opposite strains along the $2\bar{2}0$ direction.

Due to pseudomorphic axial growth, both, the structural composition and the interface strain of the NW are encoded along directions perpendicular to the growth axis. The NW coordinate system is defined in Figure 2.10. To access the structural parameters along the NW c-direction, we recorded 3D RSMs in vicinity of the axial 111 Bragg peak. Structural parameters along the NW a- and b- directions were probed measuring the $2\bar{2}0$ and $22\bar{4}$ Bragg

reflections, respectively (see Figure 2.10 for crystal orientation). The ZB and WZ polytypes having different axial lattice parameters (see Figure 2.1), each is represented by a distinct Bragg peak, 111 for ZB and $000\bar{2}$ for WZ, in reciprocal space.
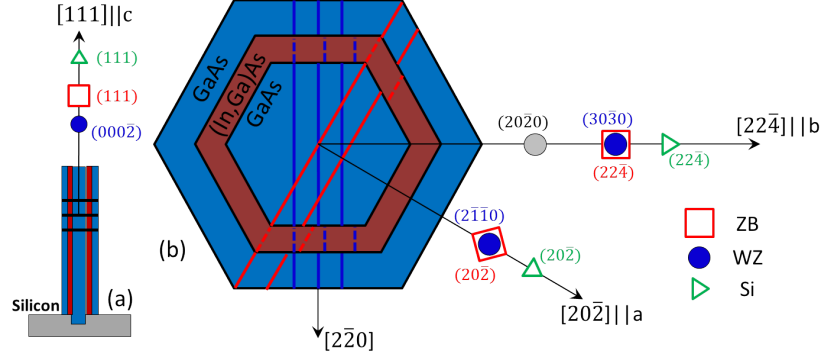
Figure 2.10: Side and top views of a single core-shell-shell NW. Black, red and blue lines represent the 111, $2\bar{2}0$ and $22\bar{4}$ lattice planes, respectively. Si and the NW WZ and ZB Bragg reflections are denoted by green triangles, blue circles and red squares, respectively.

The peak position measured in Q_z can be transformed into the lattice parameter d_{hkl} using equation 2.4. The lattice parameter can be calculated by,

$$d_{111}^{exp} = d_{111}^{(In,Ga)As}V + d_{111}^{GaAs}(1 - V) = d_{111}^{GaAs} + \frac{0.404[\text{Å}]}{\sqrt{3}}xV \qquad (2.5)$$

where $d_{111}^{(In,Ga)As}$ and d_{111}^{GaAs} are the unstrained lattice parameters of (In,Ga)As and GaAs. "x" represents the In content in the (In,Ga)As shell and "V" is the volume fraction of the (In,Ga)As shell within the whole NW, which depends on the shell thickness "t". As pseudomorphic growth is expected and due to the higher GaAs to (In,Ga)As volume fraction, the 111 lattice spacing of the (In,Ga)As shell will be compressed by $\epsilon_{zz}^{(In,Ga)As}$ with respect to $d_{111}^{(In,Ga)As}$ whereas the GaAs core and outer shell parameters will undergo tensile strain

by ϵ_{zz}^{GaAs} with respect to d_{111}^{GaAs}, expressed by

$$d_{111}^{exp} = d_{111}^{(In,Ga)As}(1 + \epsilon_{zz}^{(In,Ga)As}) = d_{111}^{GaAs}(1 + \epsilon_{zz}^{GaAs}) \qquad (2.6)$$

The radial $2\bar{2}0$ lattice parameter of the (In,Ga)As shell will show an expansion $(1 + \epsilon_{xx}^{(In,Ga)As})$ due to the biaxial compressive strain along the [111] and [$22\bar{4}$] directions, ϵ_{zz} and ϵ_{yy}, respectively. Following the notation in Ref. [44], the $2\bar{2}0$ lattice parameter can be expressed as

$$d_{2\bar{2}0}^{(In,Ga)As}(exp) = d_{2\bar{2}0}^{(In,Ga)As}(1 + \epsilon_{xx}^{(In,Ga)As}) = d_{2\bar{2}0}^{(In,Ga)As}(1 - \nu_{yx}\epsilon_{yy}^{(In,Ga)As} - \nu_{zx}\epsilon_{zz}^{(In,Ga)As})$$
$$(2.7)$$

using

$$\epsilon_{yy}^{(In,Ga)As} = \frac{a^{(In,Ga)As} - a_{(bulk)}^{GaAs}}{a_{(bulk)}^{GaAs}} \qquad (2.8)$$

and the directional Poisson ratios,

$$\nu_{yx} = \frac{2(C_{11}+5C_{12}-2C_{44})}{3(C_{11}+C_{12}+2C_{44})}$$

and

$$\nu_{zx} = \frac{4(C_{11}+2C_{12}-2C_{44})}{3(C_{11}+C_{12}+2C_{44})}$$

and

$$d_{2\bar{2}0}^{(In,Ga)As} = (d_{2\bar{2}0}^{GaAs} + \frac{0.404[\text{Å}]}{\sqrt{8}}x) \qquad (2.9)$$

The tensile strain of the GaAs core along [111] will result in compressive strain along [$11\bar{2}$] and [110]. Assuming ϵ_{yy}^{GaAs} is given by the projection of the normal strain components of the $1\bar{1}0$ side planes tilted by 30° with respect

to the y-axis, $\epsilon_{yy}^{\mathrm{GaAs}} \approx \frac{\sqrt{3}}{2}\epsilon_{xx}^{\mathrm{GaAs}}$, which roughly follows the cylinder approximation $\epsilon_{yy}^{\mathrm{GaAs}}$s $\approx \epsilon_{xx}^{\mathrm{GaAs}}$ [45], one may approximate

$$\mathrm{d}_{2\bar{2}0}^{\mathrm{GaAs}}(\exp) = \mathrm{d}_{2\bar{2}0}^{\mathrm{GaAs}}(1 + \epsilon_{xx}^{\mathrm{GaAs}}) \approx \mathrm{d}_{2\bar{2}0}^{\mathrm{GaAs}}(1 - (\frac{\nu_{zx}}{1 + \frac{\nu_{yx}}{2}\sqrt{3}})\epsilon_{zz}^{\mathrm{GaAs}}) \qquad (2.10)$$

Here, $\mathrm{d}_{(2\bar{2}0)}^{\mathrm{GaAs}}$ and $\mathrm{d}_{(2\bar{2}0)}^{\mathrm{(In,Ga)As}}$ are the lattice parameters of the unstrained materials, C_{ij} are the elastic constants [44,46], and the Poisson ratios are $v_{yx} = 0.61$; $v_{zx} = 0.49$. They are equally used for (In,Ga)As and GaAs. Similar calculations can be conducted to calculate the $22\bar{4}$ lattice parameters of GaAs and (In,Ga)As.

Chapter 3

Scanning modes used

This section discusses four experiments that have been used in the following chapters. The first is recording a 3D RSM of a Bragg reflection. This experiment has been used in all chapters. The second is nXRF imaging and it has been used in Chapter 3. The third and fourth experiments are quick SXDM and low energy CL in scanning electron microscopy and they have been used in Chapter 5. Explaining how these techniques work will make it easier to follow the experimental sections of this thesis.

3.1 Reciprocal space mapping

Here, recording a RSM of the 111 Bragg reflection, acquired from a single NW, will be explained. In this geometry, the incident and scattering angles in the substrate plane (β_1 and β_2) are set to zero whereas both incident and exit angles (α_i and α_f) of the X-ray beam with respect to the 111 lattice planes are close to the GaAs Bragg angle. The experimental geometry of the 111 XRD measurement is displayed in Figure 3.1a and for better visibility of β_1 and β_2, see Figure 5.1a. When the incident beam fulfills the Bragg condition with the 111 lattice planes, the detector plane in reciprocal space cuts the Bragg reflection at its center (see Figure 3.1 a,ii and b,ii). In order to fully scan the Bragg reflection, an angular θ scan around the Bragg angle in real

space is required (Figure 3.1a). The bigger the angular range is, the larger is the probed range by the detector plane in reciprocal space. For each step, the intensity distribution will be collected by recording a 2D frame using the 2D pixel detector. The total number of frames can then be composed to plot the 3D intensity distribution as a function of the reciprocal space coordinates Q_z^{hkl}, Q_y^{hkl} and Q_x^{hkl} defined by [47],

$$Q_x^{hkl} = K.(\cos\alpha_f.\sin\beta_2 + \cos\alpha_i.\sin\beta_1) \tag{3.1}$$

$$Q_y^{hkl} = -K.(\cos\alpha_f.\cos\beta_2 - \cos\alpha_i.\cos\beta_1) \tag{3.2}$$

$$Q_z^{hkl} = K.(\sin\alpha_f + \sin\alpha_i) \tag{3.3}$$
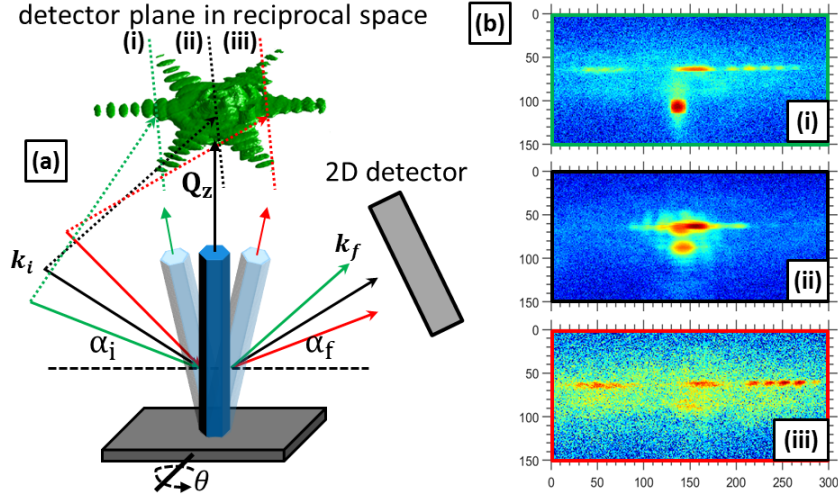
Figure 3.1: (a) A rocking θ scan around the 111 Bragg angle of GaAs. The green (i), black (ii) and red (iii) dotted lines represent the detector plane in reciprocal space at angles less, equal and larger than the Bragg angle. (b, i-iii) demonstrate the detector frames recorded at (i), (ii) and (iii) in (a).

The 3D RSM of the 111 Bragg reflection is demonstrated in Figure 3.2a. Here, Q_z^{111} is defined along the NW growth direction whereas Q_x^{111} and Q_y^{111}

are the reciprocal space vectors perpendicular to Q_z^{111}. The 2D projections in the (Q_z^{111}, Q_x^{111}) and (Q_z^{111}, Q_y^{111}) planes are displayed at the sides whereas the 2D projection in the (Q_y^{111}, Q_x^{111}) plane is displayed at the bottom. The six-sided star (Figure 3.2b,i) represents the Fourier transformation of the NW hexagonal cross-section i.e. each pair of opposite truncation rods (TR) in reciprocal space is perpendicular to a pair of opposite side facets in real space (compare Figures 3.2b,i and ii). Along each TR, thickness fringes are visible. From the separation ΔQ_{TR} between neighbored maxima or minima, the thickness, T, along a pair of opposite side facets can be evaluated using $T=2\pi/\Delta Q_{TR}$ [14]. From the angular orientation α, β and γ, of neighboring TRs in reciprocal space, one is able to calculate the angle between neighboring side facets in real space using 180 (α or β or γ). Furthermore, comparing ΔQ_{TR} measured along the three different TRs, one is able to calculate the thickness along all three opposing side facets, marked by orange, red and blue dotted lines in Figures 3.2b,i and 3.2b,ii. This makes it possible to reconstruct the entire cross-section of the investigated NW.
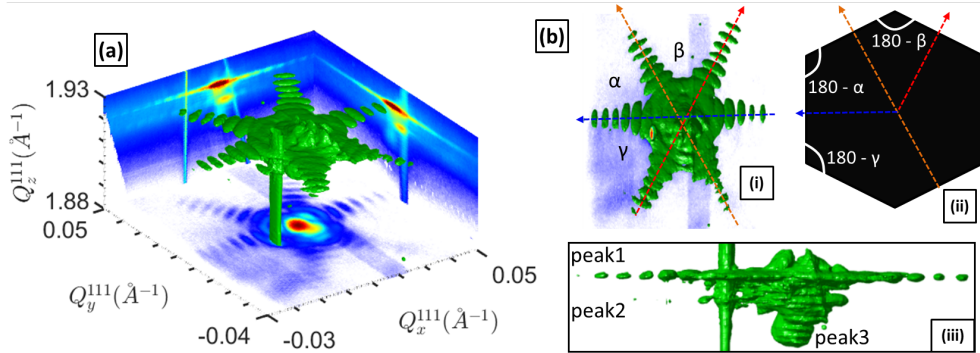
Figure 3.2: (a) bird view 3D RSM of the 111 Bragg reflection acquired from a single NW. 2D projections are displayed at the sides and bottom. (b,i) top view of (a). (b,ii) the total NW cross-section calculated from (b,i). The calculation process is explained in text. (b,iii) side view of (a).

Additional information about the axial d-spacing, using eq. 2.4, and the existing polytypes at the scanned NW volume, can be achieved from Q_z^{111}

(Figure 3.2b,iii).

3.2 X-ray fluorescence nano-scale characterization

Another use of X-rays is XRF, which is an established technique for qualitative and quantitative elemental analysis in a wide variety of application fields [48–50]. Compared to other analytical techniques, XRF has many advantages. It measures a wide range of elements and concentrations in many different types of materials. It is non-destructive and requires no or very little sample preparation. The evolution of synchrotron radiation sources and advances in X-ray optics has allowed the achievement of collimated X-ray beams with dimensions in the nanometer range and the feasibility of nXRF scanning microscopy [40]. This made it possible to measure individual NWs regardless if tilted, broken or grown perpendicular to the surface of the substrate.

When the high energy primary X-ray collides with an atom, it disturbs its equilibrium. If the energy of the radiation is higher than the binding energy of an inner atomic shell, a tightly bond inner electron gets excited into vacuum leaving a vacancy behind. An outer electron then replaces the missing inner electron releasing a fluorescent X-ray (Figure 3.3). The energy of the emitted fluorescence photon is given by the energy difference between the associated orbitals. For example, if an electron transitions from a level with energy E_i to one with energy E_j, the emitted X-ray has energy $E_X = E_i - E_j$. Because the energy of the emitted photon is characteristic of a transition between specific electron orbitals in a particular element, the resulting fluorescent X-rays can be used to detect the abundances of elements that are present in the sample.

This means that XRF provides qualitative information about the sample measured; however, XRF is also a quantitative technique. The X-rays emitted by the atoms in the sample are collected by the detector and processed in the analyzer to generate a spectrum showing the X-rays intensity versus their energy. An example is shown in Figure 4.5 i.e. the spectrum is collected from a single GaAs/(In,Ga)As/GaAs core-multi-shell NW. The peak energy identifies the element whereas the intensity gives an indication about its concentration in the investigated specimen. For example, the two
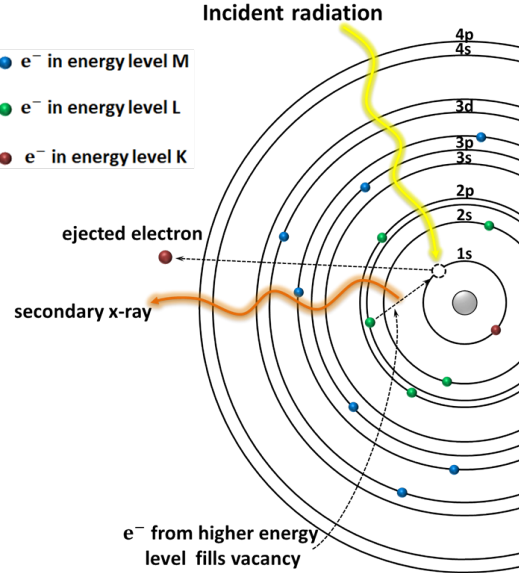
Figure 3.3: A sketch of an atom showing the various atomic levels, designated K, L and M. Each of these has additional sub-shells.

peaks marked by Ga in Figure 4.5 correspond to the $K_{\alpha 1}$ and $K_{\beta 1}$ excitation energies of Gallium at 9.251 keV (left) and 10.267 keV (right), respectively. The Ga $L_{\alpha 1}$ and $L_{\beta 1}$ excitation energies, found at 1.098 keV and 1.125 keV, could not be detected as they coincide with noise at low energies. Materials other than Ga, As and In originate from the experimental setup and materials inside the hutch as the measurement was not done in vacuum. Knowing the numerical transition energies of each element, one can select a certain peak from the spectrum and scan the surface of the substrate searching for NWs. An illustration is displayed in Figure 3.4 where the Ga $K_{\alpha 1}$ and $K_{\beta 1}$ excitation energies were selected to scan a quadratic area on the substrate. This makes it possible to locate and scan specific individual NWs. Bright spots represent individual NWs that are either grown tilted or perpendicular to the surface. A tilted NW, marked by a red box in Figure 3.4b, has been

measured by nXRF. A zoom in of the NW is shown in Figure 3.4c whereas the Ga and In XRF signals are demonstrated in Figures 3.4d and 3.4e.
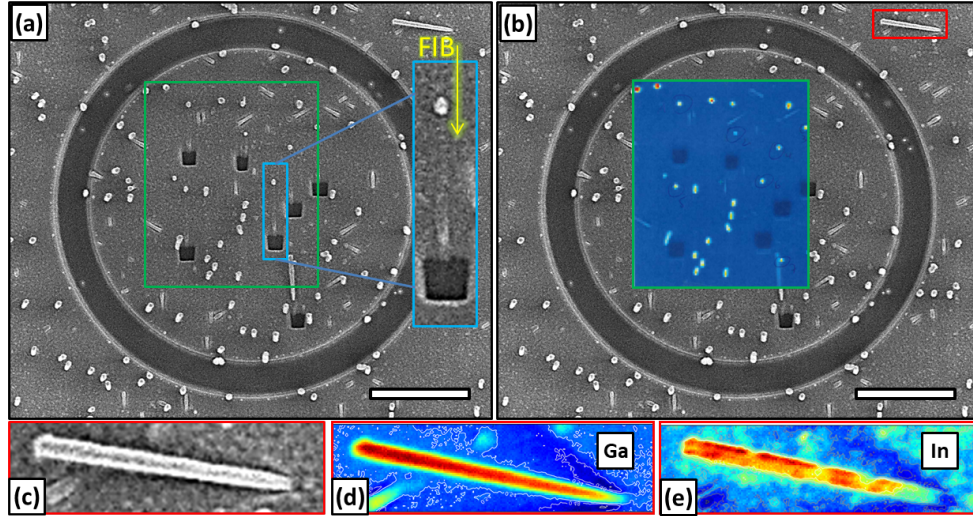
Figure 3.4: (a) Top view SEM micrograph of a FIB patterned circle on a Si 111 substrate with NWs grown on top. Few NWs were processed with FIB leaving quadratic holes on the surface of the substrate behind. The holes indicate the positions where the ion beam hits the substrate. A zoom of a FIB cut NW is marked with blue i.e. the trace of the ion beam resulting from shadowing by the NW is still visible. The yellow arrow indicates the direction of the ion beam. (b) The same SEM image as in (a) only that the k_α- Ga fluorescence signal of the area indicated by a green box is scanned with X-rays. (c) Zoom in of a tilted grown NW, marked by a red box in (b). (d,e) Ga and In fluorescent signals of the NW shown in (c).

3.3   Quick scanning X-ray diffraction microscopy

SXDM is a two dimensional quick and continuous mapping technique which provides nanometer resolution of a specimen at a given position in reciprocal space. The resulting real space maps are made by translating the sample across the beam and simultaneously recording scattering images at every point along a rocking curve. This technique has been improved in the nano beam station ID01 of ESRF [51] and will be used to inspect the polytype distribution along the growth axes of single NWs and the results will be

demonstrated in Chapter 5. As the angular separation between the Bragg angles of ZB, WZ and any mixed phase of the two polytypes is small, one can apply this technique at the Bragg angle of ZB instead of performing a complete angular scan. This would only influence the intensity of each polytype but not their spatial distribution. The advantage of this technique lies in its non-invasive nature and sensitivity to the lattice parameter and crystal phase structures along the probed volume [52] as it has also allowed for the study of individual nanostructures [25]. An animation of a 2D mesh scan across a single NW is illustrated in Figure 3.5a. The NW is assumed to be composed of different polytypes along its growth axis, e.g. ZB (blue), WZ (green) and a mixture of both (red). Figure 3.5b shows detector frames in reciprocal space at the three scanned positions indicated in 3.5a. Regions of interest can then be defined around the ZB and WZ Bragg reflections and in between for any mixed phase of the two polytypes. The resulting 2D spatial distribution of each polytype along the NW growth axis in real space are demonstrated in Figure 3.5c.
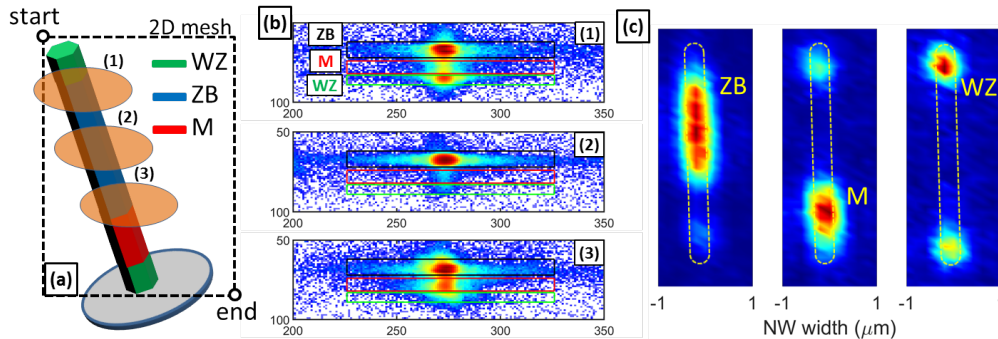
Figure 3.5: (a) Animation of a 2D mesh scan across full length of a single NW. The starting and ending points of the 2D scan are indicated by white filled circles. The beam is represented by an orange oval. The NW can be scanned from top to bottom or vice versa. (b) Reciprocal space detector frames taken at different positions along the NW growth axis. The ZB and WZ contribution in (1), only ZB in (2) and ZB and a mixed face in (3) reflect the polytype presence at the illuminated NW section. (c) The 2D spatial polytype distribution of ZB, M and WZ along the NW growth axis in real space.

3.4 Cathodoluminescence imaging

When a crystal is illuminated by an electron beam of sufficient energy, electrons from the lower-energy valence band are promoted to higher-energy levels in the conduction band. When attempting to resettle at the valence band ground state, the energetic electrons may get trapped either by intrinsic structural defects and/or extrinsic impurities. Traps can interact in different scenarios to produce luminescence (Figure 3.6). The first scenario, the electrons excited to the conduction band may not encounter a trap and fall to the valence band (1). The second scenario, they move randomly through the crystal structure until a trap is encountered. From that trap, the electron might return to the ground state (2) or it may encounter multiple traps (3) emitting photons with wavelengths dependent on the energy differences. When vacating the traps, the electrons will emit energy. If the energy is in the appropriate wavelength range, luminescence will be produced. Most of the photons fall in the visible portion of the electromagnetic spectrum whereas some fall in the ultraviolet and infrared portions.
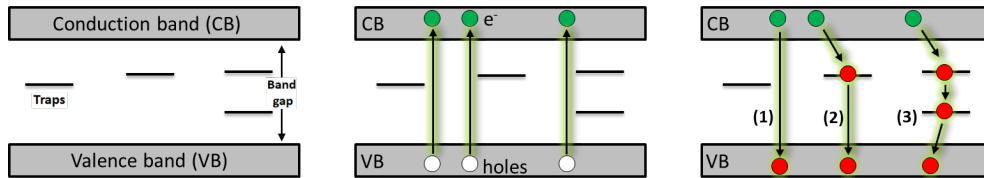
Figure 3.6: (Left) Semiconductor valence and conduction bands with hypothetical electron traps, indicated by horizontal lines. (Middle) electrons excited from valence band to conduction band leaving holes behind. (Right) Possible paths of electrons as they fall back to ground state of the valence band. Scenarios (1), (2) and (3) are explained in text.

Optical measurements e.g. CL [53] and photoluminescence (PL) [54] done on pure GaAs NWs predict a higher band gap of unstrained WZ GaAs compared to that of ZB [55]. As shown schematically in Figure 3.7, WZ/ZB GaAs heterostructures exhibit a type II band alignment [30] where electrons and holes are spatially separated and stored in the ZB and WZ regions, re-

spectively. When the segment thickness of the two poytypes is in the range of several nanometer, quantum wells (QW) with quantized levels of electrons and holes are formed i.e. the thinner the QW, the higher is the quantization energy. The electron-hole pair confined to the WZ/ZB interface results to a spatially indirect recombination at 1.43 eV which should be the lowest energy observable in pure GaAs WZ/ZB multilayer structures.

CL imaging is an analytical technique that combines functional optical information with the spatial resolution of electron microscopy. In the scanning electron microscope (SEM) or the scanning transmission electron microscope (STEM), low-energy CL microscopy is considered as a very useful tool for the characterization of low dimensional nanostructures such as quantum dots and semiconductor NWs [56–58]. The respective technique has the advantage of revealing not only the pres-

Figure 3.7: (a) Schematics of the band alignment between consecutive ZB and WZ GaAs segments of different width. The conduction and valence band discontinuities are denoted by E_c and E_v. The band gap of each polytype is denoted by E_g. Horizontal red lines represent quantized levels for electrons and holes in conduction and valence bands.

ence of luminescence centers but also their spatial distribution along the specimen. The optical characterization of NWs is usually performed by statistically averaging their ensemble. However, for core-shell NW systems, this approach is imprecise and sometimes misleading due to the possible coexistence of different factors that may influence the NW optical properties, i.e. a variation in the core/shell thicknesses and/or alloy concentration. Low-energy CL allows the characterization of individual NWs i.e. the combination with other electron beam techniques makes it possible to determine the origin of the luminescence [94].

Chapter 4

Spatial indium distribution within the (In,Ga)As shell

In this chapter, we present two complementary approaches to investigate the In content and homogeneity within in the (In,Ga)As shell of GaAs/(In,Ga)As/(GaAs) core-shell-(shell) NWs using synchrotron radiation. The NWs have been characterized in their as-grown configuration.

- First, we determine the mean In content of the (In,Ga)As shell by high resolution XRD done on NW bunches.

- Second, we study the In distribution within individual NWs by nXRF.

From XRD, we were able to disentangle the influence of In content and shell thickness by measuring and analyzing two Bragg reflections with diffraction vector parallel and perpendicular to the growth axis, respectively. From nXRF, both the NW 111 basal plane, that is parallel to the surface of the substrate, and the $10\bar{1}$ sidewall were scanned with a 50 nm × 50 nm nanobeam. NWs with different nominal In content of the (In,Ga)As shell were inspected such that the average In concentration determined by XRD shows good agreement with the nominal value.

- For a nominal In content of 15%, the In distribution is fairly uniform between all six sidewall facets.

- For NWs with 25% nominal In content, different sidewall facets of the same NW exhibit different In contents. This effect is attributed to shadowing during growth by molecular beam epitaxy. However, the In distribution along the NW growth axis is still fairly homogeneous.

- In NWs with 60% nominal In content and no outer GaAs shell, the In content

varies significantly between different sidewall facets and along the NW growth axis. This fluctuation is explained by the formation of (In,Ga)As mounds that grow simultaneously on top of a thinner (In,Ga)As shell.

The methodology presented here may be applied also to other core-shell NWs with ternary shell and paves the way to correlating NW structure with functional properties that depend on the as-grown configuration of the NWs.

4.1 Introduction

Naturally, the optical properties of such core-shell NW heterostructures depend on their structure, i.e. the chemical composition, the thicknesses of core and shell(s), strain, and the crystal phase. Thus, the precise characterization of these properties is indispensable for progress with respect to applications. We emphasize that variations between different NWs in an ensemble are common, and in particular the composition of ternary alloys may be inhomogeneous even within individual NWs. The most widely used methods for structural analysis at the nanoscale are based on TEM. In particular, compositional information can be deduced, e.g., from EDX and HAADF images [17, 18, 59–61]. Alternatively, X-rays may be used as a probe for structural characterization [62, 63]. High resolution XRD reveals periodicity of both the crystal lattice and heterostructures in specific directions, which can be analyzed to deduce composition and thicknesses. Furthermore, XRF provides direct chemical information of the specimen. With recent achievements in preparing X-ray beams with nanometer diameter at synchrotron radiation sources [64], it is flexible nowadays to study either NW ensembles or individual NWs [65–68]. The key benefit of X-ray based approaches is that NWs can be accessed in their as-grown configuration on the substrate, while TEM characterization requires preparing and then removing a very thin NW lamella from the substrate. This benefit principally allows the correlation between structure and functional NW properties for one and the same NW without being affected by sample preparation, like PL, light coupling effects [69], or charge injection from the substrate [70].

In this paper, we report two complementary X-ray based methods for the structural analysis of core-shell NWs involving ternary compounds, exemplified by GaAs/(In,Ga)As/(GaAs) core-shell-(shell) NW heterostructures. On the one hand, we employ high-resolution XRD in two orthogonal directions from NW ensembles in combination with scattering simulations based on a finite element method (FEM) approach to determine the average In content of the (In,Ga)As shell in the NW ensemble. In particular, the analysis of the

strain along and perpendicular to the NW axis enables us to disentangle composition and thickness of the ternary shell. On the other hand, we use nXRF measurements on individual NWs to study the compositional homogeneity of the ternary shell.

4.2 Experimental and computational details

The three investigated samples were grown by Ga-assisted molecular beam epitaxy (MBE) on Si 111 substrates. Details of the growth are described elsewhere [15, 71]. For sample 1, a pre-patterned substrate was used, resulting in an ordered array of NWs [32], while the other two NW ensembles are random. The NWs are typically 4 µm long and composed of a 140 nm diameter GaAs core covered subsequently by (In,Ga)As and GaAs shells. The (In,Ga)As shells were deposited at a substrate temperature of about 405 °C with high As$_2$:Ga flux ratio [atomic ratio above 40]. The three different samples differ mostly in the nominal In content of the shells, which was varied by changing the In/(In+Ga) flux ratio. A previous study of similar samples indicated that the crystal structure of these NWs is predominantly ZB with a small WZ content [71]. The shell thickness, t, and In shell content, x, of each sample under investigation are listed in Table 4.1 along with the NW number density and other information that will be introduced later.

Table 4.1: Structural information about the investigated samples. The NW density was extracted from SEM images, and the core-shell configuration, nominal dimensions and nominal In content of the (In,Ga)As shell mentioned in the first four rows, were deduced from MBE growth parameters. The In concentration x, thickness t, and the out-of-plane as well as in-plane elastic strain values of the (In,Ga)As shell listed in the last four rows, were determined from XRD measurements along the [111] and [2$\bar{2}$0] direction as described in the text. However, for sample 3 the In content had to be deduced from the parasitic growth on the substrate between the NWs.

	Sample 1	Sample 2	Sample 3
NW density (µm^2)	0.1	1	1
core-shell configuration	GaAs/(In,Ga)As/GaAs	GaAs/(In,Ga)As/GaAs	GaAs/(In,Ga)As
nominal dimensions (nm)	140/40/30	140/40/30	140/18
Nominal [In] (%)	15	25	60
XRD [In] (%)	15 $\pm$ 0.7	27 $\pm$ 1.5	70 $\pm$ 8
XRD [t] (nm)	40 $\pm$ 2	36 $\pm$ 3	not accessible
$\epsilon_{zz}^{(In,Ga)As}$ (%)	-0.56	-1.11	not accessible
$\epsilon_{xx}^{(In,Ga)As}$ (%)	0.93	1.59	not accessible

Figures 4.1a and 4.1b show exemplary SEM micrographs of individual NWs from sample

2 and sample 3, respectively. The NWs of samples 1 and 2 exhibit smooth shells whereas the morphology of NWs with high nominal In content on sample 3 is characterized by the presence of mounds resulting in a rough shell surface (Figure 4.1c), as observed before [71] An overview SEM images of all three samples are shown in Appendix A. In addition, both images display a droplet-like feature at the NW top. This feature results from the consumption of the Ga droplet at the NW top prior to the growth of the radial heterostructure and concurrent axial growth. Prior to the XRF measurements of selected individual NWs, approximately 2 µm of the NW top were removed [sketch and SEM in Figures 4.1d and 4.1e, respectively] using FIB, in order to simplify the characterization of the elemental distribution in the NW plane-view cross-section. The droplet-like feature at the NW top exhibits a roundish shape from an in plane view (Figure 4.1f) whereas the FIB procedure exposed the hexagonal cross-section of the NW basal plane with the six well pronounced 110 sidewall facets (Fig. 4.1g).
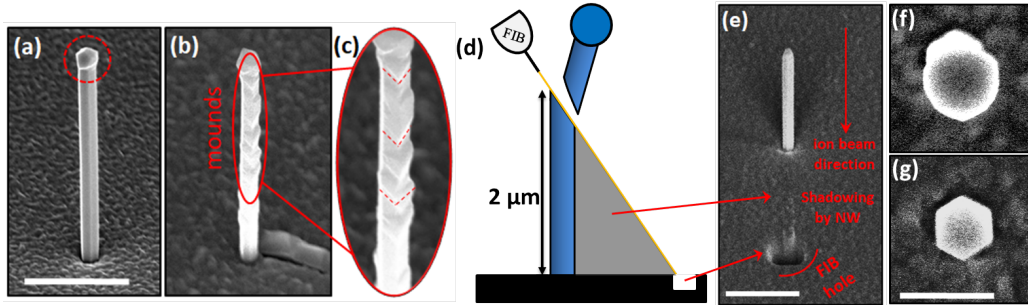
Figure 4.1: SEM images and FIB cutting. (a) and (b) SEM micrographs of single NWs from samples 2 and 3, respectively. The NW from sample 2 shows smooth outer shell whereas accumulation of mounds is visible at the circumference of the NW from sample3. (c) Zoom in along the NW growth axis, marked by a red circle in (b). The growth of the mounds takes place along the direction indicated by linear dotted lines and in the opposite direction along the growth axis of the opposite facet not visible in this SEM image. (d) and (e) Animation and SEM micrograph of NW upper section cutting process using FIB. The NWs are cut to approx. 2 µm in length at a 30° incident angle. Both, hole and the straight line in (e) explained schematically in (d), are a consequence of the ion beam and the shadowing caused by the NW length. (f) and (g) are top views of the NW cross-section before and after cutting the droplet-like feature at the NW top.

In order to trace individual NWs grown at random positions on substrates with native oxide layers [samples 2 and 3] during the nXRF experiment, several NWs were isolated inside FIB etched circles. A demonstration can be seen in Figure 4.2a. A circle with circumference of 5 µm in thickness and inner radius of 25 µm was etched from the surface

of the substrate using Ga focused ion beam. To avoid Ga deposition on the NWs during the etching process, low ion beam current was used and a separation of atleast 10 µm was maintained from the circumference of the inner circle. Figure 4.2b shows a SEM image at 52° view angle of the same NW region after cutting the NWs top sections by FIB. For NWs grown on pre-patterned substrates, isolating NWs by FIB etched markers was not required as the position of each individual NW could be identified. Each NW field, from which specific single NWs were selected, can be distinguished by large numbers at each side. For example, the NW field displayed in Figure 4.2c has a separation of 10 µm between neighboring NWs and hole diameter of 90 nm. The first four NWs at the top right corner of the corresponding NW field were selected and cut by FIB (see Figure 4.2d).
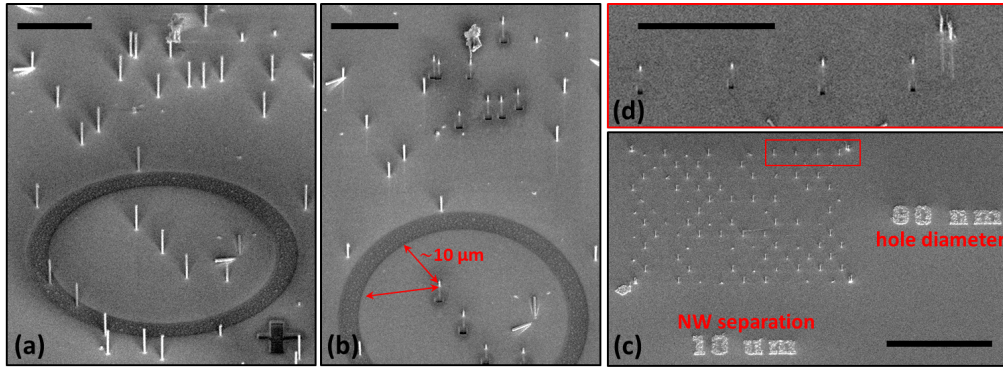
Figure 4.2: FIB marking for easier NW tracing during nXRF. (a) NW region marked by a FIB patterned circle 20 µm in radius. The NWs here were still not cut by FIB. (b) The same NW area after cutting the droplet like feature at the NW top with FIB. (c) Sample2, NW field with 10 µm separation between neighboring NWs and 90 nm hole diameter. (e) Zoom in into the NW area marked by a red box in (e) after cutting the NWs top sections by FIB. Scales in (a,b), (c) and (d) are 10, 50 and 15 µm, respectively.

For the nXRF study, we used the nanoprobe station ID16B of the ESRF in Grenoble. The nanoprobe is a pink beam with upper energy cutoff at 29.46 keV. Due to its high photon energy, the nanobeam is transmitted through the whole nanostructure without major absorption loss, exciting element-specific fluorescence radiation. Further details regarding the beamline instrumentation can be seen in Figure 4.3 and found elsewhere [40].
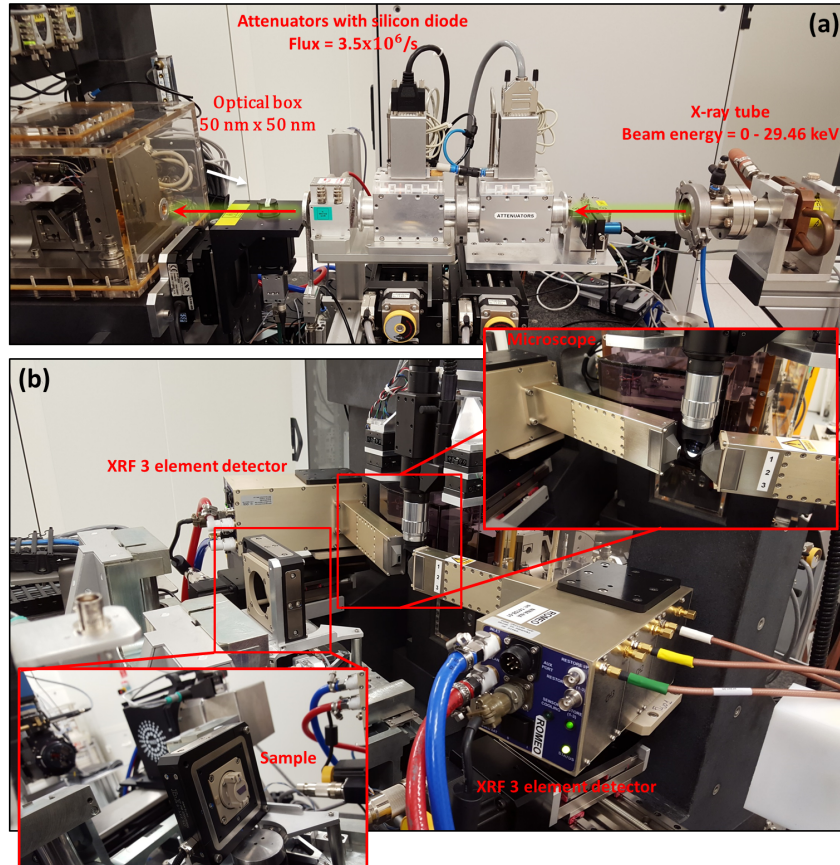
Figure 4.3: ID16b nXRF experimental setup. (a) labeled from right to left, X-ray tube with generated x-ray beam energy ranging from 0 to 29.46 keV. Set of attenuators tuning the photon flux to 3.5 x 10^6 /s. Optical box consisting of couple of Kirkpatrick-Baez positioned perpendicular to one another as demonstrated in the animation in Figure 4.4a. This results in a nano focused beam 50 nm x 50 nm [hor x ver] in size. The beam path is indicated with yellow glowing red arrows. (b) is a continuation of (a). A microscope was implemented in order to trace the marked FIB cut NWs. Two XRF 3 element dispersive detectors were placed at each side from the sample at an angle of 15° with respect to the sample plane. The circular gap on the left side, indicated with a red box, is where the sample was then mounted.

Figure 4.4a shows a schematic view of the experimental setup. Illuminated by the probing beam, the sample is scanned with a step size of 10 nm along the NW basal plane of free-standing NWs or along the side plane of NWs laying on the substrate [see sketch in Figure 4.4b] with an acquisition time of 0.5 s per step, which was sufficient to achieve highly intense XRF maps. The elemental composition and local properties of the NWs

were estimated by fitting the XRF spectra using the software PyMca [72].
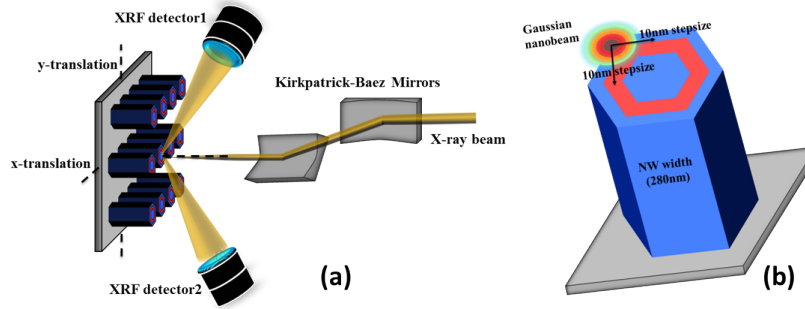
Figure 4.4: (a) A schematic illustration of the setup at the XRF station ID16b of the European Synchrotron Radiation Facility. (b) Sketch of how the X-ray nanobeam is scanned across the NW area during the XRF experiment.

As the experiment is set under ambient conditions, the incident radiation interacts not only with the material inside the sample but also with air molecules and the material of the experimental hutch. The measured fluorescence energy spectrum of sample 1 after excitation by the incident X-ray beam is shown in Figure 4.5.
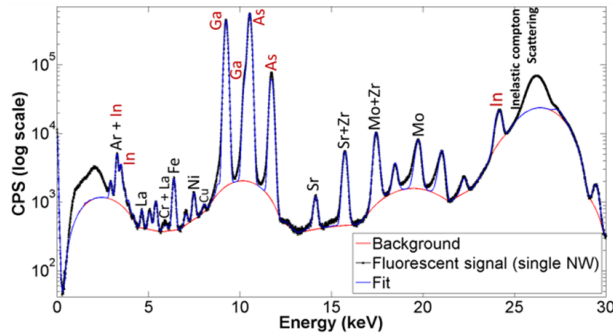
Figure 4.5: Fluorescence energy spectrum acquired during the measurement of sample 1. The lines are labeled with the elements that they correspond to. The spectrum contains lines originating from the sample [elements In, Ga, As marked in red] but also other lines originating from air and the experimental setup.

The spectrum contains a large number of lines, out of which the ones associated with the elements In, Ga, and As present in the sample are labeled in red. The other lines seen in the spectrum originate from material other than the investigated sample, e.g. the collimator, and are thus irrelevant.

32

4.3 XRD and FEM results and discussion

XRD measurements on NW ensembles were carried out at beamlines BL9 of the DELTA synchrotron [TU Dortmund] and P08 of PETRA III [DESY, Hamburg] using 1 x 1 mm^2 beam with photon energy of 13 keV, and a 2D pixel detector. In particular, we recorded 2D RSMs of the axial 111 and radial $2\bar{2}0$ Bragg reflections. Due to the lattice mismatch between the GaAs core and the (In,Ga)As shell, the NW heterostructures are affected by epitaxial strain. Depending on the amount of lattice mismatch, this strain can relax plastically or accommodate elastically accompanied by lattice deformation. In a previous publication on such GaAs/(In,Ga)As core-shell NWs, Lewis et al. [71] did not observe any plastic strain relaxation up to an In content of 40%. Thus, in the present study we can safely analyze the results for samples 1 and 2 assuming elastic relaxation. Furthermore, in the study by Lewis et al. [71], XRD profiles were acquired across the 111 reflection that reveals strain along the NW growth axis. In this direction, because of pseudomorphic growth, the GaAs core and (In,Ga)As shell share the same lattice constant, whose value depends both on the In content in the shell and the dimensions of core and shell in the radial direction. Hence, for the deconvolution of shell thickness and In content, additional information is needed. Therefore, we measured for the present study RSMs both around the out-of-plane 111 and the in-plane $2\bar{2}0$ reflections [where the word plane refers to the substrate plane]. As we will explain in more detail below, the combination of these two independent measurements allows the determination of the mean In content within the (In,Ga)As shell.

While the lattice constant along the growth direction (axial direction) is the same for core and shell materials, the lattice constant in direction perpendicular to the growth axis (radial direction) varies within the core-shell heterostructure. This variation is sketched in Figure 4.6a, which follows the model introduced by Stankevič et al. [73]. Analogous to planar films, it is supposed that the strain state within each of the six NW side facets is laterally homogeneous. As there may be deviations from this simplification at the edges of the hexagon, they are not included in the schematic. The red lines indicate $1\bar{1}0$ planes of the (In,Ga)As shell. The lattice spacing between these planes is different in sidewall facets that are oriented perpendicular to the $[1\bar{1}0]$ direction (label C) or inclined (label B). Both spacings differ, in turn, from the lattice spacing in this direction in the GaAs core. Furthermore, yet another value is expected for the outer GaAs shell (label A).

The variation in the in-plane lattice constant becomes visible in the RSM taken at the $2\bar{2}0$ Bragg reflection of sample 2 displayed in Figure 4.6b. The two axes of this figure

correspond to, on the one hand, the reciprocal vector $Q_\parallel^{2\bar{2}0}$ indicating the momentum transfer in the direction $[2\bar{2}0]$ measured in the XRD experiment and, on the other hand, the perpendicular reciprocal vector $Q_\perp^{2\bar{2}0}$ [Later on, similar notations are used for the 111 measurements]. The RSM contains as expected several peaks. The most intense one corresponds to the GaAs core. Compared to this peak, the strongest deviation along $Q_\parallel^{2\bar{2}0}$ occurs in region C of the (In,Ga)As shell. In regions B, the lattice planes of the (In,Ga)As shell are tilted by $\pm\, 60^o$ with respect to the direction of measurement, and the $1\bar{1}0$ lattice spacing lies in between the two extremes of core and region C. In other words, because the unit cells are orthorhombically deformed, the respective lattice parameters of these tilted planes are projections of the component of the (In,Ga)As shell.
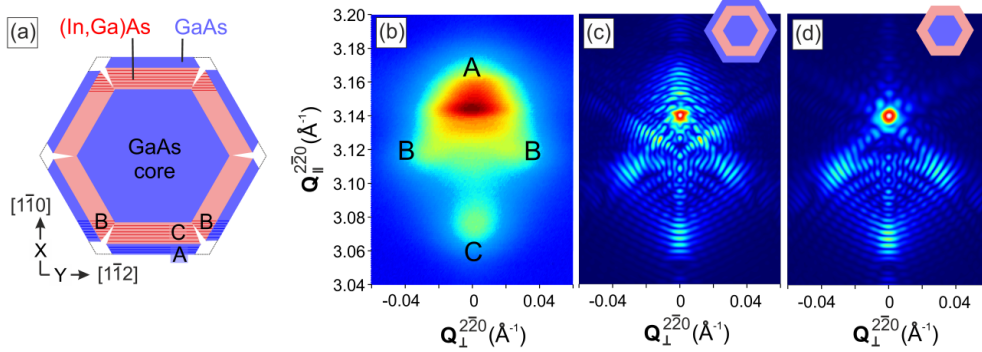
Figure 4.6: Panel (a) illustrates the strain distribution along $[2\bar{2}0]$ for a single GaAs/(In,Ga)As/GaAs core-shell-shell NW heterostructure. Lines colored in red and blue and labeled C and A represent the $2\bar{2}0$ crystallographic planes of those (In,Ga)As and GaAs shell facets, respectively, that are oriented perpendicular to the direction scanned during out-of-plane XRD. Peak B corresponds to the $2\bar{2}0$ planes of the (In,Ga)As shell in neighboring facets. Note that these planes exhibit a different angle with respect to the facet orientation than the C planes, and thus different lattice spacing. The assignment is confirmed by finite element simulations presented in (c) and (d). As the strain state along the NW edges is expected to be different compared to the NW side facets, the areas close to the NW edges are kept empty in the schematic. (b) 2D RSM of the $2\bar{2}0$ reflection for sample 2. (c) & (d) show scattering simulations of the $2\bar{2}0$ reflection for a single 140/40/30 nm GaAs/(In,Ga)As/GaAs core-shell-shell and 140/40 nm GaAs/(In,Ga)As core-shell NWs with nominal In content of 25%, respectively.

Depending on the inclined orientation of the sidewall facet, for region B, momentum is additionally transferred either in the positive or negative direction $Q_\perp^{2\bar{2}0}$, and correspondingly there are two symmetric peaks B in the RSM. For the outer GaAs shell, the change in $2\bar{2}0$ lattice spacing is compared to the GaAs core in the opposite direction as for the (In,Ga)As shell, and thus for region A, a shoulder is visible on top of the core peak.

For scattering simulations, the strain distribution in a GaAs/(In,Ga)As core-shell NW was computed using the numerical FEM approach. The FEM, which is based on linear elasticity theory, takes into account the hexagonal cross-sectional shape of the NW as well as the full anisotropy of the elastic constants. For the ternary alloy (In,Ga)As, the elastic constants were obtained via linear interpolation of those of GaAs and InAs. We employed the commercial software package MSC Marc[c]. The step width of the grid varied between 1 and 2 nm and was chosen with higher node density at regions with strong strain gradients. In order to substantiate the correlation between the different regions of the core-shell heterostructure and the different peaks in the RSM explained above, we simulated the diffraction pattern of the $2\bar{2}0$ reflection for a single NW model using kinematic scattering theory. The kinematic sum,

$$I(q) \propto |\sum_j f^0_{atom,j} e^{iQ.[r_j+u(r_j)]}|^2 \tag{4.1}$$

adds up the plane waves that are coherently scattered from each individual atom. Here, the atomic positions r_j can be displaced from their ideal positions by a vector $u(r_j)$, e.g., due to strain, and $f^0_{(atom,j)}$ is the atomic scattering factor. The displacement of the atomic positions is obtained via interpolation of the ideal atomic positions with the three-dimensional displacement field of the core-shell (In,Ga)As/GaAs NW, simulated using a FEM approach. The result is presented in Figure 4.6c and is in qualitative agreement with the experimental RSM in Figure 4.6b thus confirming the assignment made above. Moreover, it is possible to retrieve the influence of the outer GaAs shell on the diffraction pattern by eliminating the respective nodes from the FEM model while maintaining the actual 3D displacement field of the full model. The result can be observed in Figure 4.6d. In this simulation, the peak A associated with the outer GaAs shell is not present.

To quantify the experimental XRD data, we created line profiles along $Q^{111}_{\parallel}$ and $Q^{2\bar{2}0}_{\parallel}$ from the RSMs of both the 111 and $2\bar{2}0$ reflections of all three samples, respectively, as shown in Figure 4.7a and 4.7b. This was done by integrating the intensity along $Q^{111}_{\perp}$ and $Q^{2\bar{2}0}_{\perp}$, respectively. Considering the 111 reflections in Figure 4.7a, the peak of the Si substrate, appearing at $Q^{111}_{\parallel} = 2.004$ Å^{-1}, has the highest intensity and is used as a reference. Furthermore, there are three peaks related to the grown III-V materials. We associate the peak of the overall second highest intensity, labeled by "PS", with the pseudomorphic lattice parameter of the core-shell NWs along the NW axis. In addition, the vertical lines labeled D and E indicate the $Q^{111}_{\parallel}$ positions corresponding to relaxed cubic GaAs and (In,Ga)As with In contents close to the nominal values. Following the discussion in Ref. [71], these

peaks are assumed to arise from parasitic growth on the substrate between the NWs. In particular, the vertical lines labeled E mark mean In contents of 15%, 27% and 70% for samples 1, 2, and 3, respectively. These values are in good agreement with the nominal values and are for samples 1 and 2 the result of an elaborate procedure to determine the In content in the (In,Ga)As shell from the XRD data that is described in the following.

The peaks in the line profiles were de-convoluted using a multi-Gaussian fit, and then the peak positions measured in Q space were transformed into lattice parameters d_{hkl} using eq. 2.5 and the lattice parameter was calculated by eq. 2.6. Assuming the thicknesses of core and shells shown in Table 4.1, the volume fraction of the (In,Ga)As shell is V = 0.367 for all three samples. For the example of sample 2 with nominal In content x = 0.25, one estimates $\epsilon_{zz}^{(In,Ga)As} \approx -0.011$ and $\epsilon_{zz}^{GaAs} \approx +0.0065$. However, as d_{111} depends on the dimensions of the core and shells in addition to the In content, one cannot determine the In content in the (In,Ga)As shell from measuring the 111 reflection alone without knowing the core and shell thicknesses.

In Figure 4.7b with the $2\bar{2}0$ measurements, a Si reference point is missing because the $2\bar{2}0$ peak of the Si substrate is not excited as the probing X-ray beam was nearly parallel to the surface of the substrate. Instead, the peak of highest intensity corresponds to unstrained GaAs. Thus, we associate this peak with the lattice parameter of the GaAs core. Due to tensile strain along [111], the core is expected to be compressed along $[2\bar{2}0]$ by $(1 + \epsilon_{xx}^{GaAs})$. All other peak positions are measured with respect to this peak. In all samples, we find three additional peaks named A, B and C. In extension of the model introduced by Stankevic *et al.* for (In,Ga)N/GaN core-shell single NWs [73], we assign the center of the broad peak C to the $2\bar{2}0$ lattice parameter of the (In,Ga)As shell in sidewall facets parallel to $2\bar{2}0$, as explained above (Figure 4.7). This lattice parameter will show an expansion $(1 + \epsilon_{xx}^{(In,Ga)As})$ due to the biaxial compressive strain along the [111] and $[11\bar{2}]$ directions, ϵ_{zz} and ϵ_{yy}, respectively.

In eqs. 2.8 and 2.10, $d_{2\bar{2}0}^{GaAs}$ and $d_{2\bar{2}0}^{(In,Ga)As}$ are the lattice parameters of the unstrained materials, C_{ij} are the elastic constants [44, 46], and the Poisson ratios are $v_{yx} = 0.61$; $v_{zx} = 0.49$. They are equally used for (In,Ga)As and GaAs.
Exemplary the strain evaluation will be demonstrated for sample 2. Following eq. 2.11, and considering ϵ_{zz}^{GaAs} taken from d_{111}^{exp} using eq. 2.7, the value $d_{2\bar{2}0}^{GaAs}(exp)$ of the GaAs core is deformed by $1 + \epsilon_{xx}^{GaAs} = 1 - 0.654 v_{zx} \epsilon_{zz}^{GaAs} \approx 0.9980$ with respect to the unstrained value. In other words, the peak corresponding to the radially compressed GaAs core is found to be shifted by $\Delta q_{||} \approx +0.004 \text{Å}^{-1}$ towards larger values compared to $d_{2\bar{2}0}^{GaAs}$. Fol-

lowing eq. 2.8 and 2.11 and using $\epsilon_{xx}^{(In,Ga)As}$ from eq. 2.8, the value $d_{2\bar{2}0}^{(In,Ga)As}(exp)$ for (In,Ga)As is deformed by $1 - \nu_{yx}\epsilon_{yy}^{(In,Ga)As} - \nu_{zx}\epsilon_{zz}^{(In,Ga)As} \approx 1.0164$ resulting in a peak shift of $\Delta q_{||} \approx -0.031 \text{Å}^{-1}$ compared to the unstrained value. Because eq. 2.6 contains the product xV, but eq. 2.8 depends on x only, both x (In content) and V (i.e. shell thickness t) can be disentangled by measuring $d_{111}(exp)$ and $d_{2\bar{2}0}^{(In,Ga)As}(exp)$. Following this procedure, the mean In contents are estimated to be x $= 0.150 \pm 0.007$ and 0.270 ± 0.015 with shell thicknesses of 40 ± 2 nm and 36 ± 3 nm for samples 1 and 2, respectively, as shown in Table 4.1. Using these strain values, the unit cell of the (In,Ga)As shell is uniaxially deformed by $1 - \frac{(1+\epsilon_{xx}^{(In,Ga)As})}{(1+\epsilon_{zz}^{(In,Ga)As})} \approx 1\%$ and 2%, for sample 1 and 2, respectively, towards the radial direction.

For sample 3 with a nominal In content of 60%, according to the results of Lewis *et al.* [71] an additional path for strain relaxation beyond the elastic deformation regime is relevant. For such structures Lewis *et al.* demonstrated a new scenario for strain relaxation, where a coherently strained (In,Ga)As NW shell and plastically relaxed (In,Ga)As mounds grow simultaneously on the GaAs NW sidewalls. Detailed calculations of such a complex relaxation mechanism are underway but beyond the scope of the present study. Therefore, we suppose peak E originates from parasitic islands which corresponds to unstrained (In,Ga)As with mean In content of x $= 0.70 \pm 0.08$.
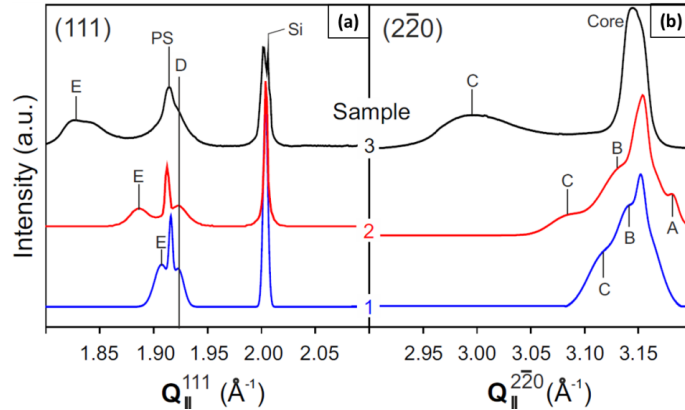
Figure 4.7: (a) and (b) show XRD intensity integration of all samples plotted along scattering vectors $Q_{||}^{111}$ and $Q_{||}^{2\bar{2}0}$, respectively. For better visibility, the curves are plotted with vertical offsets. The position expected for unstrained GaAs in $Q_{||}^{111}$ in (a) is marked by the dashed line near D. Positions expected for unstrained $In_{0.15}Ga_{0.85}As$ [blue], $In_{0.27}Ga_{0.73}As$ [red] and $In_{0.7}Ga_{0.3}As$ [black] are marked by vertical lines and named E in (a) and C in (b), respectively. A graphical explanation of peaks A, B and C is shown in Figure 4.6a. The explanation of the peaks named A to E and peak PS is given in the text.

The main outcome of the XRD analysis is the mean In content of the (In,Ga)As shell in the NW ensembles of samples 1 and 2 listed in the fifth row of Table 4.1. These values are in very good agreement with the nominal values. For sample 3, we measured the mean In content from parasitic islands and suppose that the same In content is incorporated in the NWs.

4.4 nXRF results and discussion

The XRD analysis of the previous section provides an ensemble average for the In content of the (In,Ga)As shell. However, in many cases it is crucial to obtain information about the In distribution within the shell, and for this purpose measurements of individual core-shell NWs are indispensable. In addition, nXRF is the method of choice to measure single NWs in their as-grown configuration on the substrate.

In this experiment, the 111 plane of several individual NWs was probed by a Gaussian X-ray beam with diameter of 50 nm (FWHM). The Gaussian beam shape results in an in-homogeneous fluorescence excitation within the probing area, as sketched in Figure 4.4a. At the marked position, the (In,Ga)As shell is excited by the center of the Gaussian beam, whereas the neighboring GaAs areas are excited by the tails of the beam. In order to determine the true elemental distribution, the fluorescence intensity map has to be corrected for the Gaussian beam profile. To this end, a simulation program was created using a Matlab code that mimics the correct excitation profile at each probing position and normalizes the XRF intensity generated at a certain sample area to the Gaussian incident intensity distribution. The feasibility of this procedure was tested on sample 2, simulating the expected In distribution and assuming a Gaussian beam FWHM of 50 nm × 50 nm, the nominal NW diameter of 280 nm, and an (In,Ga)As shell thickness of 40 nm. The measured total Ga + In signal is shown in Figure 4.8a as a red line and the corrected profile is shown in blue. The FWHM of the blue box reflects the nominal NW diameter very well. The same procedure was applied to the In signal within the (In,Ga)As shell, and the result is presented in Figure 4.8b. Here, the simulated intensity was normalized to unity and the beam corrected In profile is shown in blue. The Ga composition shown in Figure 4.8c was then obtained by subtracting the corrected In signal in Figure 4.8b from the total signal in Figure 4.8a, which reproduces the core-shell-shell composition of the NW. This procedure was applied in a similar way to determine the In and Ga profiles measured for sample 1.
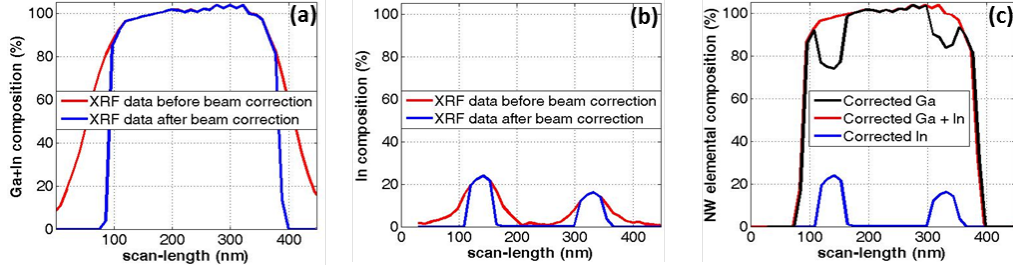
Figure 4.8: (a) Combined Ga and In fluorescence signal along single line scans through the center of the NW before [red] and after [blue] Gaussian beam shape correction. (b) In fluorescence signal along single line scans before [red] and after [blue] Gaussian beam shape correction. (c) Corrected Ga [black], In [blue] and sum of Ga and In [red] signals.

The corrected 2D XRF intensity maps of the In signal averaged over the K_α, K_β and L_γ fluorescence intensities taken from the 111 basal plane of individual NWs of samples 1 to 3 are shown in Figure 4.9 in false color representation. For samples 1 and 2, each data point of the map is an average over the sample area excited by the nano X-ray beam after correction for the Gaussian beam profile. For both samples, we assumed that the In content is homogeneous along the NW length and reaches both detectors mainly through the NW side planes with negligible absorption. For sample 1 (Figure 4.9a) the measured In distribution of a selected NW reflects the hexagonal NW geometry with six well pronounced {110} side facets. In order to probe the homogeneity of the In distribution within the shells, we extracted line scans along each of the six NW side planes marked as LP1 to LP6 by integrating over the respective shell thicknesses, and the measured In fluorescence intensity was normalized to the mean In content of the shell determined from the XRD data [see Table 4.1]. The resulting line scans are shown in Figure 4.9b and 4.9c and reveal a rather uniform In distribution. Differences in In content between the different side facets do not exceed 1.5% [in percentage points]. The In distribution in other single NWs of the same sample shows qualitatively similar behavior (see Figure A4 in Appendix, B).

Figure 4.9d displays the In fluorescence of one selected NW of sample 2. Here, the In signal is not uniformly distributed across the six side planes but shows a significantly lower In content along one of the side planes. In order to quantify these differences, we took line profiles along the x- and the y-direction across the NW basal plane (Figure 4.9e). The mean In signal of the profile extracted in the y-direction was normalized to the In content of 27% found by XRD [Table 4.1]. With this normalization, the line scan along the x-axis cutting a pair of opposite facets reveals maximum In concentrations of 27% and 18.5% at the left and right lobe, respectively (Figure 4.9e). However, we emphasize that

the in-homogeneity in the measured In fluorescence can be explained both by a lower In content and/or a thinner (In,Ga)As shell thickness for the right facet compared to the left one. Because the probing nanobeam is larger than the shell thickness, these effects cannot be distinguished. Additional single NWs measured from this sample show qualitatively similar behavior (see Figure A5 in Appendix B).
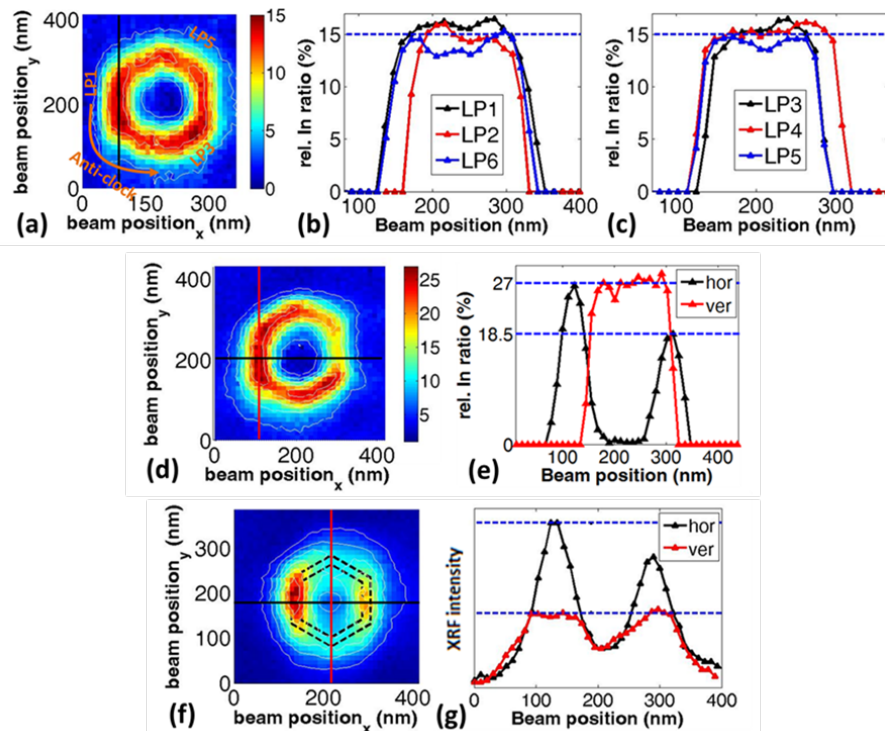
Figure 4.9: (a) XRF intensity map of a single NW from sample 1 after correction for the Gaussian beam profile. The six sidewall facets are labeled counter-clockwise by LP1−LP6. The black line indicates for LP1 the central position of a line profile that was extracted and is displayed in (b). For this line profile, the XRF intensity was integrated across the shell thickness. Similar line profiles were extracted for all six facets and are displayed in (b) and (c). (d) XRF intensity map of a single NW from sample 2 after correction for the Gaussian beam profile. The red and black line mark the positions of the line scans shown in (e), one parallel to a side facet (red) and one across the NW (black). (f) XRF intensity map of a single NW from sample 3. Due to the irregular morphology of the NWs on this sample, the signal could not be corrected for the Gaussian beam profile. The dashed lines represent the expected position of the (In,Ga)As shell. The solid lines indicate the positions of the line scans shown in (g), both across the NW, in the horizontal (black) and vertical (red) direction.

A possible explanation for the differences in In fluorescence observed for the NWs of sample 2 on different sidewall facets is shadowing of the molecular In and Ga beams during shell growth. For a similar sample, TEM revealed for some NWs a notably different (In,Ga)As shell thickness on few sidewall facets, in particular if another NW was close by [17]. We note that for the present study the NW number is higher for sample 2 than for sample 1, which would be consistent with more pronounced shadowing. Also, on sample 1 the spacing between the NWs is homogeneous due to the pre-patterning, while for the unpatterned substrate of sample 2 the spacing varies.

A completely different picture is revealed for the NWs of sample 3 with nominally 60% In concentration in the (In,Ga)As shell. The 2D In distribution of one selected NW from sample 3 is shown in Figure 4.9f. The dotted lines show the expected shape of the (In,Ga)As shell, assuming the nominal NW structure with a GaAs core of 140 nm in diameter surrounded by 18 nm of (In,Ga)As shell. We find that the In fluorescence signal is not uniformly distributed. Instead, it shows strong maxima at certain positions along the shell and much lower intensity in other shell regions. Similar patterns were obtained for other NWs from the same sample (see Figure A6 in Appendix B). Qualitatively, this behavior is visualized in Figure 4.9g by line scans along the x-axis [black line] and y-axis [red line]. Due to the non-uniform NW morphology characterized by the appearance of (In,Ga)As mounds, the Gaussian beam shape correction of the XRF maps was not feasible for this sample, and therefore a determination of shell and mound thickness is not possible. Lewis *et al.* found that for NWs with the same core-shell dimensions and nominal In concentration, the 18 nm thick (In,Ga)As shell splits into a 10 nm thick coherently strained (In,Ga)As shell and thicker plastically relaxed (In,Ga)As mounds [71]. In our study, the larger thickness of the mounds compared to the shell results in a much higher XRF intensity. This effect would explain the differences observed for the scan along the x-axis in Figure 4.9g compared to the line scan along the y-axis. We note that the higher intensity of the mounds compared to the shell does not automatically indicate a higher In content as one has to consider the different excitation volumes.

For a rough comparison between the In concentrations in the mounds and in the shell, we performed atomic force microscopy [AFM] measurements on a side plane of a single dispersed NW taken from sample 3 as shown in Figure 4.10. Above a base line at height of 190 nm, which measures the mean NW diameter, several mounds show up with height between 10 to 50 nm and length between 200 and 300 nm. To correlate the measured XRF intensity with the In concentration, we consider first that the X-ray absorption coefficient of In at 24.00 - 24.21 keV [In L -line] is about $\mu \approx 0.2$ cm^{-1}, meaning that the

measured fluorescence signal is generated within the whole NW. Secondly, we consider that the measured fluorescence intensity, I, is proportional to the number of In atoms, N, within the excited volume. Considering first the XRF intensities measured from the basal plane (Figure 4.9g), and assuming a number density N [number of In atoms per nm^3], the measured XRF intensity is $I \approx N \times V$, where V is the excited volume containing In atoms. Approximating a mean mound length to about $L \approx 200$ nm and the area of extension of the beam to d^2, with $d = 50$ nm, $I_{mound} = N_{mound} \times d^2 \times L = N_{mound} \times 5 \times 10^5$ nm^3. On the other hand, the XRF intensity from the shell is generated in a volume, $V = d \times t \times l$, where t is the shell thickness $[t \approx 10$ nm$]$ and l is the NW length after FIB treatment $[l \approx 2000$ nm$]$. Therefore, the shell intensity is $I_{shell} = N_{shell} \times 1 \times 10^6$ nm^3. Because one supposes that several mounds, Z, are deposited along the NW length (see Figure 4.10) the total mounds XRF intensity is $I_{totalmounds} = I_{mound} \times Z$ which can reach an intensity larger than I_{shell} even if $N_{mound} = N_{shell}$. By these reasons it follows from our experiment that the mean In content in mounds can be only slightly larger [in case of $Z = 1$ or 2] or even smaller than the mean In concentration within the shell.

A similar estimation can be made for the XRF data taken from the side plane (Figure 4.9f). Here, the mound volume excited by the nanobeam is about d^3 considering that the mound height is equal or larger than the beam size and that the mounds extend across the width of a NW side facet. That reasoning gives $I_{mound} = N_{mound} \times 1.25 \times 10^5$ nm^3. Exciting the In within the shells [top and bottom side planes] of thickness t gives $I_{shell} = N_{shell} \times 2 \times d^2 \times t = N_{shell} \times 5 \times 10^4$ nm^3 explaining $I_{mound} > I_{shell}$ for $N_{mound} = N_{shell}$ as seen in the experiment. Following the estimate, we cannot conclude from our XRF experiment whether the In content differs in the mounds and in the coherent shell.
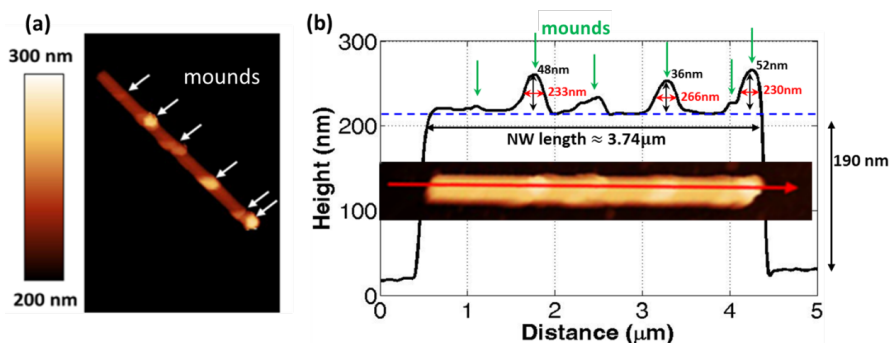

Figure 4.10: (a) Atomic force microscopy image of a dispersed NW from sample 3. (b) Line profile along the NW axis.

During the XRF experiment, we observed that some of the NWs were broken or had grown in an oblique direction with respect to the surface normal. These NWs offer the opportunity to investigate the In distribution along the NW axis. For such NWs, the XRF intensity was not corrected for the beam profile. Figure 4.11a shows the In fluorescence map of such a NW from sample 2. Since these NWs were not treated by FIB, they still display the droplet-like top at one end of the NW, and there the In fluorescence is clearly much higher. In the map of Figure 4.11b, both the In and Ga fluorescence are plotted, each in a different color. Apart from the droplet-like feature at the tip, the fluorescence is fairly homogeneous along the whole NW length. Quantitative information is provided by the line profile in Figure 4.11c, for which the In fluorescence was scaled to the average In content of 27% in the (In,Ga)As shell obtained by XRD. We note that the absolute In fluorescence intensity cannot be compared with the one measured for the vertical NWs since now much less material from the (In,Ga)As shell is probed for each pixel of the scan. At the droplet-like feature at the NW top, the In content is 23% [percentage points] higher than in the NW itself. This result demonstrates the importance of removing the NW tip to retrieve meaningful data for the vertical NWs. However, we would like to point out that on the basis of these data, the In content actually cannot be compared in a quantitative way between tip and the rest of the NW, since the probed amount of In-containing material is at the tip different. Along the NW itself, the In content fluctuates by around 7% [percentage points]. This fairly small variation justifies the averaging done along the NW axis for the XRF results presented in Figure 4.9.

The situation is again different for the NWs of sample 3. Data analogous to the ones discussed in the previous paragraph are shown for a representative NW of sample 3 in Figures 4.11d-f. In this case, the In fluorescence exhibits strong fluctuations along the NW length, to an extent that the droplet-like feature at the tip cannot be clearly distinguished. These local fluctuations of the XRF intensity reach up to 24% with respect to the maximum XRF intensity. These fluctuations are consistent with the fluctuations observed for the vertical NWs and are again explained by the formation of pronounced mounds on the NW sidewalls. These mounds lead to a locally larger volume of (In,Ga)As compared to the coherent shell. In an attempt to learn more about these mounds, we extract one line scan along the NW through its center [red line in Figure 4.11f] and one line scan at the edge of the NW [black line], where the latter crosses preferentially the mounds. Not surprisingly, the relative fluctuations in In fluorescence are stronger for the line scan at the NW edge. However, when approximating the mounds by a box with depth equal to the width of a NW side plane, following the arguments given in SM 3, we still cannot judge whether the In content differs in mounds and shell.
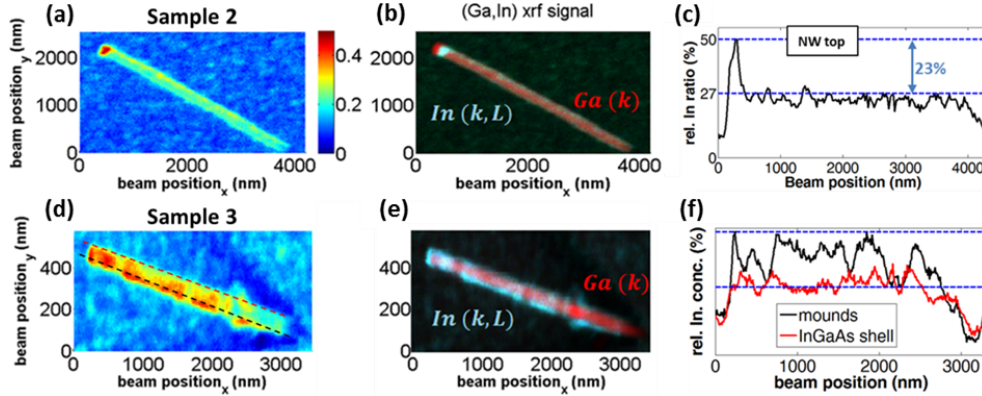
Figure 4.11: XRF measurements of NWs oriented perpendicular to the probing beam. (a) In fluorescence map of a single NW from sample 2. (b) Overlaid map of the In [cyan] and Ga [red] fluorescence. (c) Line profile of the In content along the whole NW length, resulting from normalizing the In fluorescence signal to the average In content of the (In,Ga)As shell determined by XRD. Note that at the droplet-like feature at the NW tip [left-hand side], the probed volume of In is different, and that hence the quantitative value there cannot be directly compared. (d) In fluorescence map of a single NW from sample 3. (e) Overlaid map of the In [cyan] and Ga [red] fluorescence. (f) Line scans of the In fluorescence taken along the NW length through its center [red] and at the NW edge through the (In,Ga)As mounds [black].

4.5 Summary

We have presented two independent and complementary experimental studies of the In content in GaAs/(In,Ga)As core-shell NWs based on X-rays. First, by measuring both the axial 111 and radial $2\bar{2}0$ reflections of NW ensembles using XRD, we were able to disentangle the average In concentration of the (In,Ga)As shell and its thickness despite the ternary nature of the alloy. The resulting values are in good agreement with the nominal ones deduced from growth parameters. Second, we demonstrated on individual NWs the measurement of the spatial In distribution in a 40 nm thick (In,Ga)As shell by nano XRF, employing a Gaussian nanobeam with FWHM of 50 nm. By correcting the measured XRF intensities for the Gaussian beam shape, we were able to identify In fluctuations within the (In,Ga)As shells. Furthermore, by normalizing the XRF signal to the average In content determined by XRD, we obtained quantitative information about the variation in In fluorescence.

NWs with 15% nominal In content in the shell exhibited a fairly homogeneous In distri-

bution between different sidewall facets. In contrast, in core-shell NWs with 25% nominal In content in the shell, we observed significant variations between the In fluorescence on opposite sidewall facets of the same NW. However, we have to point out that this measurement method by itself cannot distinguish between differences in the In content at constant shell thickness and differences in shell thickness at constant In content, since the fluorescence intensity depends only on the total amount of probed In. For the same sample, we found in a different measurement geometry that the In content is fairly homogeneous along the length of the NW. Core-shell NWs with 60% nominal In content in the shell exhibit pronounced fluctuations in In fluorescence, both between different sidewall facets and along the length of the NW. These fluctuations are consistent with the formation of (In,Ga)As mounds on the sidewall facets during growth.

We emphasize that the measurement techniques presented here can be applied to NWs in their as-grown perpendicular configuration on the growth substrate. Thus, these techniques pave the way to correlating at the single-NW level structural information and functional properties depending on the as-grown configuration of the NWs. Finally, these techniques can be transferred to core-shell NWs with ternary shell in general.

Chapter 5

Structural characterization of individual as-grown core-shell nanowires

As it has been discussed and demonstrated in the previous chapter for the NW system of samples 1 and 2, core-shell semiconductor NWs made from III-V materials with low lattice mismatch grow pseudomorphic along the growth axis, i.e. the axial lattice parameters of core and shell materials are the same. Therefore, both structural composition and interface strain of the NW are encoded along directions perpendicular to the growth axis. Due to fluctuations of the supplied growth species during MBE growth, structural parameters such as local shell thickness, composition and strain may differ between NWs grown onto the same substrate. This requires structural analysis of single NWs instead of measuring NW ensembles.

In this chapter, we illustrate a new method to determine the complete structure of individual GaAs/(In,Ga)As/GaAs core-shell-shell NWHSs by means of nXRD using synchrotron radiation. To do so, we sequentially recorded RSMs of Bragg reflections with scattering vector parallel (out-of-plane) and perpendicular (in-plane) to the NW growth axis. From the out-of-plane 111 Bragg reflection, we derived deviations in the hexagonal symmetry and diameters of NWs grown on the same substrate under the same conditions. The radial NW composition and interface strain became accessible by measuring the 2D scattering intensity distributions of the in-plane $2\bar{2}0$ and $22\bar{4}$ reflections, exhibiting well pronounced thickness fringes perpendicular to the NW side planes (truncation rods - TR). Quantitative values of thickness, composition and strain acting on the (In,Ga)As and GaAs shells were obtained via FEM and subsequent Fourier transformation simulating the TRs measured

perpendicular to each of the three pairs of opposing side-facets. Considering the experimental constraints, thicknesses and In content have been evaluated with uncertainty of $\pm$ 2 nm and $\pm$ 1%, respectively. Comparing data taken from different individual NWs, the shell thickness differs between one and the other.

5.1 Introduction and objective

GaAs/(In,Ga)As/GaAs core-shell-shell NWHSs selectively grown by MBE on a patterned Si 111 substrate can be employed for applications in near-infrared optical data communication [15]. Since core and shell(s) are composed of lattice-mismatched materials, mutual strain will be introduced and released towards the outer side planes. As shown by Lewis et al. [71], elastic strain release takes place if the In concentration within the $In_xGa_{1-x}As$ shell does not exceed a certain limit (x< 0.4). Higher In concentrations may lead to an inhomogeneous In distribution within the active layer and result in the formation of statistically distributed mounds on top of the side facets. In the previous chapter, we have demonstrated that the In distribution within 40 nm thick (In,Ga)As shell of individual GaAs/(In,Ga)As/GaAs core-shell-shell NWs could be measured by nXRF. But since the size of the nanobeam (50 nm x 50 nm) was larger than the nominal shell thickness, the latter could not be determined [74]. Here, we determine the thickness and In content of each shell for the same core-shell NW system but with 15% nominal In content and 20 nm (In,Ga)As shell thickness. Knowing these parameters, this can be then deployed to tune the optical properties of these NWHSs. For example, Dimakis et al. observed a shift and broadening in the CL intensity spectrum for the same NW system as a function of a variation in the (In,Ga)As shell thickness and In content along different side facets [15]. On the one hand, these parameters as well as the strain distribution for different systems of single core-shell NWs have been mapped and investigated with nanometer sized X-ray beam using synchrotron radiation by [19, 63, 67, 68, 75]. On the other hand, the most frequently used technique so far to measure shell thicknesses in core-shell NWs is plan-view TEM [17, 76, 77]. However, milling the NW cross section down to approximately 100 nm by the FIB may lead to layer damage, amorphization, redisposition of layers and if done extensively, to destruction of the NW [78–81].

In this chapter, we report for the first time on an alternative relatively non-destructive technique to determine the thickness composition in single core-shell-shell NWs using nXRD. The advantage of our approach is that several single NWs grown on the same substrate can be measured in the as-grown geometry. This makes it possible to study the structural

parameters among different single NWs and correlate observed deviations to additional physical measurements such as PL or CL wavelength and intensities taken from the same NWHS [82–84]. As already shown by Biermanns et al. [85], individual GaAs NWs grown on the same substrate may exhibit different structural parameters. In this consequence, small fluctuations in the NW diameter or shells thicknesses can be expected in the case of NWHS (see later) requesting evaluation of structural parameters from single NWs.

As in-plane Bragg reflections were measured in grazing incidence geometry, the nano-beam strikes the sample almost parallel to the surface of the substrate and illuminates the whole sample along its pathway. To achieve free access to single NWs, we used pre-patterned substrates where a single line of nucleation centers were defined by means of e-beam lithography. By proper alignment of these centers along a particular crystallographic direction, we were able to access individual NWs along the $[1\bar{1}0]$ and $[11\bar{2}]$ crystallographic direction allowing for 3D structural analysis of single NWHS (Figure 5.1a and Figure B1 in Appendix A).

5.2 Samples

The sample was grown by MBE on a pre-patterned Si 111 substrate using the self-catalysed VLS mechanism [32]. Besides arrays of holes with different densities, the mask contains a line of single holes with 10 µm separation along the $[1\bar{1}0]$ direction (Figure 5.1a). NW growth is confined to the holes but the growth of parasitic objects in these holes cannot be completely avoided. The NW core was grown for 30 min at 630 řC reaching an average length of about 3 µm and a diameter of 50 nm [33]. Subsequently, the Ga droplet was consumed using a high arsenic flux. Reducing the growth temperature to 440°C, the GaAs core was capped by a 20 nm thick (In,Ga)As shell with 15% nominal In content followed by growth of a 30 nm thick GaAs outer shell grown at 440°C [15]. With cubic lattice parameters of $\approx$ 5.653 Å and $\approx$ 5.714 Å, respectively, GaAs and $In_{0.15}Ga_{0.85}As$ have a nominal lattice of $\approx$ 1.1% with respect to unstrained GaAs. A sketch of the basal plane of the single NW line, which is the plane parallel to the surface of the substrate, is shown in Figure 5.1a. Here one single NW is marked by an arrow. Rotating the NW axis with respect to the incident beam, the $2\bar{2}0$ and $22\bar{4}$ lattice planes can be probed (marked by blue and green lines). A side view SEM micrograph of the NW chemical composition is displayed in Figure 5.1b. The orientation of the NW crystal lattice is sketched in Figure 5.1c. Using the notations of cubic crystal system, the NW growth axis is parallel to [111]. During further analysis, this direction is defined as the c-axis of the NW coordinate

system. Accordingly, the direction towards the NW edge is defined as the b-axis and is oriented along the $[22\bar{4}]$ direction whereas the direction perpendicular to the NW side facet is defined as the a-axis and is oriented along $[2\bar{2}0]$ (Figure 5.1c).
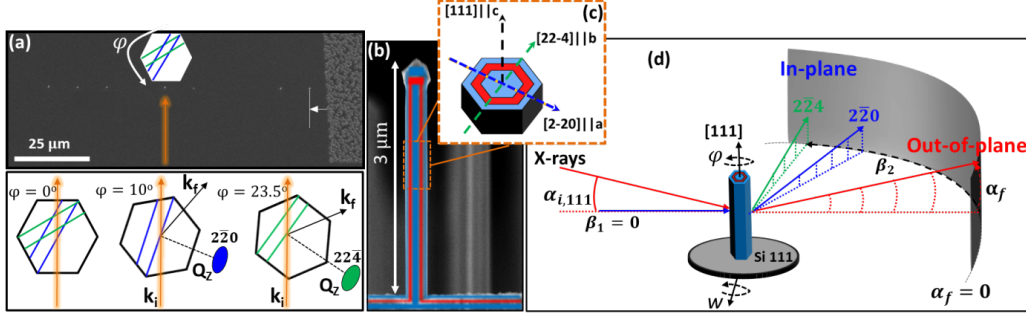

Figure 5.1: Panel (a-top) displays the NW orientation when the incident beam is perpendicular to the NW array shown in SEM. (a-bottom) illustrates the required rotations around the NW azimuth in order to fulfill the Bragg condition with the $2\bar{2}0$ and $22\bar{4}$ NW lattice planes, which are represented by blue and green lines, respectively. (b) SEM micrograph of the NW-sample composition from side view. (c) 3D animation of the core-shell-shell NW with the crystal coordinate system from bird views. (d) demonstrates the experimental geometries used to measure out-of-plane 111, and in-plane $2\bar{2}0$ and $22\bar{4}$ Bragg reflections. The red lines represent the scanning geometry for symmetric 111 Bragg reflection, whereas the blue and green lines represent symmetric $2\bar{2}0$ and $22\bar{4}$ Bragg reflections in GID geometry, respectively.

5.3 XRD experimental setup

The nXRD experiments have been carried out at two different synchrotron facilities, both with photon energy of 9 keV ($\lambda = 1.378$ Å). Out-of-plane and in-plane nXRD measurements were performed at beamline P08 of PETRA III (DESY, Hamburg) [86] where a set of compound refractive lenses was equipped in the beam path providing a beam size of 1.8 µm x 0.6 µm (hor x ver). It is worth to mention that this was the first XRD user experiment performed using a nano-focused beam at the P08 beamline. An additional out-of-plane measurements were executed at beamline ID01 of the ESRF (Grenoble, France) [39] using a nano-beam of 250 nm x 150 nm (hor x ver) defined by inserting a Fresnel zone plate into the beam path. In total six single NWs have been inspected where one NW, named NW2, has been measured in both in-plane and out-of-plane geometries. To access the structural parameters along the NW c-direction, we recorded 3D RSMs in vicinity of the axial 111 Bragg peak (similar to the one in Figure 3.2). The procedure on how to record a RSM

is explained in subsection 2.3.1. Structural parameters along the NW a- and b-directions were probed measuring the $2\bar{2}0$ and $22\bar{4}$ Bragg reflections, respectively (see Figure 5.1c for directions). In both experiments, we used 2D pixel detectors. The experimental geometry for out-of-plane XRD measurements is displayed in Figure 5.1d (red lines). Here, the laboratory coordinate system is defined such as the momentum transfer of the 111 Bragg refection, Q^{111}, is directed parallel to the NW c- axis. In this geometry, the incident and scattering in-plane angles (β_1 and β_2) are set to zero whereas both incident and exit angles (α_i and α_f) of the X-ray beam with respect to the 111 lattice planes are close to the GaAs Bragg angle of $\alpha_i \approx 12.2°$ (see Figure 5.1d for angular notations). Accordingly, RSMs were recorded by rocking the sample by $\Delta\alpha_i = \pm 0.7$ degrees with respect to the 111 Bragg angle using step size of $0.0025°$ and acquisition time of 3 sec. For each step, the intensity distribution was collected by recording a 2D frame using the 2D pixel detector. In total, 600 frames were collected and then composed to plot the 3D intensity distribution as function of the reciprocal space coordinates Q_z^{hkl}, Q_y^{hkl} and Q_x^{hkl} defined by equations 2.12-2.14. Q_x^{hkl} and Q_y^{hkl} are the reciprocal space vectors perpendicular to Q_z^{hkl}, directed along the a-axis and b-axis, respectively. The wave number of the beam is denoted by $K = 2\pi/\lambda$, where λ is the wavelength of the X-ray beam.

5.4 Out-of-plane XRD

Using this geometry, we measured three single NWs (NW1, NW2 and NW3) along the single line of the patterned substrate (Figure 5.1a). The 3D RSMs of the 111 Bragg reflection were recorded at the mid-section of the NWs, away from the NW top and the substrate-NW interface where the scattering intensity did show deviations compared to the central part (Figure 5.2a). Figure 5.2b shows a (Q_z,Q_x) projection of the 3D RSM (integrated along Q_y) recorded for NW1. The most intense peak in the RSM is the Si Bragg peak at $Q_z^{111} \approx 2.004$ Å^{-1}. As expected, a single NW Bragg peak is seen below the Si substrate peak at $Q_z^{111} \approx 1.921$ Å^{-1} (corresponds to d-spacing of $d_{111}^{expt} = 3.271$ Å) demonstrating pseudomorphic growth between GaAs and (In,Ga)As. This verifies our assumption that the two materials share the same axial lattice parameter along the growth direction. Nevertheless, it is worthy to mention that the width of the NW Bragg peak of ≈ 0.0051/Å can originate either from a contribution of the Gaussian beam profile or small strain gradient. The intensity is modulated along Q_x^{111} due to the NW core-shell-shell structure i.e. the thickness fringes measure the NW diameter between one pair of opposite side facets. This will be explained in more details later. Due to pseudomorphic growth, the interplanar d-spacing of the 111 lattice planes within the NW can be estimated using

equation 2.6 i.e. V is the volume ratio between (In,Ga)As and GaAs materials in the NW and x is the In content within the (In,Ga)As shell. Both parameters will be extracted later considering results of in-plane nXRD and FEM modeling. Figure 5.2c shows the (Q_x, Q_y) plane of the 3D RSM cut at $Q_z = 1.921\,\text{Å}^{-1}$ for NW1, seen as a horizontal dashed black line in Figure 5.2b. It displays the Fourier transformation of the hexagonal NW cross-section, visible as a six-sided star in reciprocal space. Perpendicular to the NW side facets, extended TRs with thickness oscillations are visible.
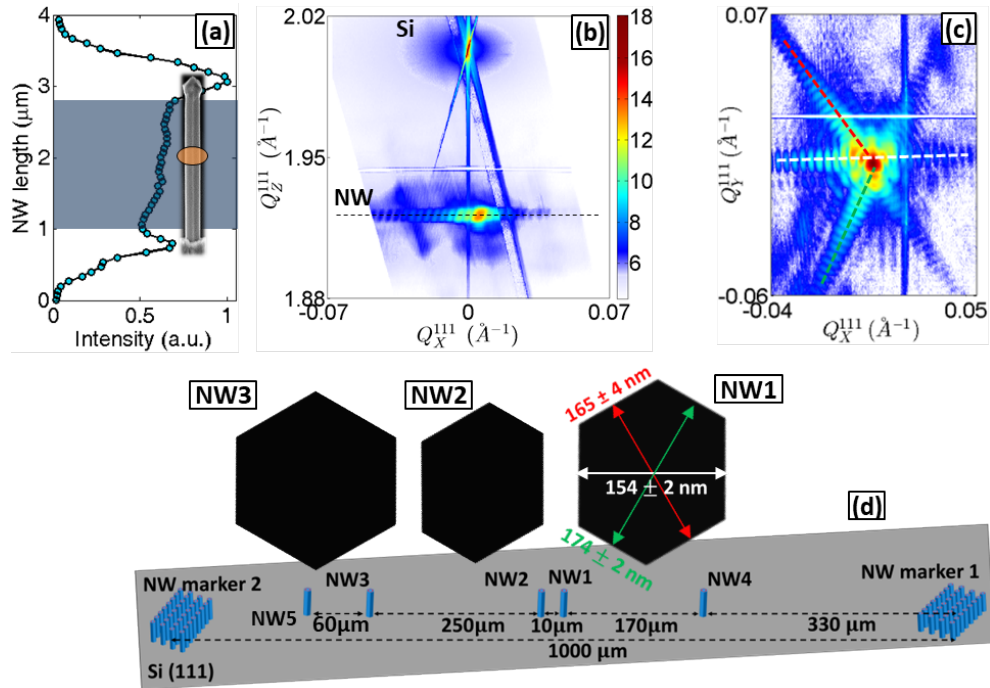
Figure 5.2: (a) Integrated intensity of a scan along the NW azimuth while fulfilling the 111 Bragg condition. The two humps correspond to the Si/NW interface and top section of the NW. The beam position at which RSM was recorded is marked in orange. (b) 2D intensity integration of the 3D RSM in planes oriented along the growth direction of NW1. The top and bottom peaks represent the Si and NW 111 Bragg reflections. (c) 2D (Q_x, Q_y) RSM. The position of the cut in Q_z is indicated by a black line in (b). (d) A schematic of the NW line region bounded by two markers (see Figure B1 in Appendix A, NW array perpendicular to the beam). Cross-sections of NW1, NW2 and NW3, similarly calculated, are colored in black from right to left, respectively. The cross-section of NW1 is estimated from thickness oscillations and orientation of the TRs in the RSM demonstrated in (c). The direction of each pair of side facets is indicated by an arrow in real space and a dotted line of the same color in reciprocal space. NW4 and NW5 are measured only along $[2\bar{2}0]$ or $[22\bar{4}]$, respectively, and will be discussed later in the text.

From the separation ΔQ_{TR} between neighbored maxima or minima along the TR, the thickness, T, between a pair of opposite side facets in real space can be evaluated (see subsection 2.3.1). Comparing ΔQ_{TR} measured along the three different TRs, one is able to reconstruct the entire cross-section of the investigated NW. The evaluated cross-section of NW1, colored in black, is displayed in Figure 5.2d where the diameters between each of the three couples of opposite facets are marked by green, red and white arrows. The same procedure has been performed for NW2 and NW3. Table 1 shows the respective values of the three NWs where the location and cross-section of each NW on the single NW line is displayed in Figure 5.2d. Whereas NW3 displays the hexagonal symmetry pretty well, NW2 and NW1 show deviations from perfect hexagonal shape. Furthermore, the mean diameter differs among the three NWs.

Table 5.1: The NW diameters taken from each couple of opposite facets, marked in red, green and white in Figure 2(b), respectively.

	NW 1	NW 2	NW 3
Red arrow	165 ± 4 nm	138 ± 4 nm	168 ± 5 nm
White arrow	154 ± 2 nm	127 ± 6 nm	161 ± 4 nm
Green arrow	174 ± 2 nm	156 ± 5 nm	164 ± 5 nm

5.5 In-plane XRD

Because of pseudomorphic growth, the axial lattice parameter of core and shell materials is the same and therefore, individual layer thickness and In composition cannot be disentangled (see equation 2.6). However, the complete NW structure becomes accessible measuring along a direction perpendicular to the growth axis. In order to measure an in-plane reflection, the laboratory system has been changed. Here the momentum transfer of the $2\bar{2}0$ Bragg reflection, $Q_z^{2\bar{2}0}$, is set parallel to the NW a-axis, whereas Q_x and Q_y are aligned parallel to b-axis and c-axis, respectively. At the $22\bar{4}$ Bragg reflection, the momentum transfer $Q_z^{22\bar{4}}$ is parallel to the NW b-axis whereas Q_x and Q_y are oriented parallel to a-axis and c-axis, respectively (see Figure 5.1c). To fulfill the Bragg condition with the $2\bar{2}0$ and $22\bar{4}$ lattice planes in real space, the whole sample has to be rotated by about 10° and 23.5° around the NW azimuth with respect to the $[1\bar{1}0]$ normal, respectively, as displayed in Figure 5.1a. For measurement, the angles α_i, α_f and β_1 are set to zero whereas the in-plane detector angle is set to $\beta_1 + \beta_2 = 2\theta_{hkl}$ (see Figure 5.1d). In order to record RSMs of the mentioned in-plane Bragg reflections, the sample is rocked by φ around the NW c-axis in vicinity of the Bragg condition. Accordingly, (Q_z, Q_x)

plane of the 3D RSMs measured along the $[1\bar{1}0]$ NW normal and $[11\bar{2}]$ NW edges of NW2 are displayed in Figures 5.3a and 5.3b, respectively. Each RSM displays several features, labeled by A-F pointing towards specific crystallographic directions.

In order to correlate these features with different components of the core-shell-shell structure, we performed a FEM simulation (details of FEM modeling are introduced later) of a single NW model with the nominal thicknesses of 50 nm/ 20 nm/ 30 nm corresponding to core diameter/ (In,Ga)As shell thickness/ outer GaAs shell thickness and nominal In content of 15% as input and qualitatively compared the simulated with the experimental in-plane diffraction patterns shown in Figures 5.3a and 5.3b. To do so, the NW composition and strain were simulated by applying two dimensional Fourier transformation (FT) of the displacement field calculated in framework of the linear elasticity theory using equation 4.1 [87]. The displacement of the atoms from their unstrained reference positions r can be described by a displacement field u(r), which is obtained by minimization of the elastic energy of the single NW model subjected to a lattice mismatch of 1.1% at the hetero-interface between GaAs and $In_{0.15}Ga_{0.85}As$. The NW shape is described by a shape function $\Omega(r)$, which is unity inside the volume of the object and zero outside. The anisotropy of the crystalline materials was considered by implementing their elastic constants taken from [46] i.e. those of (In,Ga)As were calculated by linear interpolation between GaAs and InAs. Free mesh parameters were used, i.e. the mesh width of the grid varied between 6 and 7 nm at the GaAs core and outer shell away from the hetero-interfaces. Approaching the GaAs/(In,Ga)As interfaces and through the (In,Ga)As shell where high strain gradients are expected, the mesh size was reduced and chosen to be between 1 and 2 nm.

$$A_G(\Delta Q) = \int \Omega(r)e^{iQ.u(r)}e^{\Delta Q.r}dr \tag{5.1}$$

Here, A_G is the scattering amplitude of the Bragg reflection. The diffracting intensity can be obtained by FT of $A_G(\Delta Q)$ considering the displacement field, u(r), projected onto the probed reciprocal lattice vector Q. The simulated diffraction patterns of the $2\bar{2}0$ and $22\bar{4}$ reflections, displayed in Figures 5.3c and 5.3d, show qualitative agreement with the features shown in Figures 5.3a and 5.3b, respectively. In addition, the influence of a certain shell within the NW on the diffraction patterns can be retrieved by eliminating the nodes of the remaining shells from the complete FEM model maintaining the simulated displacement field of the full model. This dissection technique is similar to taking the FT of the resulting displacement field in each NW part whereas the full diffraction pattern is obtained by a coherent FT of the full core-shell-shell NW structure. For example, in

Figure 5.3g, the nodes of the (In,Ga)As shell only are considered in the FT and plotted while those of the GaAs core and cap are excluded. Comparing the resulting features with the diffraction pattern of Figure 5.3a, only the peaks at lower Q_z values carry major information about the (In,Ga)As shell. In particular, feature C is attributed to the $2\bar{2}0$ lattice spacing of the (In,Ga)As shell along the scanned direction while peaks B originate from the neighboring facets tilted by 60° with respect to C. To demonstrate the relation between the labels A-F, shown in Figures 5.3a and 5.3b, and the $2\bar{2}0$ and $22\bar{4}$ diffracting lattice planes, real space images are shown in Figures 5.3i and 5.3j. The NW basal planes in Figures 5.3i and 5.3j are orientated along the same direction as in the reciprocal space diffraction patterns in Figures 5.3a and 5.3b, respectively. The same procedure can be performed highlighting the GaAs cap (Figures 5.3e and 5.3f). Figure 5.3e displays that the peaks at the upper part of the diffraction pattern, marked by A and D, are representing the lattice spacing of the GaAs outer shell along the scanned direction and at the neighboring facets, respectively. On the other hand, the GaAs core displays no major contribution to the total diffraction pattern. The same technique can be used to analyze the $(22\bar{4})$ diffraction pattern. The bottom and upper peaks marked previously by F and E (see Figures 5.3f and 5.3h) represent the lattice spacing of the (In,Ga)As shell and GaAs cap along neighboring facets tilted by $30°$ with respect to the $[22\bar{4}]$ scanned direction, respectively.

For quantitative analysis, first, we transformed the RSMs displayed in Figures 5.3a and 5.3b from Cartesian to polar coordinate system around the intersection point of the dotted lines. The corresponding RSMs are plotted in Figures 5.4a and 5.4b setting $Q_x = 0$ as zero point of the azimuthal rotation φ shown as vertical axis in the figures, whereas the horizontal axis is denoted as Q_r. This figure displays the TRs of all NW side plane as lines parallel to the horizontal axis. Second, we extracted line profiles (LP) along the vertical (VLP) and diagonal (DLP) TRs of the $2\bar{2}0$ 2D RSM, marked by dotted lines in Figure 5.3a and labeled by VLP1 and DLP1-DLP2 in Figure 5.4a and same for TRs of the $22\bar{4}$ RSM, marked by dotted lines in Figure 5.3b and labeled by VLP2, DLP3-DLP4 in Figure 5.4b. The mentioned LPs are plotted in Figures 5.4c and 5.4d, respectively. Considering Figures 5.3 and 5.4, RSMs recorded along directions perpendicular to the NW growth axis are rich in features encoding the specific radial structure of the measured NWHS. In particular, the TRs show pronounced thickness oscillations which can be used to determine shell thicknesses and interface strain.
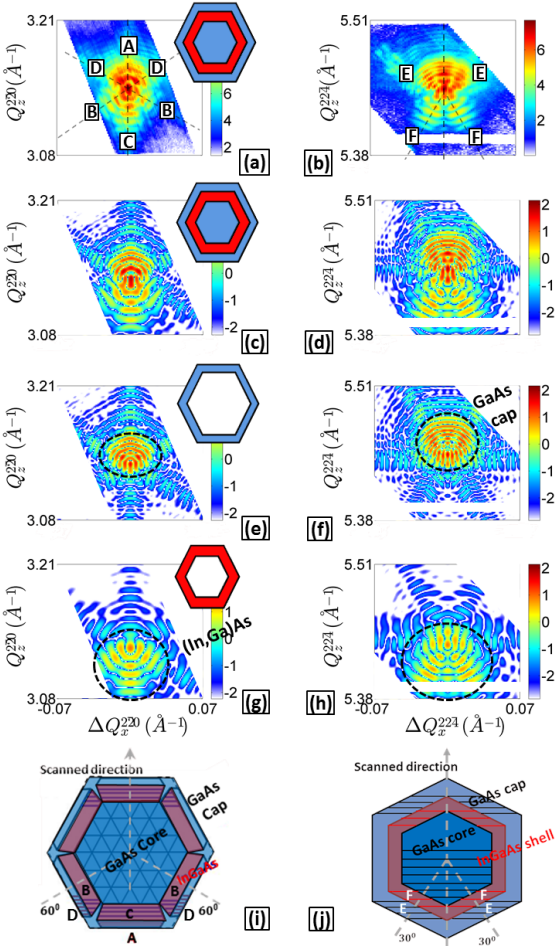
Figure 5.3: (a) and (b) XRD RSMs in the Q_{yx} plane of the $2\bar{2}0$ and $22\bar{4}$ Bragg reflections, respectively. The scanned direction is represented by the vertical dotted line at $Q_x = 0$. (c) and (d) show FEM simulations of the $2\bar{2}0$ and $22\bar{4}$ Bragg reflections of a single core-shell-shell NW model, respectively, using the nominal dimensions. (e) and (f) are similar to (c) and (d), respectively, but with subtracting the displacement field of the GaAs core and the (In,Ga)As shell. (g) and (h) are constructed by subtracting the displacement field of the GaAs core and outer shell from the total displacement field, respectively. (i) and (j) display real space NW models that explain RSMs shown in (a) and (e), respectively. Lines labeled C and A represent the $2\bar{2}0$ crystallographic planes of the (In,Ga)As and GaAs shell facets indicated in the scheme, respectively. Peaks B and D correspond to the $2\bar{2}0$ planes of the (In,Ga)As and GaAs shells in neighboring facets. As $2\bar{2}0$ RSMs provide strain information about the shell side facets only, areas close to the NW edges are kept empty in the scheme neglecting possible local variations in strain and In content. Peaks F and E correspond to the $22\bar{4}$ lattice planes of the (In,Ga)As and GaAs shells in neighboring facets, respectively. Peaks A, B, C, D and E are explained in (i), (j) and text.

5.6 FEM modeling of the TRs

Unfortunately due to specific scattering geometry, the Si Bragg peak, which could be used as a reference, was not accessible and due to their rather similar scattering volumes (see Table 4.2), shells and core contribute with rather similar scattering amplitude to the total scattering pattern. Therefore, an appropriate model is required to evaluate the structural parameters of the NWHS via simulation of the experimental data. Here, we used finite element modeling in terms of Comsol as a tool for data analysis. All details about the anisotropy and mesh size are the same as presented in the previous section. In addition, we implemented a core-shell-shell NW model with perfect hexagonal geometry and identical structural compositions for opposite side facets and used the nominal radial composition as initial input.

As shown in Figure 5.3, the 2D FT of the model calculated along the $[1\bar{1}0]$ or the $[11\bar{2}]$ direction shows qualitatively similar features as the measured RSM. However, in order to achieve full agreement between FEM and the XRD patterns, we simulated all measured TRs using distinct NW models of perfect hexagonal shape. To do so, we extracted line profiles along the TRs from FEM in similar way as done for the experimental data, i.e. we simulated the XRD lines scans VLP1, DLP1,2 for $2\bar{2}0$ and VLP2 and DLP3,4 as shown in Figure 5.4. The best agreement with the experimental data was achieved by varying thicknesses of the shells in small steps and the In content of the (In,Ga)As shell inside the NWHS model within the range of $\pm$ 1%. The agreement of the NW model (red curves) with the experiment (black lines) for the $2\bar{2}0$ data are shown in Figure 5.4c.

As DLP3 and DLP4 are tilted by 30° with respect to the $[2\bar{2}4]$ scanning direction, the two LPs represent two neighboring $\{1\bar{1}0\}$ facets. This explains why DLP3 and DLP4 were successfully fitted using the same FEM models as used for fitting the $2\bar{2}0$ data. In contrast to this, VLP2, extracted from $22\bar{4}$ reflection along the NW edge, had to be fitted with different structure parameters (60 nm/ 30 nm/26 nm GaAs/(In,Ga)As/GaAs) compared to the direction perpendicular to the NW side plane DLP1. Without detailed discussion, this finding can be a hint of either faceting or In segregation at the NW edges which has been reported previously for various core-shell NW systems [56, 88–90]. Combing the fitted NW shell thickness along VLP1, DLP1 and DLP2, we were able to retrieve the true NW cross-section from the in-plane experimental data (Figure 5.4e) displaying a deformed hexagonal shape for NW2. The estimated thicknesses from the $2\bar{2}0$ Bragg reflection show rather good agreement with the NW cross-section evaluated from 111 reflection of NW2 (Figure 5.4f).
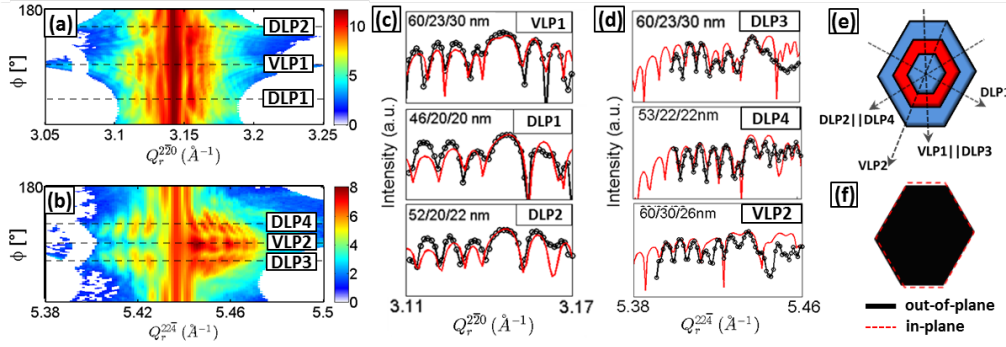
Figure 5.4: Panels (a) and (b) display the $2\bar{2}0$ and $22\bar{4}$ RSMs of NW2, plotted in Figures 5.3(a) and (b), in polar coordinates, respectively. (c) and (d) demonstrate the compatibility between the FEM simulations (red) based on the thicknesses indicated at the top of the diagrams and the experimental XRD data (black) along VLP and DLP1-DLP4. The mentioned LPs are named accordingly and marked by dotted horizontal lines in (a) and (b). (e) illustrates the NW cross-section predicted from the FEM fittings along $[2\bar{2}0]$ in (c). (f) shows the compatibility between the NW cross section evaluated from out-of-plane (black cross-section) and in-plane (red dotted line) measurements.

More than 35 FEM models were executed to reach the best agreement. It turns out that at given experimental conditions the thickness of a single layer can be determined by an accuracy of ± 2 nm and the In content of the (In,Ga)As shell by $\pm 1\%$. As seen in Figure 5.5 (blue and green dashed circles) and Figure B2 in Appendix A, variations of 3 nm in shell thickness or 2% in In content result in a visible angular shift of the outer oscillations, respectively. Figure 5.5 shows a selection of the GaAs/(In,Ga)As/GaAs NWHS FEM models used to fit VLP1 (Figure 5.4c). The best fit was achieved for a NWHS model with thicknesses of 60 nm/23 nm/30 nm (green dashed circle). To demonstrate the precision of the fitting process, the (In,Ga)As shell thickness was varied by 3 nm which resulted in a visible shift of the outer oscillations (blue dashed circle). Furthermore, FEM simulation using the nominal values of core diameter and shell thickness shows bad agreement with the XRD line profile (orange dashed circle).

As a second approach, we fitted all three TRs simultaneously considering the deformed hexagonal NW model. For simplicity of the FEM NWHS model, the analysis was carried out under the assumption that the structural composition of opposite side facets is identical. To do so, again we extracted line scans from the FT of the FEM model similar to the procedure explained for Figure 5.4. The FEM LPs again showed good agreement with the experimental XRD LPs (see Figure 5.6). The agreement of the fit results using both approaches reveals that the strain acting at all pairs of opposite side facets behave rather
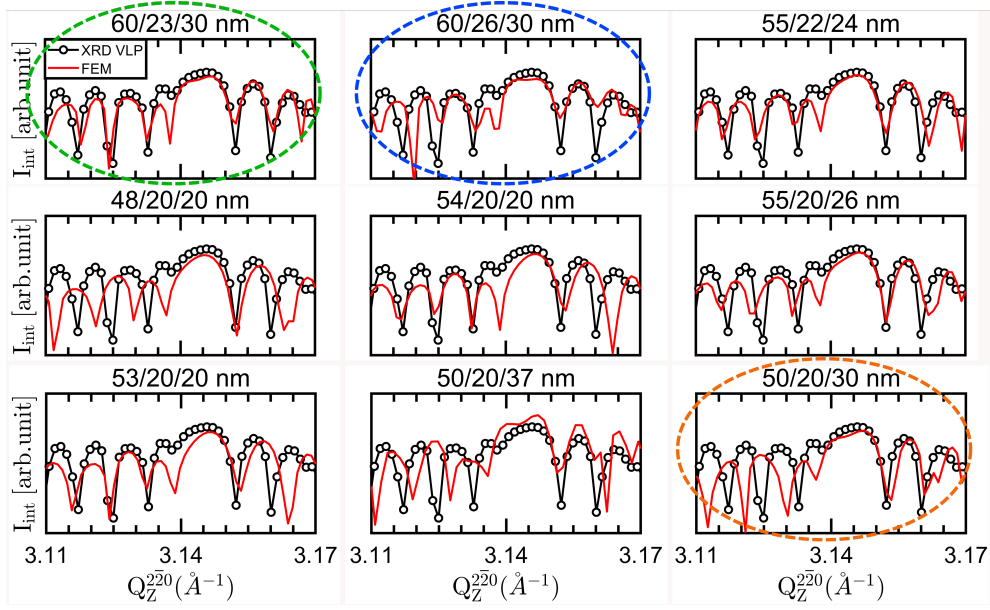
Figure 5.5: Portion of the GaAs/(In,Ga)As/GaAs combinations used in FEM to fit the VLP1 line profile from the $2\bar{2}0$ RSM plotted in Figure 5.4a. The XRD LP is colored in black whereas the FEM LP is colored in red. The FEM simulation of the 60 nm/23 nm/30 nm NW model, marked by a green circle, shows the best fit with respect to the experimental data. Varying the (In,Ga)As shell thickness by 3 nm, the FEM simulation does not longer fit the XRD LP precisely. This is marked by a blue dashed circle. FEM of single NW model with the nominal dimensions is marked in orange.

independent with respect to each other. Therefore, the approach of fitting three hexagonal models to the same NW, (which is easy to implement in FEM) can be applied without major restriction in accuracy of the fits. As a result, our full analysis reveals that the cross-section of NWs shows severe deviation from the hexagonal symmetry. In the same manner, two additional NWs were measured only along $[2\bar{2}0]$ or $[22\bar{4}]$. These are NW4 and NW5, respectively, marked in Figure 5.2d. As shown in Figure B3 in Appendix A, the recorded RSMs of the two NWs show similar features as NW2. However, detailed data analysis reveals that the structural parameters of both NWs differ from those evaluated for NW2. In contrast to NW2, NW4 exhibits perfect hexagonal symmetry (see Figure B4 in Appendix A). On the other hand, NW5 shows different shell thicknesses compared to NW2 (Figure B5 in Appendix A).
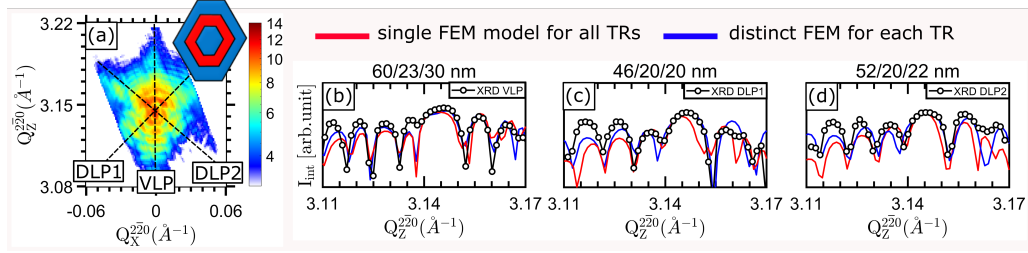
Figure 5.6: (a) RSM of the $2\bar{2}0$ Bragg reflection of the NW displayed in Figure 5.3a. On the top right corner, the predicted NW cross-section is plotted. (b-d) demonstrate FEM simulations and XRD LPs of VLP, DLP1 and DLP2. FEM simulations of distinct NW models for each TR are colored in blue whereas FEM LPs extracted from the NW model plotted in (a) are colored in red. XRD line profiles are colored in black.

As a result of fitting the experimental data, the implemented FEM NW model represents the complete structure of the NW measured by the experiment. Subsequently, one can extract further parameters from the model which are not directly accessible from the experiment. One of these parameters is true composition of the NW cross-section i.e. we are able to calculate the (In,Ga)As/GaAs volume ratio of NW2 to be $V \approx 0.31$. With this value and using the fitted In content $x = 0.15 \pm 0.01$, we can calculate the 111 lattice spacing by equation 2.6. This yields $d_{111}^{\text{expt}} = 3.275$Å, which is in good agreement with the d-spacing calculated directly from the 111 XRD measurement in Figure 5.2b. With these values, one can determine the epitaxial strain acting at the (In,Ga)As shell and the GaAs layers, ϵ_c^{GaAs} and $\epsilon_c^{\text{(In,Ga)As}}$, respectively, using equation 2.7. Here, the inter-planar spacing of the 111 lattice planes for unstrained (In,Ga)As and GaAs are represented by $d_{111}^{\text{(In,Ga)As}}$ and d_{111}^{GaAs}, respectively.

The epitaxial strain ϵ_c, acting along the c-axis of the GaAs core and the GaAs cap shell is tensile whereas the strain at the (In,Ga)As shell along same direction is compressive (Table 4.2). This is qualitatively demonstrated in Figure 5.7a which shows 2D map of ϵ_c taken at the mid-section of the FEM NW model. Figures 5.7b,c show 2D cuts of ϵ_a and ϵ_b taken at the same position. With the help of FEM, we determined the strain values alongside facets (ϵ_a) and edges (ϵ_b) of each layer inside the NWHS. The strains along the $[2\bar{2}0]$ (a-axis) and $[22\bar{4}]$ (b-axis) directions were extracted by line scans taken through a pair of opposite side facets and a pair of opposite edges of NW2 i.e. the first is colored in blue and the second is colored in red (Figure 5.7d). The two lines are indicated in Figures 5.7b and 4.6c, respectively. Interestingly, different strain gradients were obtained at both hetero-interfaces which are indicated by horizontal blue and red boxes that resemble the core-shell-

59

shell NW configuration in Figure 5.7d. Qualitatively, as a result of tensile and compressive strains along the NW axis, the GaAs cap and the (In,Ga)As shell undergo compressive and tensile strains along the NW side facets and edges, respectively. Since ϵ_c, ϵ_a and ϵ_b have different values, both shells experience orthorhombic deformation. Interestingly, the core undergoes tensile strain along all three directions. This finding has been reported before for elastic strain calculations and FEM simulations of cylindrical and hexagonal GaAs/GaP coreshell NWs [44]. This has been reported also for GaAs/(In,Ga)As core-single-shell NWHS [91]. In addition, the in-plane strain is not homogeneous throughout the (In,Ga)As and outer GaAs shells. Quantitatively, the strain gradients $\Delta\epsilon_a$ and $\Delta\epsilon_b$ and the strain values through and at the center of each layer, respectively, are listed in Table 4.2. The strain gradients at the GaAs core, (In,Ga)As shell and GaAs outer shell were estimated considering the strain accommodation between points labeled by (1) and (2), (3) and (4), and (5) and (6), respectively, in Figure 5.7d (see values in Table 2). Different strain values were obtained for NW4 (see Table B1 in Appendix A) but similar to NW2, tensile strain was observed along all directions at the GaAs core whereas both shells have undergone orthorhombic deformation. In addition, NW4 shows higher strain gradient across the radial interfaces of the NW edges. Comparing Table 4.2 and Table S1 in the supplement, the strain gradients across the GaAs core, (In,Ga)As shell and GaAs outer shell of NW4 are 0.2, 0.55 and 0.25 higher than for NW2.
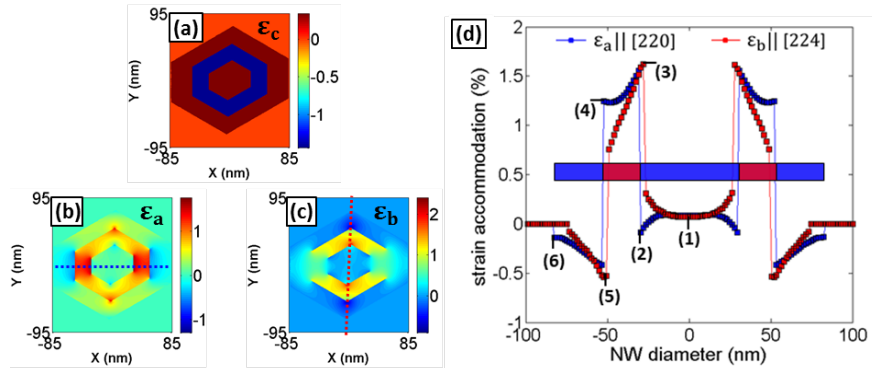
Figure 5.7: (a-c) show 2D cuts of the epitaxial strain ϵ_c, and in-plane strains ϵ_a, and ϵ_b, taken at the mid-section of the NW model. (d) local strain distribution taken at the mid-section of the FEM NW model through opposing side facets and edges named (ϵ_a) and (ϵ_b). The lines are marked by blue and red dotted lines in (b) and (c), respectively. The blue and red horizontal boxes represent the core-shell-shell NW configuration.

Table 5.2: Core diameter and shells thicknesses, volume ratios and fitted In content are shown in the first five rows. The strain values indicated by ϵ and estimated at the centers of the GaAs core, (In,Ga)As shell and GaAs cap along [111], [2$\bar{2}$0] and [22$\bar{4}$] of NW2 and the strain gradients at each layer are shown below. Values inside absolute modulus represent the strain values at each interface of the corresponding layer, labeled by (1) to (6) in Figure 5.5b. Strain values and gradients were extracted from Figure 5.5b.

at center	GaAs core	(In,Ga)As	GaAs cap
VLP1 (nm)	60	23	30
DLP1 (nm)	46	20	20
DLP2 (nm)	52	20	22
In content	—	0.15 ± 0.01	—
Vol. fraction	0.14	0.31	0.55
ϵ_c^{111} (%)	+0.32	-1.45	+0.32
$\epsilon_a^{2\bar{2}0}$ (%)	+0.08	-1.27	-0.25
ϵ_b^{22-4} (%)	+0.07	+1.12	-0.28
strain gradients	|(1) - (2)|	|(3) - (4)|	|(5) - (6)|
$\epsilon_a^{2\bar{2}0}$ (%)	0.17 |0.09, -0.08|	0.31 |1.56, 1.25|	0.28 |-0.42, -0.14|
ϵ_b^{22-4} (%)	0.45 |0.07, 0.52|	1.32 |1.8, 0.48|	0.7 |-0.76, -0.06|

5.7 Summary

Out-of-plane 111 nXRD measurements revealed that, on the one hand, GaAs and (In,Ga)As with 15% nominal In content share the same lattice parameter along the NW growth axis regardless of any variation in the total thickness of the NWs. On the other hand, it has been revealed that neighboring NWs grown under the same conditions display deviations from the nominal total NW thickness and from the perfect hexagonal symmetry. Furthermore, we demonstrated that a detailed characterization of the NWHS, i.e. shell thicknesses, In content and strain values can be obtained for each layer inside the NWHS by mapping the 2$\bar{2}$0 and 22$\bar{4}$ in-plane Bragg reflections and fitting the parameters of a FEM NW model to the experimental data. It turns out that the entire structure can be obtained by modeling the experimental 2$\bar{2}$0 and 22$\bar{4}$ RSMs only, i.e. without the data of the 111 reflection, because both in-plane reflections encode the radial structure of the GaAs/(In,Ga)/GaAs core-shell-shell NWHS. From the model, one is able to extract further parameters such as strain values and strain gradients pointing along all three directions of the NW system which differ in amount comparing different NWs. However, in all NWs, it was observed that the GaAs core undergoes tensile strain along all directions. We emphasize that the measurement and simulation techniques presented here can be applied to NWs in their as-

grown perpendicular configuration, when suitable mask designs are used for selective area growth. This paves the way to correlate structural information to functional properties of a single NW. Finally, our approach can be applied to core-shell NW systems with similar lattice mismatch.

Chapter 6

Structural and optical correlation of individual as-grown core-shell nanowires

In this chapter we discuss the direct correlation between the structural and optical properties of several single core-multi-shell GaAs/In$_{0.15}$Ga$_{0.85}$As/GaAs/AlAs/GaAs NWs grown by molecular beam epitaxy onto a pre-patterned Si 111 substrate. Due to alignment of electron beam lithography drilled and well separated holes along a single line, it was possible to access individual NWs and investigate both properties in the as-grown geometry. The polytype distribution along the NWs growth axis was revealed by synchrotron beam assisted nXRD techniques such recording RSMs and performing SXDM around the axial 111 Bragg reflection. The optical properties of the same NWs were extracted by home lab CL measurements. Comparing both, we reveal a correlation between optical yield and a particular structural phase within the NWs. In particular, we found optical yield of a mixed phase enhanced up to a factor of ≈ 80 in comparison to the WZ and ZB polytypes. The presence of this mixed phase was later confirmed by cross-sectional TEM of a core-shell NW grown on a different substrate but with the same growth parameters. This finding can be exploited to enhance the optical properties of NW based devices such as for solar cells and light emitting devices.

6.1   Introduction

Semiconductor NWs, regardless if homo- or hetero-structures, grow mainly in the cubic ZB with an atomic stacking of ABCABC- [6,21,22] and/or the hexagonal ABABAB- stacked WZ phases [6,23,24] but usually mixed phases of the two polytypes (e.g. M phase) [29,92],

stacking faults [93] and inclusions of twin planes [26,27] may modify the crystal structure. For core-shell NWs, within the elastic strain regime where pseudomorphic growth is expected to take place between the core and shell(s), the crystal structure of the shell(s) is expected to be similar to that of the core. As different phases can possess different structural properties, such as energy gaps and electronic band structures [1], a change in the spatial distribution [94–96] or segment length of crystal phases [97] will result in different band gap alignment within the NW and will therefore directly influence the optical and electronic emission of semiconductor NW devices. Furthermore, NWs grown on the same substrate under the same conditions may possess different structural parameters and crystal phases. Therefore, the structural to optical correlation should be done for single NWs as ensemble measurements would only provide average information. This kind of correlation has already been carried out on NWs of various semiconductor materials [58,94] i.e. the phase structure has been forever investigated by cross-sectional HR-TEM. However, this process requires milling the NW down to less than 100 nm which could remove internal stresses and could possibly induce changes in the phase structure within the NW. As recent technological applications demand the use of NWs in their as-grown geometry on the substrate [18,98], a relatively less destructive technique is nXRD provided by synchrotron nano-focused beams where one can probe the three dimensional internal structure of the NWs.

The effects of polytypism on the optical properties and band structure of individual Ga(N)P NWs have been recently addressed by Dobrovolsky et al. in 2015 [94]. Accessing the optical properties by CL mapping and the structural properties of the same NWs by TEM, the authors have demonstrated that ZB rotational twins in GaNP NWs have detrimental effects on light emission intensity at low temperatures by promoting non-radiative recombination processes. They have also shown that the formation of the WZ polytype has no major influence on the CL intensity in the GaNP alloy. In a different work, the structural and optical properties of GaAs/AlGaAs core-shell NWs were investigated by Bolinsson et al. in 2014 [58] using similar techniques as in [94]. The authors have illustrated enhancement in the CL emission intensity when increasing the GaAs NW core growth temperature, relating it to the formation of rotational twins in the core. As listed in few of many examples, the optical and structural properties of the WZ, ZB and TZB polytypes in various NW systems have been previously addressed by means of CL and TEM measurements. Nevertheless, the CL emission has not been yet recorded for a mixed crystal phase of the mentioned polytypes in III-V core-shell NWs. In addition, this combined correlation was never achieved from the same NW in the as-grown geometry. The advantage of our work is that the contact between the Si substrate and the NWs was

never lost as all measurements were executed in the NW as-grown geometry.

In this work, we investigate $GaAs/In_{0.15}Ga_{0.85}As/GaAs/AlAs/GaAs$ core-multi-shell NW heterostructures. It has been demonstrated that growing an (In,Ga)As shell coherently sandwiched in between GaAs core and outer shell can lead to core-multi-shell NW quantum wells forming good candidates for light-emitting-diodes [15]. Hanno et al. have recently demonstrated that radially grown $GaAs/In_{0.15}Ga_{0.85}As/GaAs/AlAs/GaAs$ NWs show the highest CL emission at room temperature compared to $GaAs/In_{0.15}Ga_{0.85}As/GaAs$ (system1) and $GaAs/In_{0.15}Ga_{0.85}As/AlAs/GaAs$ core-multi-shell NWs (system2) [33]. On one hand, the additional AlAs barrier improves the luminous efficiency of core-shell NWs of system1 at room temperature. On the other hand, compared to system2 and with adding a GaAs spacer in between the (In,Ga)As and AlAs shells, the CL emission from the (In,Ga)As shell QW was calculated to be one order of magnitude higher. In this work, we focus on the optical aspect of this NW system.

The aim of the present work is to find a correlation between the optical and structural properties of individual core-multi-shell NWs for the first time in their as-grown geometry. In this regard, the optical properties of three single NWs were investigated by measuring the CL intensity maps along their growth axes. The structural properties of the same NWs were revealed by two nXRD measurements using synchrotron radiation. The first was a pre-characterization experiment which was performed before the CL measurement. There, we have recorded RSMs in the vicinity of the axial 111 Bragg reflection almost at the midsections of the investigated NWs. The second was to reveal the polytype distribution along the growth axes of the same NWs using quick SXDM and it was executed after CL. To confirm the polytype distribution measured by nXRD, complimentary TEM measurements were done on an individual core-shell NW grown on a different substrate but using the same growth parameters.

6.2   Sample

Several individual GaAs/(In,Ga)As/GaAs/AlAs/GaAs core-multi-shell NWs grown on a patterned Si 111 substrate have been investigated. The nominal dimensions of the NW core and shells are 50 nm/10 nm/5 nm/20 nm/10 nm. The nominal indium content within the (In,Ga)As shell is 15%. Prior to MBE growth, holes with separation of 10 µm were defined in the thermally oxidized silicon substrate using EBL along a 1 mm straight line connecting two 50 x 50 µm^2 square markers (Figure 6.1a,b). The NWs were then grown

preferentially out of these holes by molecular beam epitaxy using the VLS mechanism whereas the two square markers were dominated by parasitic growth. Details about the growth parameters can be found elsewhere [32,33]. The NWs are assigned by NWA where A is the number of the investigated NW. To locate the NWs of interest, first, supported by an optical microscope, the straight line of NWs was aligned perpendicular to the incident beam direction, assigned by the y-axis of the sample coordinate system (see Figure 6.1b). Being parallel to the NW array, the edges of the markers were simultaneously aligned perpendicular to the incident beam (along x-axis). Second, setting the Bragg angle to that of the GaAs 111 Bragg reflection and translating the marker across the beam along x and y, we fixed the X-ray nano-beam to the center of the marker. Finally, using the SEM extracted positions of the NWs with respect to the center of the marker, NW1-NW3 could be located and measured. The three single NWs investigated by CL and nXRD are zoomed in and displayed in Figure 6.1c. The NW core- multi-shell composition and orientation with respect to the sample coordinate system are animated in Figure 6.1d.
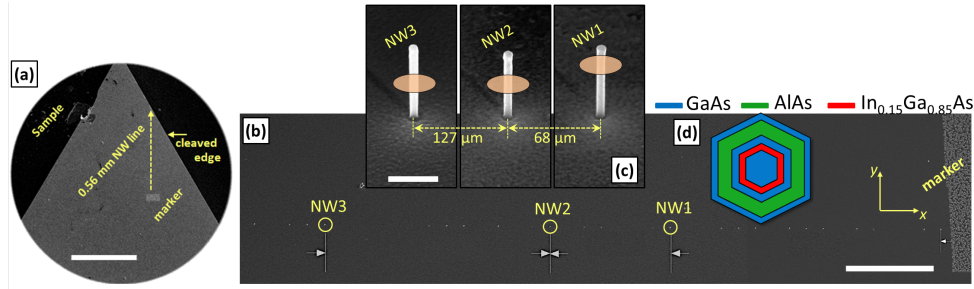

Figure 6.1: (a) Sample after cleaving. Part of the NW line is cleaved during the process i.e. only 0.56 mm are left. (b) SEM micrograph of the NW line near the marker. NW_1-NW_3, seen as white dots, are marked by yellow circles and named accordingly. x and y are the translation directions of the sample, perpendicular and parallel to the incident beam direction, respectively. (b) SEM zoom in of NW_1, NW_2 and NW_3. (c) Animation showing the NW core-shell structure and orientation when the incident beam is perpendicular to the NW line. The scale bars in (a), (b) and (c) are 500, 50 and 1 µm, respectively.

6.3 Experimental part

Prior to the CL measurements, a pre-characterization nXRD experiment was carried out at beamline P08 of PETRA III [86] with photon energy of 9 keV ($\lambda = 1.378$ Å) and beam size of 1.8 µm x 0.6 µm (hor x ver). The structural parameters and phase composition within about 600 nm (vertical beam size) along the growth axes of NW1-NW3 have been accessed by recording 3D RSMs of the 111 Bragg reflection at the mid sections of NWs 2

and 3 and at the top section of NW1 (Figure 6.1c). Usually, we record such maps at the mid-section in order to avoid stacking faults or defects expected at the substrate to NW interface or top NW section. To avoid repetition, the same coplanar geometry explained in [14] was used to scan the symmetric 111 Bragg geometry.

Figure 6.2a shows a 3D isosurface RSM of the 111 Bragg reflection recorded at the mid to top section of NW1. Here, the momentum transfer of the 111 Bragg refection, Q_z^{111}, is directed parallel to the NWs growth axes whereas Q_x^{111} and Q_y^{111} are the reciprocal space vectors defined perpendicular to Q_z^{111}. The respective 2D projections are attached to the sides and bottom of the 3D plot. Similar 3D RSMs were recorded at the mid-sections of NW2 and NW3. The Si Bragg peak has been measured but is not added to the 3D plot. However, it was considered as a reference value ($Q_z^{111} = 2.004$ Å^{-1}) in order to determine the exact angular positions of the NW Bragg peaks. Three distinct peaks, named peaks 1, 2 and 3, are visible at different Q_z^{111} values. Peak 1 reflects the high contribution of the ZB polytype at the illuminated section of NW2. A possible explanation of peak 2 is the presence of the 4H polytype. Alternatively to 4H, the disordered M phase as suggested by Johansson et al. [29] could cause similar contributions to the measured RSM, since the 4H polytype and M phase have the same hexagonality h = 0.5. As complimentary TEM, which shall be discussed later in more details, reveals no extended 4H segments but shows a mixture of different polytypes and faulted segments (see later Figure 6.4), we will address Peak 2 by the M phase. The WZ peak (peak 3) is also visible but with much lower intensity compared to peaks 1 and 2. Interestingly, integrating the 3D RSMs along Q_x^{111} and Q_y^{111} of the three NWs, the obtained line scans show relatively higher M phase contribution compared to WZ (Figure 6.2b). Due to the lattice mismatch between the core and the (In,Ga)As shell, ZB is slightly shifted in Q_z^{111} from the position expected for unstrained GaAs, marked by a vertical dotted line in Figure 6.2b.

The 2D RSM at the bottom shows the (Q_x^{111},Q_y^{111}) plane extracted from the 3D RSM at $Q_z^{111} = 1.921$ Å^{-1}. As explained in Chapters 3 and 5, comparing Q_{TR} measured along the three different truncation rods in the RSM, one is able to calculate the thickness along all three opposing side facets, marked by orange, red and green dotted lines in Figures 6.2a and 6.1c. This makes it possible to reconstruct the entire cross-section of the investigated NWs. The cross-section of NW1 is displayed in Figure 6.2c. Following this procedure, the same NW cross-section was achieved from the M phase Bragg peak, showing that both Bragg peaks originate from the same NW. The cross-sections of the three NWs are demonstrated in black in Figure 6.2d whereas NW cross-sections with nominal total diameter of 140 nm are colored in gray and positioned on top of the black ones. All NWs display the hexagonal

symmetry pretty well and show only slight variation from the nominal dimensions.
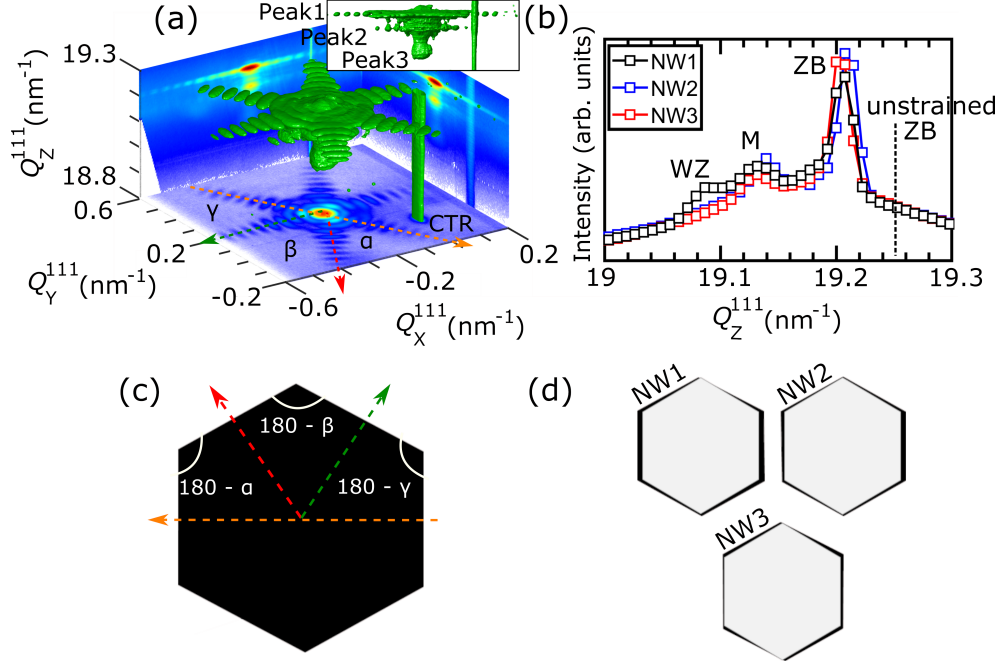

Figure 6.2: Panel (a) 3D RSM of the 111 Bragg reflection for NW1. A side view is displayed at the top right corner showing the presence of 3 Bragg peaks. The 2D projections are added to the sides and bottom. , and are the angular separation between neighboring TRs indicated by orange, red and green dotted arrows, respectively. A side view of the 3D Bragg reflection is placed at the top right corner. (b) Integration of the 3D Bragg reflection along Q_x^{111} and Q_y^{111} for all three investigated NWs. The NWs show pronounced ZB and M phase but lower WZ contribution. (c) The constructed cross-section for NW1. (d) The reconstructed cross-sections of the three measured NWs colored in black. The cross-section of the NW with nominal dimensions is placed on top of each NW and marked in gray. Table 1: Numerical values of thicknesses separating all three pairs of opposing side facets and angular orientation of neighboring side facets indicated by colored dotted lines and indicated in white in Figure 1c, respectively. In addition, the NW tilt with respect to the normal of the silicon substrate, θ, was calculated from 2D RSMs in the (Q_x^{111}, Q_y^{111}) reciprocal space plane (Figure 6.2a).

Numerical values of thicknesses separating all three pairs of opposing side-facets and the angles between neighboring side facets are listed in Table 1. The fluctuations in the total diameters averaged for the three NWs with respect to the nominal dimensions are calculated to be 6 ± 3 nm and couple of nanometers with respect to one another along all opposing side facets. Additional information about the NW tilt can be extracted from

RSMs in the (Q_x^{111}, Q_y^{111}) plane. From the separation between the silicon crystal truncation rod (CTR) and the NW Bragg peak in Q_x^{111} and Q_y^{111}, the angular tilt of the NW with respect to the substrate normal can be determined with high precision that cannot be detected by SEM, see Table 1.

Table 6.1: Numerical values of thicknesses separating all three pairs of opposing side facets and angular orientation of neighboring side facets indicated by colored dotted lines and indicated in white in Figure 6.2d, respectively. In addition, the NW tilt with respect to the normal of the Si substrate, θ, was calculated from 2D RSMs in the (Q_x^{111}, Q_y^{111}) reciprocal space plane (Figure 6.2c).

	NW 1	NW 2	NW 3
Facets 1 (Orange)	152 ± 4 nm	147 ± 4 nm	147 ± 2 nm
Facets 2 (Red)	148 ± 1 nm	145 ± 1 nm	148 ± 5 nm
Facets 3 (Green)	144 ± 3 nm	143 ± 3 nm	142 ± 5 nm
$180^o - \alpha$	121	121	121
$180^o - \beta$	121	120	122
$180^o - \gamma$	118	119	117
Tilt along $[2\bar{2}0]$	-0.02197	0.01012	0.01255
Tilt along $[2\bar{2}0]$	0.01906	0.01575	0.00597
θ (^{o})	0.87	0.56	0.42

The slight variations in the NWs diameters with respect to the nominal value and the small NW tilt of less than 1 degree with respect to the normal of the substrate surface reflect the good growth conditions of the NWs.

Following the corresponding nXRD experiment, the CL intensities of NW1-NW3 were collected (Figure 6.3a) using a Gatan MonoCL4 system fitted to a Zeiss Ultra55 field-emission SEM. Measurements were carried out at an acceleration voltage of 5 kV with a beam current of about 600 pA. The sample was mounted on the edge of a 45° holder to access the line of as-grown NWs. The luminescence is collected by a parabolic mirror and directed to the spectrometer, where a 600 lines/mm grating blazed at 800 nm is used to disperse the light. Spectrally-resolved linescans of the CL emission were collected by stepping the electron beam along the axis of the NW and recording the emitted spectrum at every point using a charge-coupled device detector. The intensity distribution of the CL is inhomogeneous along the growth axes of all three NWs, but notably, the highest luminescence intensity is obtained for the mid-section of the NWs, which roughly corresponds to the position where the RSMs were recorded. This observation hints at a correlation of the CL

emission and the variation in crystal structure along the growth axes of the investigated NWs. Following this assumption, only a certain crystal phase would be responsible for the highest CL emission. Based on the results of the nXRD experiment, it is difficult to distinguish whether the highest CL intensity originates from ZB or the M phase (Figure 6.2b).

To answer this question, an additional nXRD experiment was carried out after the CL measurement. This experiment was performed at beamline ID01 of the ESRF [39] using a coherent nano x-ray beam with energy of 8 keV ($\lambda = 1.55$ Å). The beam was focused down to 200 nm x 400 nm (ver x hor) in size using a Fresnel zone plate. The same recipe, used in the previous nXRD experiment, was followed in order to locate the NWs by X-rays. In order to correlate the CL emission with the NW crystal structure, we mapped the spatial distribution of ZB, WZ and the M phase, along the growth axes of NW1-NW3. The technique used was SXDM which is a 2D quick and continuous mapping technique that provides nanometer resolution of a specimen at a given position in reciprocal space. The resulting real space maps are made by translating the sample and simultaneously recording scattering images at every point along a rocking curve. However, in this experiment, SXDM was performed at the Bragg angle of the ZB reflection. This only affects the collected intensity from each polytype but not the spatial distribution. The corresponding phases were monitored by measuring the 111 Bragg reflection. This means we are not able to distinguish between ZB and its twin as they overlap at the same position in Q_z^{111}. Due to the different lattice spacing of the 111 planes of the mentioned ZB, WZ and the M phase, their Bragg conditions are fulfilled at different angles appearing well separated in the 2D detector frames. Defining integrating boxes around each peak, we were able to map the intensities of the crystal phases along the NWs growth axes. The phase compositions of NW1-NW3 are demonstrated in Figure 6.3 and named accordingly i.e. the ZB, M and WZ spatial distribution within the NWs are displayed in Figures 6.3b, 6.3c and 6.3d, respectively. From the first look, the CL intensities correlate mostly with the M phase. To confirm this, first, the fraction of each polytype along the NW growth axis was calculated. This was done by dividing the integrating the intensity of each polytype inside the dotted yellow curves in Figures 6.2b-d, which represents the expected NW position, onto the sum of all. Second, the CL intensity was normalized and plotted with the polytype fractions in Figure 6.3e i.e. the CL and M phase data points are colored in black and red, respectively. In all three NWs, the peaks of normalized CL and the M phase fraction share almost the same spatial position along the NWs growth axes. Numerically, the M phase below the mid-sections of NW1, NW2 and NW3, show enhanced CL intensity up to a factor of $\approx$ 40, 20 and 80, respectively, compared to WZ and ZB.
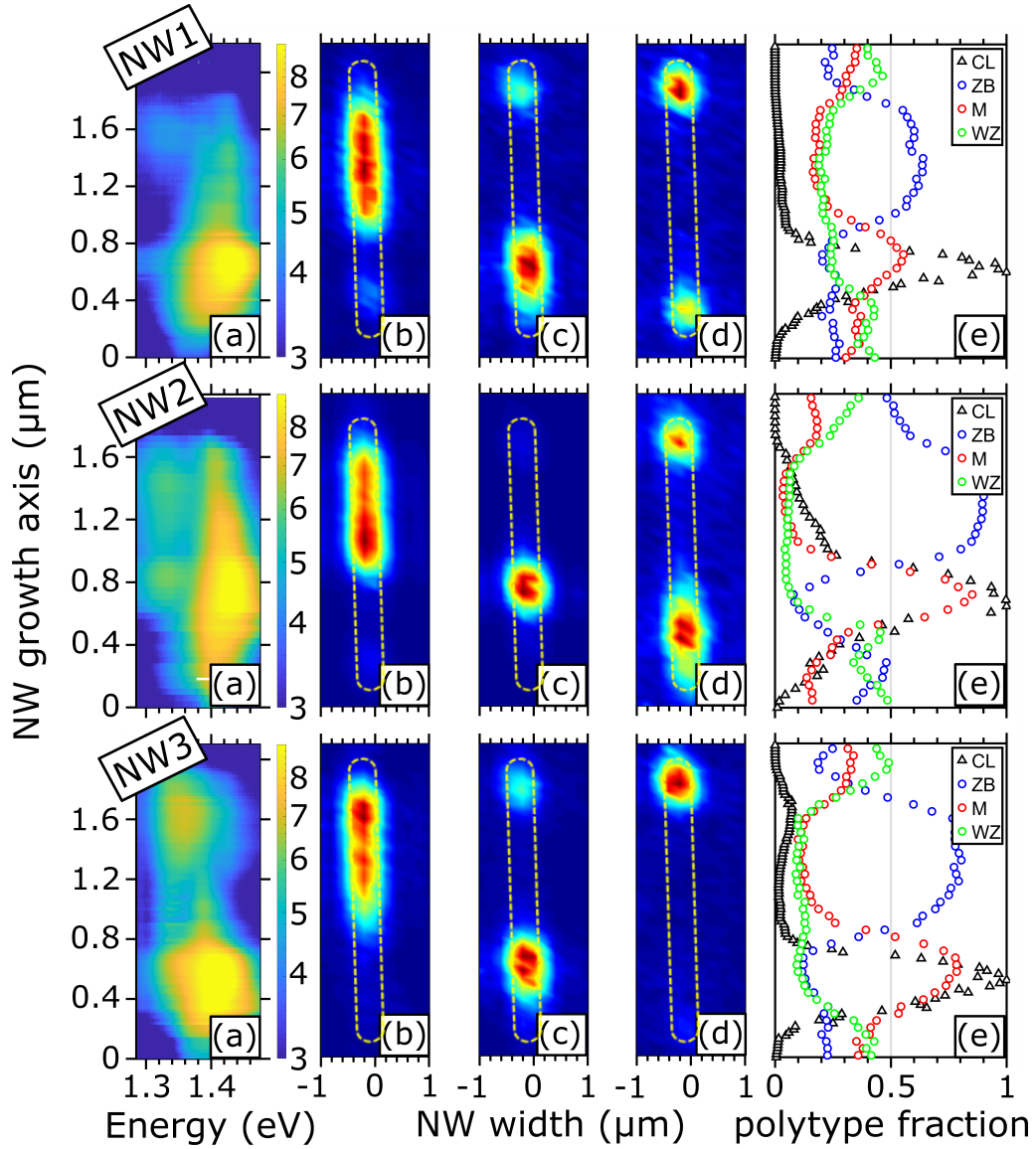
Figure 6.3: CL and crystal structure of three NWs. (a) CL intensity along the growth axes of the three investigated NWs. Panels (b), (c) and (d) ZB, M phase and WZ distribution along the NWs growth axes. (e) Integrated then normalized intensity of the CL 2D map (black) and the fractions of WZ (green), M phase (red) and ZB (blue), respectively. The yellow dotted curves in (b), (c) and (d) represent the NW shape.

Second, coherently displayed in all three well separated NWs, the NW growth is initiated always with WZ, followed by the M phase, then a long segment of ZB and its twin, which

71

cannot be distinguished from 111 measurements and finally a combination of the M phase and WZ at the NW top section where low crystallinity and many stalking faults are expected. The growth is in agreement with former observations of similar NW systems [99]. The three NWs, being well separated (see Figure 6.1), show very consistent growth in terms of crystal phase distribution.

Figure 6.4a shows a transmission electron micrograph of a single core-shell NW grown on a different substrate under same conditions as the investigated NWs. The image is acquired under dark-field conditions using the cubic (220) diffraction spot. The left side corresponds to the bottom part of the NW and on the right side the faceted top is visible. At the bottom of the NW, axial contrast features with high frequency are detected. These features are attributed to the presence of stacking faults and thin slabs of different crystal phases. In contrast, the upper part of the NW does not show clear axial contrast. Only the top of the NW shows deviations from a single crystal phase (like the bottom) due to the droplet consumption procedure. Figures 6.4bd show selective area electron diffraction measurements that were acquired to identify the different crystal phases. For the measurement at the bottom shown in Figure 6.4b, diffraction from twinned cubic zincblende structure (blue and green notations), hexagonal wurtzite structure (red notations), and streaks along [111] are detected, that are attributed to stacking faults or thin slabs. Figure 6.4c shows the measurement at the central part, exhibiting diffraction from twinned zincblende segments (blue and green). Figure 6.4d shows the measurement at the top part of the NW where only a single zincblende phase is detected (blue). Interestingly, the magnifcations of the electron diffraction images indicate that secondary spots above and below the (111) and (220) zincblende spots exist in Figure 6.4c and 6.4d. Their position exactly above and below the main peaks corresponding to the radial direction indicate a coherent, elastically strained shell. Furthermore, no sufficient indications for plastic relaxation by dislocations are indicated in the micrograph, as the contrast along the NW width corresponds to thickness fringes due to the hexagonal shape of the NW. These results imply that dislocations are not causing the low luminescence intensity of the sample grown with co-deposition and therefore, we propose that a high density of point defects might be the origin for the low luminescence intensity. However, this result is only based on few TEM measurements and more work needs to be done to distinguish the nature of the defects.
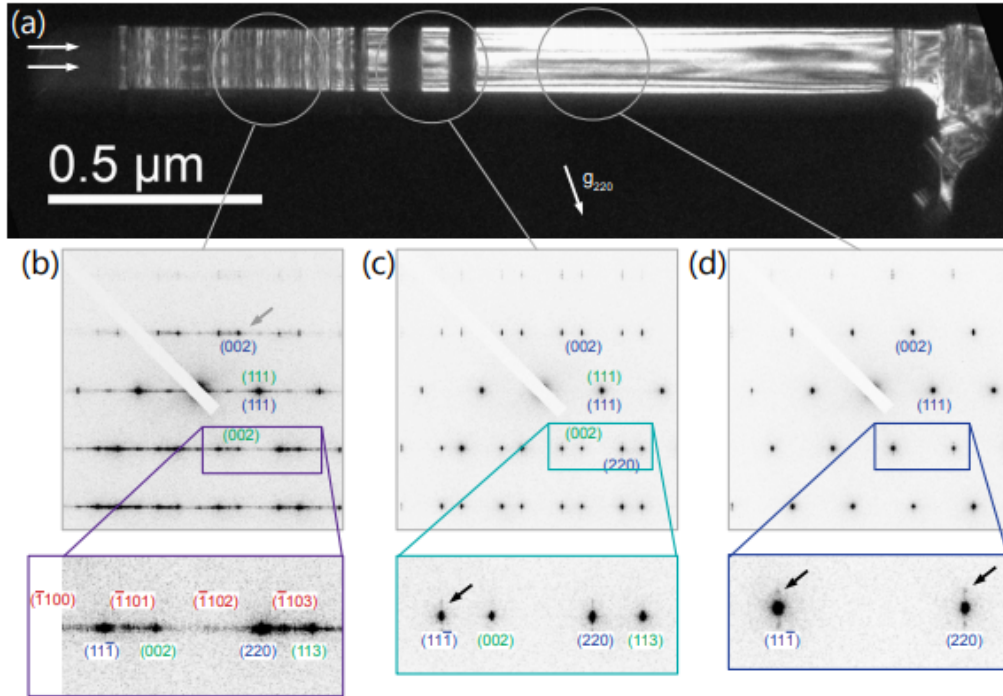
Figure 6.4: (a) Transmission electron micrograph taken in dark-field mode on a core-shell NW. The three panels in (b), (c), and (d) show electron diffraction measurements at different positions of the NW. Here, the labels indicate the respective lattice vector in reciprocal space and the arrows indicate diffraction spots suggesting a coherently strained shell.

6.4 First signs of beam damage

Apart from the GaAs/(In, Ga)As/GaAs/AlAs/GaAs core-shell NW system that was investigated for optical and structural correlation, individual GaAs/(In, Ga)As/GaAs core-shell NWs grown onto an other patterned Si 111 substrate were measured by in-plane and out-of-plane nXRD. These measurements were carried out by recording RSMs at different positions along the growth axis of each NW which in turn demand long acquisition time. The cross-sections of both NW systems are animated in Figure 6.5a and 6.5e. Next to each animation, the CL emission along the growth axis of three distinct NWs from the corresponding NW system is displayed. The exposure time of each NW is mentioned on top of each subplot. The first NW system was exposed by the nano X-ray beam for less than 2 hours (see Figure 6.5b-d) whereas the second was exposed for more than 3 hours in total (Figure 6.5f-h). On the one hand, NWs measured for less than 2 hours still show

pronounced CL emission. For example, NWb which was not exposed by X-rays is approximately 1 µm in length and shows a rather homogeneous CL emission along it growth axis. On the other hand, NWs that were heavily exposed by X-rays have completely diminished CL. For example, NWc which was exposed for a duration of 6 h shows no CL.

The optical damage induced by X-ray exposure was accompanied by burn-like features on the substrate, which represent the trace along the direction of the incident X-ray beam, as well as morphological changes of the exposed NWs such as roughness of the NW to air interface and increase of the NW diameter and length caused by C deposition. The morphological and optical changes caused by long exposure at the same position along the NW growth axis will be discussed and explained in details in Chapter 7.
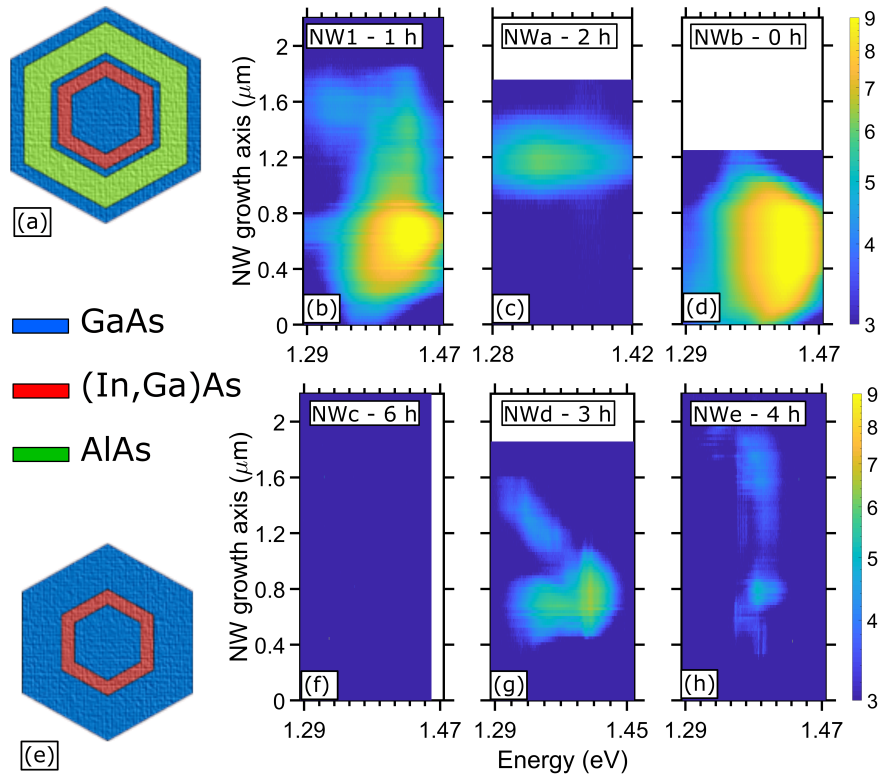

Figure 6.5: (a) and (e) plan-view animations of GaAs/(In, Ga)As/GaAs/AlAs/GaAs and GaAs/(In, Ga)As/GaAs NWs, respectively. (b-d) CL 2D maps of three NWs from the NW system in (a) after exposure. (f-h) CL 2D maps of three NWs from the NW system in (e) after exposure. The exposure time of each NW is mentioned at the top of each subplot.

6.5 Summary

In summary, the structural composition and dimensions of three CL measured NWs were inspected in their as-grown geometry using nXRD. Two nXRD experiments were carried out before and after the CL measurements. The first one revealed the almost perfect hexagonal geometry and very small tilting of the NWs with respect to the substrate normal in addition to only slight variations in the thicknesses of core and shells compared to the nominal dimensions. The second experiment revealed the structural composition and distribution along the growth axes of the three NWs which is in agreement with the theoretical growth calculations for GaAs NWs. The most interesting and novel finding of this work was unfolding the enhanced CL emission of the mixed phase within the NWs up to a factor of 80 which can be exploited to enhance the optical properties of NW based devices.

Chapter 7

Beam damage of single semiconductor nanowires during X-ray nano beam diffraction experiment

PS: This chapter should be heavily updated as, very recently after submission, the same experiment was replicated but under He atmosphere. A paper combining results of the two experiments, under ambient conditions and He atmosphere, will be published elsewhere in the near future.

Nanoprobe XRD using focused synchrotron radiation is a powerful technique to study the structural properties of individual semiconductor NWs. However, when focusing the highly intense radiation down to a sub-micron in size, a high radiation dose is deposited into a small sample volume, which may cause radiation damage for measurements with long exposure time. Here, we report on a nXRD experiment carried out on semiconductor NWs, which were previously considered to be resistant against radiation damage. The experiment has been performed under ambient conditions at the microfocus station of the P08 beamline at the 3rd generation source PETRA III. Using an incident X-ray beam with an energy of 9 keV and photon flux of 10^{10} s^{-1}, individual NWs were monitored continuously over a time interval of up to 5 hours by recording reciprocal space maps of the 111 Bragg reflection at the same spatial position. For an exposure time of about 1h, we observe a reduction in the NW integrated Bragg intensity accompanied by minor axial lattice expansion and small tilts of the NW axis with respect to the substrate normal. NWs exposed for more than 2 hours show an increase of lattice expansion and after 3 and more

hours of exposure, we can observe NW melting. SEM images taken after nXRD display the formation of an amorphous shell around the NW, which is maximum at the position of exposure. In addition, emission properties of a core-shell quantum well embedded in the same investigated NWs are studied by CL spectroscopy before and after nXRD exposure. For the 1h-exposed NWs, the CL intensity was locally quenched at the position of X-ray exposure. NWs exposed for 2h and more did not show any CL. Our findings are explained by the huge energy impact into a small NW volume due to the massive generation of electrons and subsequent electron-phonon interactions. Our results have a significant impact on future experiments to be performed at nanobeam stations of 4th generation synchrotron facilities.

7.1 Introduction

The optical emission of core-shell NW systems [100] relies on two major aspects. First, specific structural parameters such as the thickness and composition of the shell material can be used to tune the QW emission [15, 33, 34, 84]. Second, NWs often exhibit polytypism [29, 53], i.e. the occurrence of both the WZ and ZB crystal structures, or even a mixture of the two phases in the form of alternating layers. The WZ and ZB polytypes possess different structural [94] and electronic properties (e.g. band gaps) [1, 101]. Apart from transmission electron microscopy techniques such as high-angle annular dark-field imaging in scanning transmission electron microscopy [17], energy dispersive X-ray spectroscopy [18] and high-resolution transmission electron microscopy [30], the development of X-ray optics and third generation synchrotron radiation sources with high brightness nano-focused X-ray beams [39, 40] made it possible to probe the structural parameters, spatial alloy distribution, crystal phases and strain distribution of single core-shell NWs by means of XRD based methodologies. These include nano X-ray fluorescence [74], coherent Bragg ptychography [19] and coherent and non-coherent nXRD [73, 102]. For example, in a previous work [14], we have demonstrated that the thicknesses of the core and shells within individual core-shell NWs, as well as the strain distribution, can be accessed in the as-grown geometry by recording RSM of in-plane Bragg reflections. Furthermore, we were able to demonstrate the direct correlation between the optical properties and the crystal phase structure of individual as-grown GaAs/(In,Ga)As/GaAs core-multi-shell NWs by means of spatially-resolved CL and nXRD mapping for selected Bragg reflections, respectively [99]. However, during the acquisition of RSMs around Bragg reflections, the beam is fixed to the same position along the NW growth axis for an extended time. This measurement mode results in a high absorbed X-ray dose at the illuminated NW section.

Shi et al. 2012 have demonstrated radiation-induced bending of Si-on-insulator (SOI) NWs by means of coherent diffraction imaging i.e. the authors have observed a splitting of the Bragg reflections, which continuously evolves with increasing X-ray dose [103]. In a previous work done on planar SOI layers, the structural damage induced by the absorbed X-ray dose was described to induce permanent structural damage to the crystal lattice [104]. In this work, we will extend on these observations and illustrate in detail the impact of the exposure to high X-ray doses on the structure, morphology and optical emission of individual NWs. The structural changes, e.g. tilting and axial lattice variation, were monitored by continuous recording of RSMs of the 111 Bragg reflection as a function of exposure time and absorbed X-ray dose. Using SEM imaging before and after X-ray exposure, we observe severe morphological changes, while hyperspectral CL mapping in the same SEM allows us to assess the impact of the X-ray exposure on the optical emission.

7.2 Sample and experimental details

The investigated NWs were grown by molecular beam epitaxy on a patterned Si(111) substrate using the Ga-assisted vapor-liquid-solid mechanism [33, 34]. The as-grown NWs are about 2.5 µm in length and 150 nm in diameter and contain radial heterostructures of GaAs/(In,Ga)As/GaAs with 20% nominal In concentration and 10 nm thickness of the (In,Ga)As QW shell. The NWs were grown along a straight line on the substrate with a spacing of 10 µm between two neighboring NWs [14]. This makes it possible to access the same individual NWs both in nXRD and SEM/CL measurements. More details about the growth process and sample geometry can be found elsewhere [33, 34].

The nXRD experiment was performed at the beamline P08 of PETRA III [86] using a photon energy of 9 keV. The photon flux integrated over the cross-section of the beam was 10^{10} s^{-1}, while the vertical and horizontal full width at half maxima of the beam were 0.6 µm and 1.8 µm, respectively. In order to study the impact of X-ray exposure on the structural properties, 12 NWs were systematically exposed for durations between 1h and 5h. To trace the structural changes, RSMs of the 111 Bragg reflection were continuously recorded at the same position along the NW growth axis during the exposure. The time needed to record each RSM was 8 minutes. Methods used to translate from real space to reciprocal space and how to construct a 3D RSM of the measured Bragg reflection have already been presented in previous work [14, 47].

For all investigated NWs, SEM images and CL hyperspectral line-scans were recorded before and after X-ray exposure using a Zeiss Ultra55 microscope equipped with a field-emission cathode. The microscope was operated at an acceleration voltage of 5 kV with a beam current of 1.3 nA. For low-temperature CL measurements at 15 K, the SEM is fitted with a Gatan MonoCL4 system and He-cooled stage. The light is collected by a parabolic mirror and passed through an entrance slit of 0.5 mm width into a monochromator equipped with a 600 lines/mm grating blazed at 800 nm and detected on a Si-CCD. To measure the as-grown NWs, the sample is cleaved close to the line of NWs and mounted at an angle of 45°, which is accounted for when plotting the CL versus position along the NW axis. Hyperspectral line-scans are recorded by scanning the beam along the axis of the NW and recording a spectrum for 1 s at every dwell point. The python package hyperspy is used to process the CL data [105].

7.3 Experimental results

The impact of X-ray exposure on the NW structure will be exemplified for two individual NWs that will be referred to as NW1 and NW2 in the following. NW1 was exposed for 1 hour, whereas NW2 was exposed for a total of 4 hours. Before exposure, the two NWs were about 150 nm in diameter and about 2.5 µm in length with a hexagonal cross-section and well-defined side facets (see Figure 7.1a,e). After exposure, the diameter of NW1 increased by 50 nm which, if assumed symmetric, is 25 nm on the wall of each opposing side facet, and its length increased by 200 nm (see Figure 7.1b).This causes the well-defined side facets to disappear. We attribute this increase in the diameter and length of the NW to C deposition. As the sample was exposed to air, the presence of hydrocarbon molecules on the surface is inevitable. These molecules can be cracked by the impinging energetic X-ray beam, leading to C deposition on the surface of the NW and to a certain degree also on the substrate. This is expected to be enhanced by the fact that the nXRD experiment was carried out at ambient conditions. Additionally, the hydrocarbon molecules are polar and can be attracted to the exposed area by charging, leading to further C deposition along the NW circumference [106, 107].

The aforementioned changes were accompanied by a local degradation in the optical properties of the NW. This degradation was visualized by spectrally-resolved CL line-scans of the emission from the (In,Ga)As QW acquired before (Figure 7.1c) and after (Figure 7.1d) exposure. Before exposure, the NW QW showed a homogeneous distribution of the luminescence along its growth axis. The emission is centered at about 1.25 eV and shows

only a minor blueshift between the bottom and center of the NW. The tip of the NW does not emit due to a reduced crystal quality and the absence of the shell QW in this segment that is formed by axial elongation during shell growth, which also leads to a change in faceting in Figures 7.1a and 7.1e [99]. After exposure, a significant degradation of the CL emission is visible in the segment between 1.2 µm and 1.6 µm along the NW axis (Figure 7.1d), which is assumed to be the position of the nanobeam. Following the estimation for GaN NWs in Lähnemann et al. 2016, and taking 1×10^5 cm^{-1} as an upper bound for the absorption coefficient of amorphous C at a photon energy of 1.25 eV [108,109], 25 nm of C are approximated to block a maximum of about 20% of the CL emission. This indicates that light absorption in the deposited C layer is not the dominating factor in degrading the optical properties of the NW. On the one hand, the CL intensity is highly sensitive to the presence of non-radiative point defects that could potentially be introduced in the crystal lattice due to X-ray exposure, i.e. in the central segment for NW1. The introduction of such defects would lead to a significant enhancement of non-radiative carrier relaxation at the expense of the QW emission. On the other hand, the heating of the NW during the prolonged X-ray exposure could at some point lead to an interdiffusion of Ga and In atoms that degrades the previously well-defined QW layer. The emission energy of such a wider (In,Ga)As layer with reduced In content would shift to higher energies compared with the QW emission. However, at the same time, the confinement of carriers in the QW would be lost. As the luminescence from semiconductor NWs is highly sensitive to non-radiative recombination at the NW surface [34,110]. For GaN NWs, it has been observed that this non-radiative channel can even be enhanced by the creation of additional surface states during C deposition on the surface [111], Therefore, such a structural change would also lead to a quenching of the QW emission intensity. The potential structural damage to the crystal lattice by the high X-ray dose will be further discussed below.

For NW2, more severe morphological changes are observed after exposure, concerning the outer surface, length and diameter of the NW (see Figure 7.1e,f). First, the NW-to-air interface lost its well defined facets, which again can be explained by C deposition. Second, the NW section indicated by a red dashed circle in Figure 7.1e vanishes and beneath it, a swelling-like feature becomes visible (Figure 7.1f). As we discuss below, the top section of the NW, which is approximately 500 nm in length, has melted down and formed the swelling that we observe in Figure 7.1f. As a consequence, the NW diameter is increased to approximately 210 nm at the bottom and up to 480 nm at the swollen area. The melting of the NW top section after exposure brings us to the conclusion that the NW section named P in Figure 7.1e was illuminated by the peak of the Gaussian shaped X-ray beam, whereas the NW section circled in pink and named T was illuminated by its tail. The

morphological damage of NW2 was accompanied by a complete loss of its CL emission along the whole length of the NW.
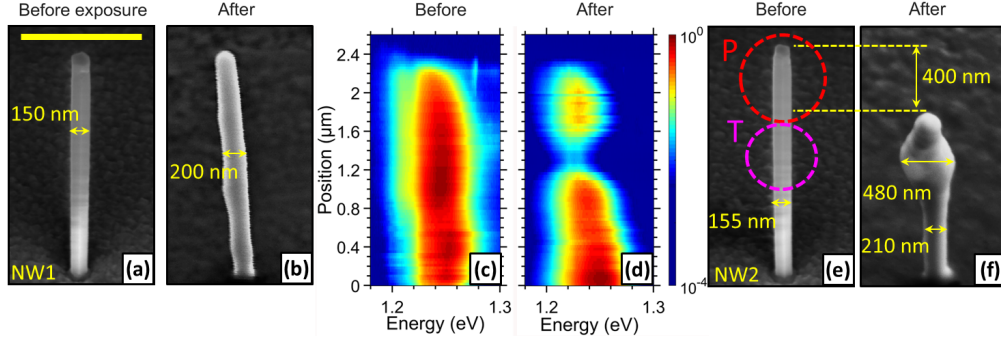

Figure 7.1: (a) and (b) SEM micrographs of NW1 before and after exposure, respectively. (c) and (d) Normalized low-temperature hyperspectral CL line-scans along the NW growth axis before and after exposure (color-coded logarithmic intensity scale) for NW1. Note that the emission intensity depends sensitively on the positioning of the NW with respect to the focal point of the parabolic mirror so that the absolute intensities of the two line-scans cannot be compared directly. (e) and (f) SEM micrographs of NW2 before and after exposure. Red and pink dashed circles, named P and T, indicate NW sections illuminated by the peak and tail of the Gaussian beam. The scale bar in (a) corresponds to 1 μm and applies to all SEM images.

To understand the morphological damage and optical degradation, we continuously recorded RSMs of the 111 Bragg reflection of the NW during the exposure experiment. This will be discussed in detail in the following. Typical (Q_Z^{111}, Q_Y^{111}) and (Q_Y^{111}, Q_X^{111}) 2D projections of the 3D 111 Bragg reflection of NW2 are presented in Figure 7.2a-e and Figure 7.2f-j, respectively. Here, Q_Z^{111} is defined along the scattering direction of the 111 Bragg reflection in reciprocal space and is sensitive to polytypism and variation in the axial c-lattice parameter. The reciprocal space vectors Q_X^{111} and Q_Y^{111} are defined along the NW $[22\bar{4}]$ and $[2\bar{2}0]$ directions, respectively, and are sensitive to the NW thickness and tilt. The RSMs in Figure 7.2a and 7.2f have been recorded only 3.6 min after the start of the exposure. The Si 111 Bragg reflection in the upper part of the RSM, was considered as a reference to calculate the variation in the axial lattice spacing of the NW and therefore was placed at the unstrained position of $Q_Z^{111} = 20.038$ nm^{-1}. Apart from Si, the pseudomorphic ZB ($Q_Z^{111} \approx 19.22$ nm^{-1}) and WZ ($Q_Z^{111} \approx 19.06$ nm^{-1}) Bragg reflections are visible. The nominal positions for unstrained GaAs of both polytypes, $Q_Z^{111} \approx 19.25$ nm^{-1} for ZB and $Q_Z^{111} \approx 19.09$ nm^{-1} for WZ, are indicated by dashed Debye-Scherrer rings in all (Q_Z^{111}, Q_Y^{111}) RSMs. Both reflections are slightly shifted from the unstrained positions due

81

to the lattice mismatch between GaAs and the (In,Ga)As shell, which contains a nominal indium content of 20%. From the appearance of thickness oscillations of the ZB reflection, it is evident that the beam is well aligned on the NW. After 48 min of X-ray exposure, the ZB reflection elongates towards smaller Q_Z^{111} values and shifts along Q_Y^{111} giving evidence for lattice expansion and tilt. The WZ peak also moves towards lower Q_Z^{111} values. After 92 min, the main peak splits into 2 sub-peaks. Considering Figure 7.1e, the sub-peaks circled in pink and red resemble the NW sections assumed to be illuminated by the tail and peak of the Gaussian nano beam, respectively. At the end of the exposure, the sub-peak originating from section P vanishes, which is explained by the melting of this NW section.

The red and black small circles in the (Q_Y^{111}, Q_X^{111}) RSMs correspond to the Si crystal truncation rod (CTR) and the NW tilt at the beginning of exposure, respectively. The thickness oscillations present in Figure 7.2f and indicated by a green dashed rectangle correspond to a NW diameter of 154 nm $\pm$ 5 nm, which is in very good agreement with the SEM observation. After 48 min (Figure 7.2g), the thickness oscillations disappear, which may be explained by the amorphous C layer deposited on the outer NW circumference. After 92 min and 117 min of exposure, similar to the (Q_Z^{111}, Q_Y^{111}) maps, the Bragg peak divides into two sub-peaks. The first sub-peak, denoted by T, remains at the same Q_X^{111} and Q_Y^{111} positions showing no tilt, whereas the second sub-peak, named P, splits from the first and moves along the dashed arrow in Figure 7.2i. At the end of the exposure (after 240 min), P vanishes. The RSMs of NW1 are given in Appendix A and show a behavior similar to the RSMs of NW2 recorded during the first hour of exposure.

The mechanism of peak elongation results from the X-ray exposure, as the position along the NW where RSMs were taken, as well as the scanning range and acquisition time, were not modified during the measurements. As discussed below, the peak elongation and splitting effect originates from the absorbed X-ray dose, which causes thermal heating and results in lattice expansion of the NW in the pattern.
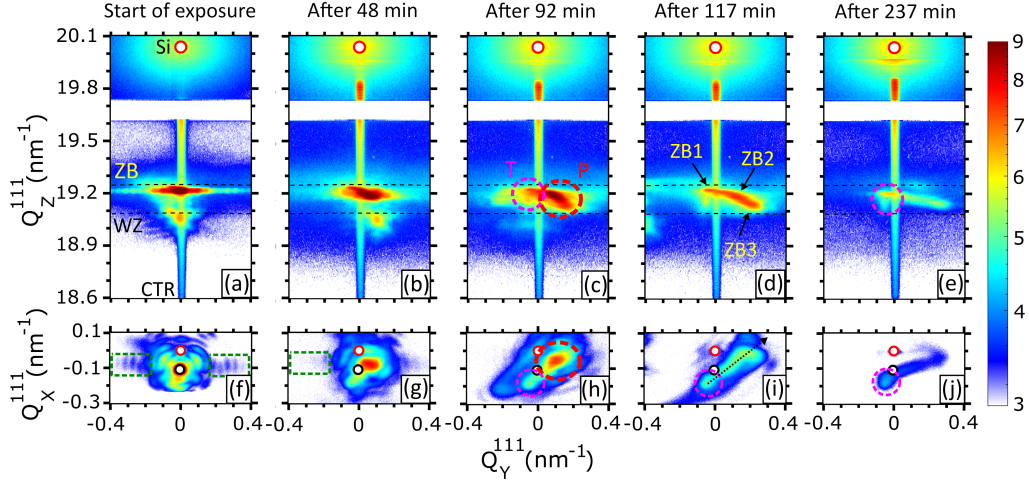
Figure 7.2: Panels Panels (a-e) 2D projections of the 111 Bragg reflection of NW2 in the (Q_Z^{111},Q_Y^{111}) reciprocal space plane. The two dashed curves in Q_Z^{111} represent the ZB (top) and WZ (bottom) Debye-Scherrer rings. The red and pink dotted circles named P and T are explained in Figure 7.1e and represent sub-Bragg peaks that originate from NW sections illuminated by the Peak and Tail of the Gaussian beam. The peaks named ZB1 ZB3 will be explained in relation with Figure 7.3d. Panels (f-j) 2D projections of the 111 Bragg reflection in the (Q_Y^{111},Q_X^{111}) reciprocal space plane. The time at which each RSM acquisition was started is mentioned at the top.

In order to quantify the NW tilt, the RSMs in the (Q_Y^{111},Q_X^{111}) plane were integrated along Q_Y^{111} and Q_X^{111} each at a time and the resulting integrated line-scans were fitted by multi-Gaussian functions. The angular tilts of the NW along Q_Y^{111} and Q_X^{111} are denoted by α_y and α_x, respectively. Following this procedure, we were able to trace the variation in α_y and α_x as a function of exposure time and thus the absorbed X-ray dose. The results are illustrated in Figures 7.3a and 7.3b. The calculation of the absorbed dose is explained in detail in Appendix B. At an exposure time of 48 min, it can be clearly seen that P and T tilt in opposite directions indicating a small bending. The heavily illuminated part, P, tilts by 0.1^o in α_y and 0.4^o in α_x with respect to the initial position, whereas the less illuminated part, T, tilts by -0.2^o in α_y and α_x by the end of exposure. The intensity decay of the 111 Bragg reflection is plotted in Figure 7.3c showing an exponential decay. This has been calculated by integrating the intensity distribution of the 3D Bragg reflection along all three reciprocal space vectors, Q_Z^{111}, Q_Y^{111} and Q_X^{111}. The Si CTR was excluded from the integration process. Finally, from the variation of the Bragg reflections in Q_Z^{111}, we were able to calculate the variation in the axial c-parameter, Δc (see Figure 7.3d). The Bragg reflection of the WZ polytype, which is formed in the upper part of the NW (see

83

Figure 7.4a) when the As-droplet is consumed at the end of the core growth [111, 112], undergoes rapid thermal lattice expansion before disappearing after 92 min of exposure. Based on SEM images and the tilt calculations, this evolution can be caused by tilting away from the Bragg condition followed by melting. The main ZB Bragg reflection, visible at the beginning of exposure, splits into 2 sub-peaks after 48 min and then into 3 sub-peaks after 92 min demonstrating a thermal expansion gradient of about 0.5%. Since the three sub-peaks originate from the main ZB reflection, they are referred to as ZB1, ZB2 and ZB3 in Figure 7.2d. As it can be seen in Figure 7.3d, ZB3 undergoes the highest lattice expansion compared to the position of the original ZB reflection at the beginning of exposure. This reflects the impact of the peak and tail exposures of the primary beam on the ZB polytype as a function of its spatial position along the NW growth axis. Therefore, ZB3 is assumed to be the region located directly below the WZ segment and beneath it is ZB2 and then ZB1 as sketched in Figure 7.4a.
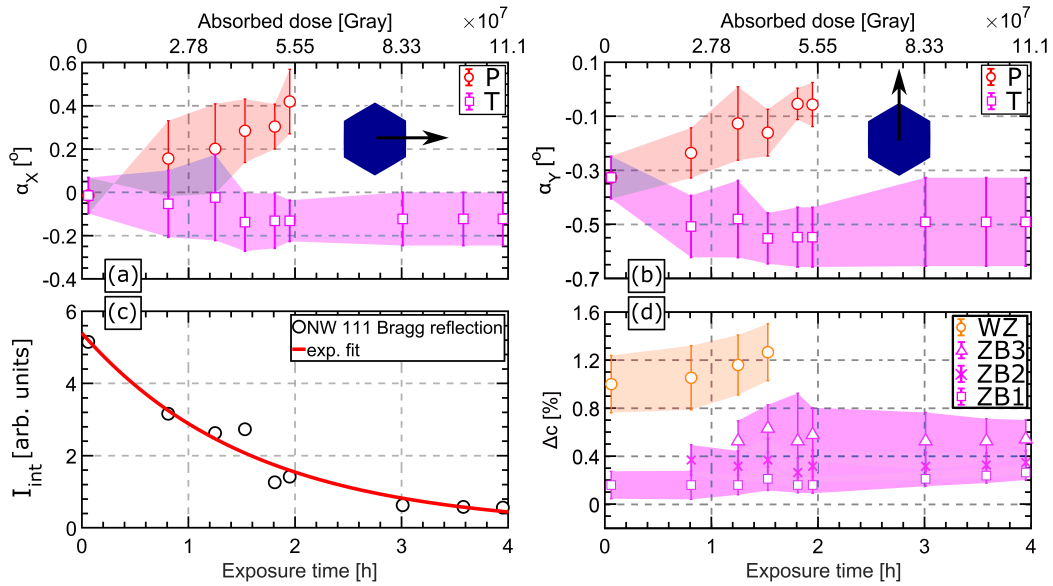
Figure 7.3: (a) and (b) tilt of NW2 along Q_X^{111} and Q_Y^{111}, respectively. The blue hexagon represents the NW cross-section and the black arrow represents the tilt direction. Data points colored in red correspond to section P whereas the ones colored in pink correspond to section T of the NW. (c) The data points demonstrate the intensity decay of the 111 Bragg reflection of the NW. The red curve is an exponential fit. Error bars are within the size of the dots. (d) Variation in the axial c-parameter within NW2. The orange data points correspond to the WZ reflection. The three ZB sub-peaks, colored in pink, were named ZB1 ZB3 as indicated in Figure 7.2d.

To explain the melting of the upper part of the NW, we made an estimate of the temperature change ΔT by attributing the axial lattice expansion (data in Figure 7.3d) to thermal heating using equation 7.1, where $C = 6.4 \times 10^{-6}/K$ is the bulk thermal expansion coefficient of GaAs:

$$\Delta T = \frac{\Delta Q_z}{Q_z \times C} \tag{7.1}$$

The results are displayed in Figure 7.4. On the one hand, the WZ polytype reaches a temperature of approximately 500 °C before the WZ signal disappears. On the other hand, ZB3 reaches temperatures higher than 600 °C. The rapid increase in the temperatures of the WZ polytype and ZB3, compared to ZB1 and ZB2, can be attributed to both peaks being located at NW section P (Figures 7.1e and 7.4a), which is illuminated by the peak of the Gaussian beam. The congruent decomposition of GaAs starts at 625 °C [113], but As losses can already occur at lower temperatures [114]. In consequence, this heating can explain the melting of the top part of the NW observed in Figure 7.1f.
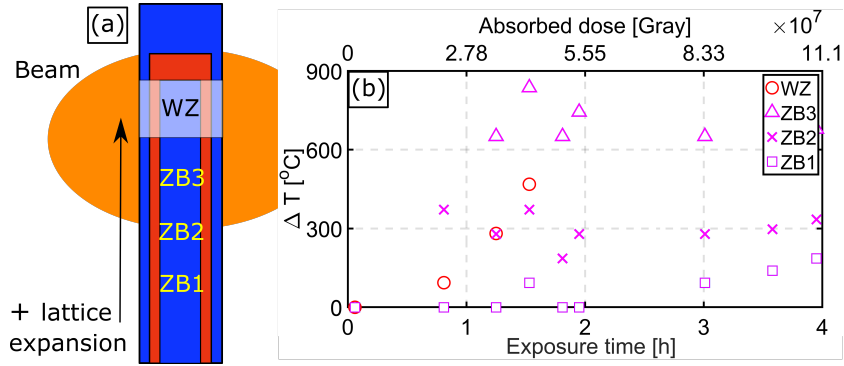
Figure 7.4: (a) Side view sketch showing the core-shell-shell configuration of a single NW. These NWs typically grow in the ZB crystal phase, whereas the WZ polytype is present in the upper part of the NW, just below the top section formed by axial elongation during shell growth. (b) Change in lattice temperature with exposure time (or absorbed radiation dose) extracted from the positions of the WZ and ZB Bragg reflections.

In total, 12 NWs have been systematically exposed for different time intervals. Melting was observed for NW2 and one other NW that was exposed for 3 hours. Due to C deposition, all other NWs showed an increase in height and diameter similar to NW1. The radial C deposition was inhomogeneous along the growth axes of several NWs, i.e. the increase in the diameter was estimated by SEM to range between 60 nm and 150 nm. Two NWs showed major tilting of 18o and 23° whereas all other NWs tilted only up to

3o. All the NWs that were exposed for at least 2 hours showed a complete quenching of the CL emission, except for one NW for which only the tip seems to have been exposed. Furthermore, local CL degradation was also noticed for NWs that were exposed for only one hour. From nXRD, minor tilting and lattice expansion were observed during the 1st hour of exposure (2.8×10^7 Gy). During the 2nd hour (5.5×10^7 Gy), the crystal lattice undergoes a pronounced lattice expansion gradient. During the 3rd hour (8.3×10^7 Gy), melting can occur. This observation is consistent for the majority of the exposed NWs. However, as the alignment of the beam with respect to the NW may differ between individual NWs, the actual dose a NW gets in a certain time might vary, which explains wire-to-wire differences concerning the speed at which the intensity decay or crystal deformation progress.

7.4 Discussion

Due to the high flux of the focused X-ray beam, combined with the confined dimensions in the NW geometry, radiation damage can occur for a semiconductor like GaAs, which from planar structures is known as a radiation hard material suitable for X-ray detectors [115, 116]. The damage we observe can be primarily explained by sample heating due to the continuous excitation by the high-fluence X-ray beam. The X-ray beam interacts with the NW material exciting photoelectrons from core atomic shells. The excited core states relax via X-ray fluorescence and the emission of Auger electrons. The photoelectrons, in turn, undergo multiple elastic and inelastic scattering events, which transfer energy to the lattice (phonons) and lead to the excitation of additional free electrons, respectively. Thus, the inelastic scattering of a single X-ray photon leads to a whole cascade of fast secondary electrons in the crystal [117]. Once the electrons are slowed down to energies below 10 eV, they can excite valence electrons to the conduction band, but again the excess energy is transferred to phonons, when the electrons and holes thermalize to the band edge. During the prolonged exposition at high X-ray flux, the excitation of phonons leads to the heating and thus expansion of the lattice evidenced in the evolution of the Bragg reflections during X-ray exposure. Note that in contrast to planar layers, the heat dissipation to the substrate is limited in these one-dimensional nanostructures. Temperature gradients away from the area of peak exposure can explain both the widening of the main ZB reflection (ZB1ZB3) and the stronger heating effect on the WZ Bragg reflection and on the sub-peak ZB3, which is assumed to correspond to the region below the WZ segment (Figures 7.3d and 7.4a). At the same time, the heating could cause interdiffusion of In and Ga species around the (In,Ga)As shell [Iikawa et al. 1988], which would reduce the confinement of carriers in the QW and, due to nonradiative recombination at the NW

surface, quench the luminescence emission. When the heating of the lattice continues, As is evaporated from the lattice [114], which then leads to a melting of the crystal. The melted material runs down the side of the NW to form the swelling we observe for NW2. During this stage, we completely loose the Bragg reflection from this part of the NW (WZ segment and ZB3).

At the same time, the inelastic scattering during the electron cascade could result in a phase transition known as nonthermal melting [118]. This process has been observed as a consequence of the high dose of fs pulses supplied by free electron lasers at 4th generation light sources [118–120]. However, for III-V semiconductors, Medvedev et al. 2019 predicted that the nonthermal melting threshold is higher than the one for thermal melting $(1.2 \text{ eV/atom} \approx 4.1 \times 10^6 \text{ Gy})$. These doses are one order of magnitude below the dose for which we observed melting of NW2, but correspond to the short-pulse, high-fluence excitation conditions at a free electron laser. In line with these theoretical results, we expect that thermal melting dominates the damage process in our samples.

The C deposition observed during X-ray exposure under ambient conditions can be explained by the interaction between the hydrocarbons on the surface of the substrate and the energetic X-ray beam. In the present case, C diffusion into the lattice cannot be excluded, but due to its smaller ionic radius compared to Ga and As, it is expected to contract the lattice [121–123] and not to expand it. On the one hand, C is a good conductor of heat, i.e. the thermal conductivity coefficient is 1.7 W/mK, compared to that of GaAs, which is only 0.2 W/mK. Therefore, the formation of a C shell would improve the heat transport along the NW, which would reduce the effect of heating at the illuminated region. On the other hand, the formation of a C shell around the NW can contribute to the degradation of the CL emission when the integrity of the QW is compromised by the heating of the crystal. As explained above, optical absorption in the C layer plays only a minor role in the observed quenching of the CL emission, as strong luminescence was still visible along most of the length of NW1 for a 25 nm thick C shell. Nevertheless, C deposition could be reduced by (1) keeping the NWs under inert gas atmosphere and (2) surface cleaning to remove hydrocarbons present on the surface of the sample.

7.5 Summary

Overall, we have demonstrated that continuous illumination of NWs by an X-ray beam focused to sub-micron spot size at an unchanged beam position can induce profound changes

in structure and morphology of the NWs, with a severe impact on the emission properties of embedded core-shell QWs as evidenced by CL measurements. As demonstrated, the exposition of NWs under ambient conditions for 1h, corresponding to a radiation dose of 2.8×10^7 Gy, results in the deposition of an amorphous C shell onto the NW side facets with a mean thickness of 25 nm. At the same time, a local quenching of the CL emission is accompanied by major structural changes such as tilting and lattice expansion. NWs exposed for 2h, corresponding to a dose of 5.5×10^7 Gy, show no more CL emission, while the lattice expansion continues. When the exposure time exceeds 3h, a melting of the NWs is possible. We attribute the structural changes to X-ray induced excitation of electrons and subsequent electronphonon interactions, which result in sample heating and lattice deformation. The CL quenching is explained by either the formation of point defects or the possible In and Ga interdiffusion around the QW shell. The observed C deposition plays only a minor role in the quenching of the CL emission.

The presented results have a significant impact on experiments to be performed in future nano-beam stations at 3rd and 4th generation synchrotron facilities. In general, it would be desirable to avoid permanent exposure, for example by choppers or fast shutters or using the single bunch mode with time delays in the nanosecond range. This reduction of the X-ray dose during exposure should be accompanied by sample cooling to further reduce the heat load.

Chapter 8

Conclusions

In this work, conventional diffraction techniques using a nano-focused X-ray beam have been used to determine the structural parameters of individual GaAs/(In,Ga)As/GaAs based core-shell NWs in their as-grown geometry. In particular, we extract information about the spatial indium distribution within the (In,Ga)As shell, the diameter and thicknesses of the core and shells, the strain acting at each side facet, and the polytype distribution along the growth axes of single NWs.

- We have demonstrated a combination of high resolution XRD done on NW ensembles and nXRF performed on individual NWs to extract the mean indium content and its spatial distribution within the (In,Ga)As shell of GaAs/(In,Ga)As based core-shell NWs with high precision. For NWs with nominal In content of 15%, the spatial In distribution was rather homogeneous along the six side facets. Due to shadowing, NWs with 25% of In, showed an In content less that by approximately 9% at one of the facets compared to the other five. Finally, NWs with 60% of In exhibit pronounced fluctuations in In fluorescence, both between different sidewall facets and along the length of the NW. These fluctuations are consistent with the formation of (In,Ga)As mounds on the sidewall facets during growth.

- Replicating the experimentally measured RSM of the $2\bar{2}0$ Bragg reflection of a GaAs/In$_{0.15}$Ga$_{0.85}$As/GaAs core-shell NW using a finite element simulation of a NW model with unique diameter and thicknesses of the core and shells, one is able to extract the strain acting on each side facet and edge. In addition, we were able to extract the In content and thickness of each side facet with accuracy of 1% and 2 nm, respectively. Notably, the GaAs core undergoes compression along and perpendicular to the NW growth axis.

- The consistency of the polytype distribution along the growth axes of several individual AlAs/GaAs capped GaAs/(In,Ga)As/GaAs core-shell NWs was revealed by means of SXDM. The growth is initiated by a small segment of the hexagonal WZ polytype; followed by a mixture of ZB, TZB, WZ and defects up to the midsection of the NW; the growth then proceeds with the ZB and TZB polytypes to end up with a droplet-like feature at the NW top which is highly defective. Accessing the optical properties of the same NWs by CL measurements, an enhancement by a factor of up to 80 was correlated with the mixture of polytypes and defects compared to that of pure WZ and ZB.

- We reveal profound changes in the structure and morphology of individual NWs, with a severe impact on the emission properties of embedded core-shell QWs caused by the continuous illumination of the NWs by an X-ray beam focused to sub-micron spot size at an unchanged beam position.

Appendix

Appendix A

Supplementary part of chapter 4

A   Supplement 1: Scanning electron microscopy

In this supplement, scanning electron microscopy (SEM) images showing the morphology and number density of NWs from the three samples are demonstrated.
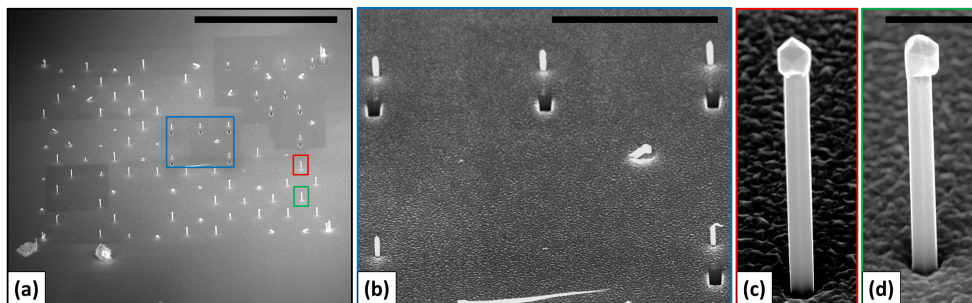
Figure A.1: (a) SEM image of the NW micro field on sample 1 where the nano XRF measurement was performed. The NW density in the inspected region is $0.1/\mu m^2$. The image in (b) is a zoom in of the NW region marked by a blue box in (a) after cutting the upper part of the NWs with the focused ion beam. Micrographs (c) and (d) demonstrate the smooth morphology of two single NWs inside the NW field, marked by red and green boxes in (a), respectively. Scales in (a), (b) and (d) are 50 µm, 10 µm and 1 µm, respectively. (c) and (d) have the same scale.

Figure A.2: (a) SEM image of the NW ensemble on sample 2 where the NW density is $1/\mu$ m^2. (b) and (c) demonstrate the smooth morphology of two randomly selected single NWs. Scale bars in (a) and (c) are 20 µm and 1 µm, respectively. (b) and (c) have the same scale.
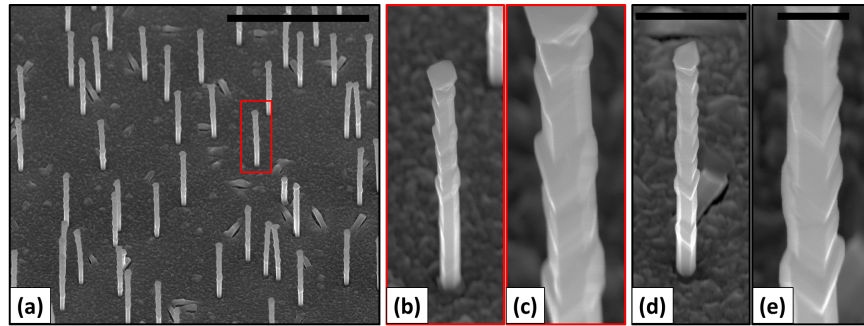
Figure A.3: (a) SEM image of the NW ensemble on sample 3 where the NW density is $1/\mu$ m^2. The images in (b) and (d) demonstrate the morphology of two randomly selected single NWs which is characterized by the presence of mounds. (b) is marked by a red box in (a). The micrographs in (c) and (e) are zoom ins of the rough shell surface of NWs presented in (b) and (d), respectively. Scale bars in (a), (d) and (e) are 5 µm, 1 µm and 250 nm, respectively. (b) and (d), and (c) and (e) have the same scale bars.

B Supplement 2: Comparison of XRF intensities taken from different single NWs.

Here, we present XRF maps of the In distribution of different single NWs measured from samples 1, 2, and 3. The data processing was the same as explained in the main text.
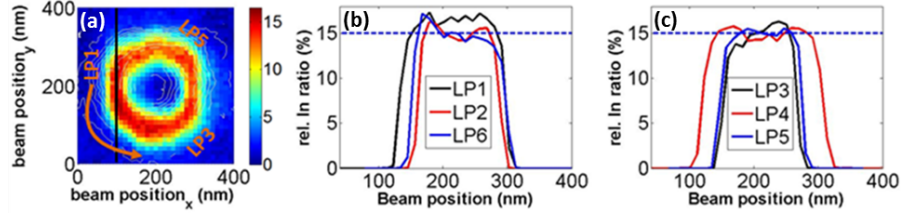
Figure A.4: (a) XRF intensity map of a single NW from sample 1 after correction for the Gaussian beam profile. The six sidewall facets are labelled counter-clockwise by LP1-LP6. The black line indicates for LP1 the central position of a line profile that was extracted and is displayed in (b). For this line profile, the XRF intensity was integrated across the shell thickness. Similar line profiles were extracted for all six facets and are displayed in (b) and (c).
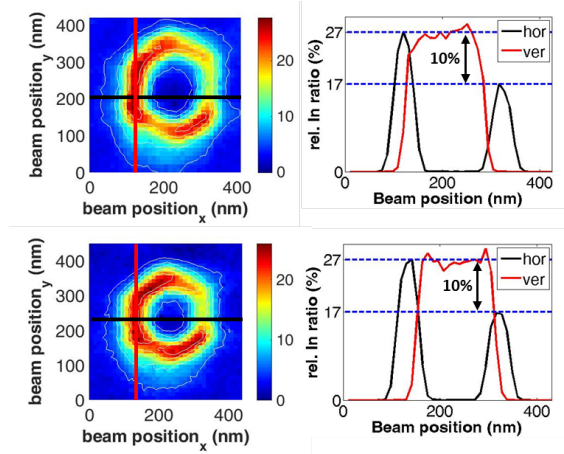
Figure A.5: XRF intensity maps of two single NWs from sample 2 after correction for the Gaussian beam profile. The red and black lines mark the positions of the line scans shown in the diagram, for each NW one line scan parallel to a side facet (red) and one across the NW (black).

Figure A.6: XRF intensity maps of two single NWs from sample 3. Due to the irregular morphology of the NWs on this sample, the signal could not be corrected for the Gaussian beam profile. The dashed lines represent the expected positions of the (In,Ga)As shell. The solid lines indicate the positions of the line scans shown in the diagrams, all across the NW, in the horizontal (black) and vertical (red) direction.

Appendix B

Supplementary part of chapter 5

A   Supplement 1: Other nanowires, in-plane reflections

In addition to NW micro fields (marked by red quadrats), NWs were grown in a single line with separation of 10 µm (Figure S1). This made it possible to access the side facets and edges of single NWs in the GID geometry. The NW orientation with respect to the incident beam direction is indicated, i.e. the incident beam is perpendicular to the NW side facet at $\varphi = 0°$ and to the NW edge at $\varphi = 30°$.
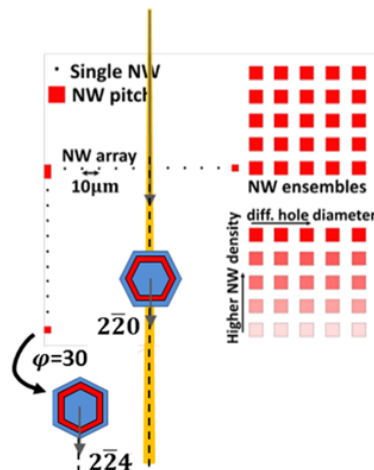
Figure B.1: Top view of the lithography patterned sample mask along the NW orientation when the incident beam is perpendicular to the NW array. Single dots represent positions of single NWs.

Figure B2 illustrates the XRD line profiles VLP1 and DLP1-2, displayed in Figure 4c, achieved by best fit of the FEM model in terms of shell thicknesses. The In content was varied by $\pm 1\%$ from the nominal value of 15%. Both structural parameters are listed on top of each subplot. An increase/decrease in the In content results in widening/shrinkage of the middle peak and an angular shift of the thickness oscillations. Nevertheless, both In contents of 14% and 15% show good agreement with the experimental data demonstrating the limit in the determination of In concentration at given experimental condition.
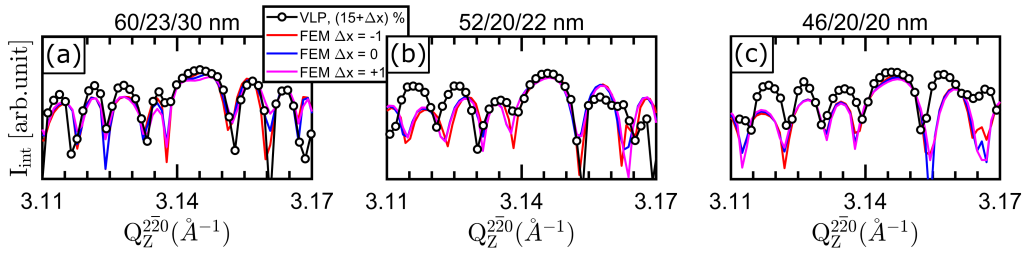
Figure B.2: (a-c) FEM simulations of the three TRs labeled by VLP, DLP1 and DLP2, respectively, in the $2\bar{2}0$ RSM displayed in Figure 4.3a. The thicknesses of core and shells in the FEM simulations are listed on top of each subplot in addition to a variation of $\pm 1\%$ with respect to the 15% nominal In content. The XRD data are labeled in black whereas the FEM simulations are labeled in red.

Left panel of Figure B3 shows the 2D RSM of the $2\bar{2}0$ reflection acquired for NW4 whereas the right panel represents the diffraction pattern of the $22\bar{4}$ Bragg reflection for a NW found outside the NW line shown in figure 4.1a. Both RSMs show similar features compared to the findings of NW2 (Figures 4.3a and 4.3b).
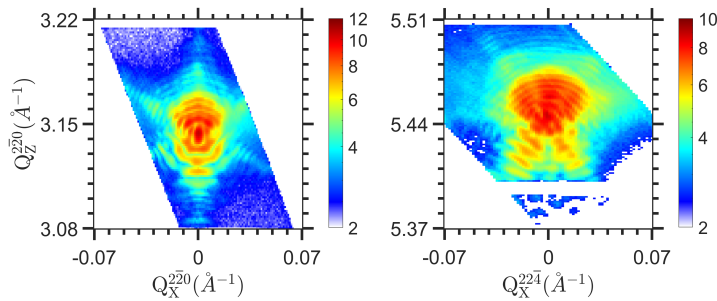

Figure B.3: RSMs of the $2\bar{2}0$ (left) and $22\bar{4}$ (right) Bragg reflections of NWs 4 and 5, respectively.

As mentioned in the manuscript, two approaches can be used to fit the line profiles ex-

tracted from XRD patterns. The RSMs of the $2\bar{2}0$ Bragg reflections of NW2 and NW4
are plotted in Figures 4.6 and B4, respectively. The first approach is to use a distinct
FEM NW model of perfect hexagonal shape to simulate each of the three TRs separately
considering different shell thicknesses. The second approach is to simulate all TRs simul-
taneously using a unique NW model. The results of both approaches are demonstrated by
blue and red lines in Figures 4.6 and B4 b-d, respectively. The fact that both approaches
show good agreement with the experimental line profiles, demonstrates that the strains
acting at the different pairs of opposite side facets are independent from each other. In
contrast to NW2, NW4 displays a perfect hexagonal geometry.
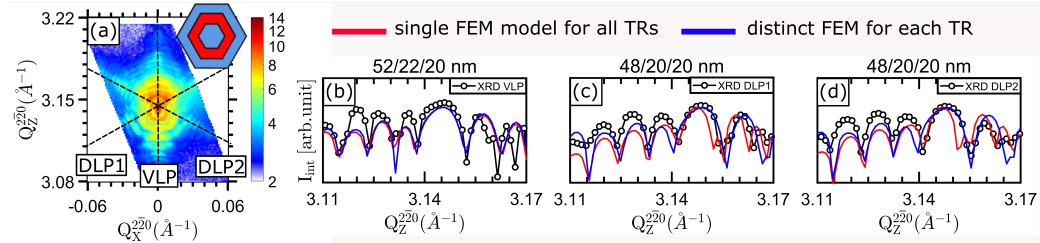
Figure B.4: (a) RSM of the $2\bar{2}0$ Bragg reflection of NW4. On the top right corner,
the predicted NW cross-section is plotted. (b-d) demonstrate FEM simulations and XRD
LPs of VLP, DLP1 and DLP2. FEM simulations of distinct NW models for each TR are
colored in blue whereas FEM LPs extracted from the NW model plotted in (a) are colored
in red. XRD line profiles are colored in black.

Table B.1: Core diamater and shells thicknesses, volume ratios and fitted In content
are shown in the first five rows. The strain values estimated at the centers of the GaAs
core, (In,Ga)As shell and GaAs cap along [111], [$2\bar{2}0$] and [$22\bar{4}$] of NW4 and the strain
gradient at each layer are shown below. Values inside absolute modulus represent the
strain values at each interface of the corresponding shell (see Figure 5b). Both strain
values and gradients have been extracted in the same manner as shown in Table 2 of the
main part of the manuscript.

at center	GaAs core	(In,Ga)As	GaAs cap
VLP1 (nm)	52	22	20
DLP1 (nm)	48	20	20
DLP2 (nm)	48	20	20
In content	—	0.15 ± 0.01	—
Vol. fraction	0.14	0.34	0.52
ϵ_c^{111} (%)	+0.36	-1.41	+0.36
$\epsilon_a^{2\bar{2}0}$ (%)	+0.08	-1.37	-0.27
$\epsilon_b^{22\bar{4}}$ (%)	+0.08	+1.18	-0.29
strain gradients	$|(1) - (2)|$	$|(3) - (4)|$	$|(5) - (6)|$
$\epsilon_a^{2\bar{2}0}$ (%)	0.15 |0.08, -0.07|	0.25 |1.60, 1.35|	0.08 |-0.33, -0.25|
ϵ_b^{22-4} (%)	0.64 |0.08, 0.72|	1.86 |2.1, 0.24|	0.94 |-1, -0.06|

Figure B5 plots the RSM of the $22\bar{4}$ Bragg reflection of NW5. Line profiles, named DLP3-4, indicated by oblique dashed black lines, were extracted along each TR to fit the experimental line profiles shown in Figures S8b and S8c. The best fits were obtained using NW models with thicknesses of 61/21/30 nm and 50/24/30 nm for DLP3 and DLP4, respectively. Based on the $22\bar{4}$ Bragg reflection only, we are not able to fit a complete NW model.
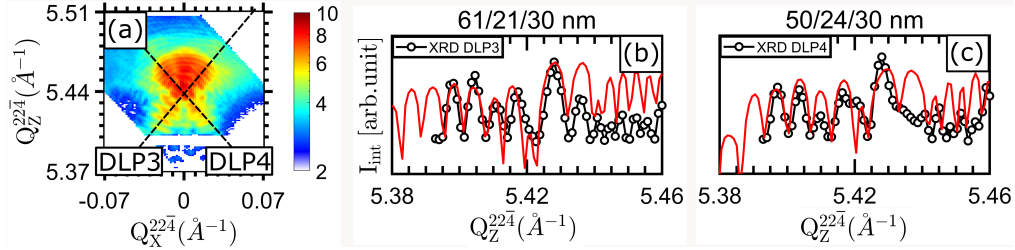

Figure B.5: Panel (a) shows the 2D RSM of the 22-4 Bragg reflection from NW5. (b) and (c) FEM simulations and XRD LPs colored by red and black, respectively, and named DLP3 and DLP4 in (a). The structural parameters of the used FEM NW model are mentioned at the top left corners of subplots (b) and (c).

Appendix C

Supplementary part of chapter 7

A   Supplement 1: Exposed nanowires

In total, 12 NWs were exposed by the X-rays for different intervals of time. NWs 1, 3 and 11 were exposed for 1h; NW6 for 2h; NWs 8, 10 and 12 for 3h; NWs 2 and 7 for 4h; And NW9 for 5h. The length, diameter and tilt of each NW were estimated by SEM before and after exposure whereas the optical emission was acquired by CL (see Table C.1).

Table C.1: Length, diameter, tilt and CL of 12 NWs before and after the exposure experiment.

	Length (µm)		Diameter (nm)		Tilt (^{o})		CL, λ (nm)	
	Before	After	Before	After	Before	After	Before	After
NW1	2.5	2.7	150	210	89.6	90	990+995	990+1000
NW2	2.6	2.1	155	210-480	90.6	93.1	960+1010	none
NW3	2.4	2.6	150	150	87.6	88.4	1000	980+995
NW4	2.6	3.1	150	190-270	89.7	89.7	—	970+1000
NW5	2.5	2.6	155	190-200	89.6	71.6	975+990	1000
NW6	2.3	2.5	150	170-230	90.4	91.7	985+995	none
NW7	2.5	2.8	150	200-300	90	96	980+995	none
NW8	2.8	3.1	160	190-270	89.2	89.7	985+995	985+995
NW9	2.4	2.6	150	190-340	90.3	89	960+990	none
NW10	2.6	2.7	155	190-290	90.3	93.8	980+995	none
NW11	2.6	2.8	160	160-240	91.3	93	980+1000	990+1010
NW12	2.4	1.6	150	210-370	90.8	67	985+995	none

NW1 was exposed by X-rays for 1 hour. The RSMs shown in Figure C.1 show a variation of the Bragg peak only along Q_Y^{111}. Similar to NW2, the main peak splits into 2 sub-peak P (peak) and T (tail). This behavior indicates that NW1 does not undergo any thermal expansion and moreover tilts only in one direction perpendicular to the [111] growth direction. Quantitatively, after exposure, the NW tilts by 0.4^o to 0.6^o from the initial orientation (Figure C.2).
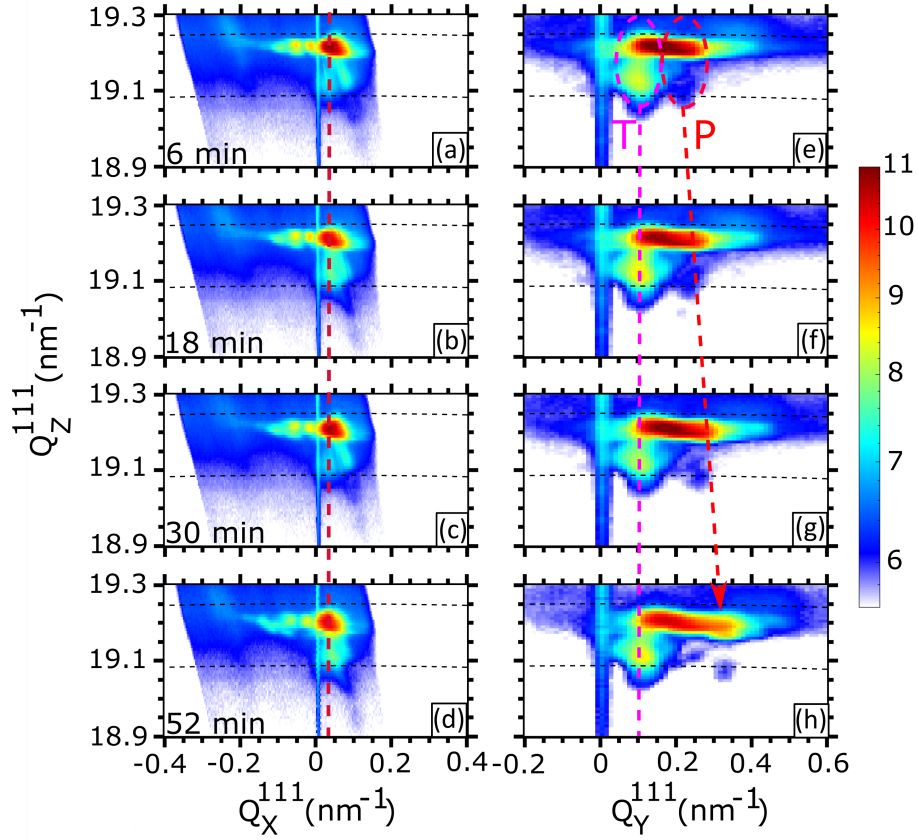

Figure C.1: (a-d) RSMs in the (Q_Z^{111},Q_X^{111}) plane of NW1 during exposure. (e-h) RSMs in the (Q_Z^{111},Q_Y^{111}) plane during exposure. The time at which the RSM acquisition was started is mentioned at the bottom left corner of each sub-plot. The pink dotted lines indicate the non-varied positions of T in Q_X^{111} (a-d) and Q_Y^{111}, (e-h) whereas the red dashed arrow indicates the variation of P in Q_Y^{111} (e-h).

Figure C.2: Tilt calculation of P and T (Q_Y^{111} direction), as well as in Q_X^{111} direction, calculated from the RSMs in Figure C.2.

NW12 was 2.4 μm in length before exposure with pronounced side facets (Figure C.3a). After being exposed by the X-ray beam for 3 hours, the NW shows severe damage described by heavy tilting of approximately 23° and melting down of about 800 nm from the top section (Figure C.3c). The damage and trace of the X-ray beam on the substrate can be clearly seen in Figure C.3b.
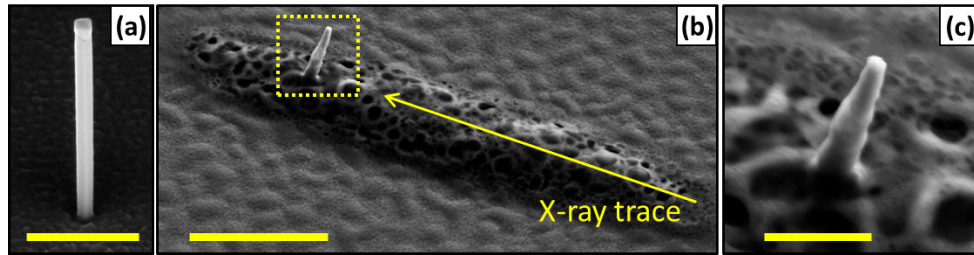

Figure C.3: (a) SEM micrograph of NW12 before exposure. (b) NW 12 after exposure. The yellow arrow indicates the trace of the X-ray beam on the substrate. (c) Zoom in of the area marked by a yellow box in (b).

B Supplement 2: Absorbed dose calculation

As shown in the main text, the structural changes within single NWs were monitored and displayed as a function of exposure time (h) and absorbed dose rate (Gy). In order to

calculate the absorbed dose, first the cross-section of the experimentally used Gaussian nano-focused beam was reconstructed knowing that the total photon flux is 10^{10} s^{-1} and that the vertical and horizontal full width at half maxima of the beam are 600 nm and 1800 nm, respectively. Second, a single NW with nominal height of 2 μm and diameter of 150 nm was created and convoluted with the Gaussian beam (Figure C.4a). The simulation considers a possible misalignment of the NW with respect to the beam during the experiment.
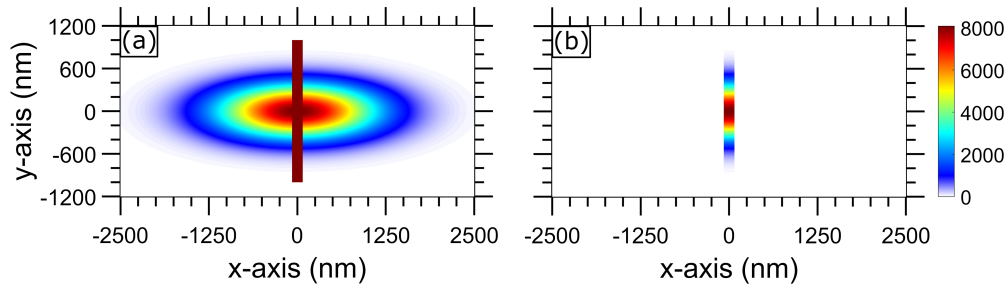
Figure C.4: The reconstructed Gaussian beam aligned to the center of a NW with nominal height of 2000 nm and diameter of 150 nm. (b) The number of photons illuminating the NW if the Gaussian beam hits the center of the NW.

Integrating the signal in Figure C.4b, the photon flux that illuminates the NW (F^{ill}) is calculated to be 5.94 Œ 10^8 s^{-1}. The dose is measured in Gray (J/kg), requiring the NW mass in kilogram and the deposited energy in Joule as input.

The total flux that hits the NW expressed in units of Joule is,

$$F^{tot} = F^{ill}1.610^{-19}J = 9.5010^{-11}J/s \tag{C.1}$$

Considering the nominal NW thickness of 150 nm and a height of 600 nm, given by the vertical full width at half maximum of the beam, the illuminated NW volume (V^{ill}) is calculated to be 1.17 Œ 10^7 nm^3. The mass, M, of the NW is calculated using V^{ill} and the density of GaAs (ρ^{GaAs}) by,

$$M = V^{ill}\rho^{GaAs} = 6.2210^{-17}kg \tag{C.2}$$

The dose rate per second (D_0) that hits the NW is defined as,

$$D_0 = F^{tot}/M = 1.5310^6 Gy/s \tag{C.3}$$

The dose rate absorbed by the NW requires the NW thickness, T, which is chosen to be the nominal NW diameter of 150 nm, and the linear absorption coefficient, μ, which is 3.37 Œ 10^{-5} nm^{-1}. Using these parameters, the absorbed dose rate per second (D_A) and the transmitted dose rate per second (D_T) can be calculated using equations C.4 and C.5,

$$D_A = D_0(1 - e^{-\mu T}) = 7.7112 10^3 \text{Gy/s} \tag{C.4}$$

$$D_T = D_0 e^{-\mu T} = 1.5206 10^6 \text{Gy/s} \tag{C.5}$$

Bibliography

[1] F. Bechstedt and A. Belabbes. *J. Phys.: Condens. Matter*, 25:273201 (27pp), 2013.

[2] A. Belabbes, C. Panse, J. Furthmüller, and F. Bechstedt. *PHYSICAL REVIEW B*, 86:075208, 2012.

[3] P. Caroff, K. A. Dick, M. E. Messing J. Johansson, K. Deppert, and L. Samuelson. *Nature Nanotechnology*, 4:50–55, 2009.

[4] S. Lehmann, D. Jacobsson, and K. A. Dick. *Nanotechnology*, 26:301001, 2015.

[5] S. Lehmann, J. Wallentin, D. Jacobsson K. Deppert, and K. A. Dick. *Nano Lett.*, 13:4099–4105, 2013.

[6] H. J. Joyce, J. Wong-Leung, Q. Gao, H. Hoe Tan, and C. Jagadish. *Nano Lett.*, 10:908915, 2010.

[7] Z. Lu, Z. Zhang, P. Chen, S. Shi, L. Yao, C. Zhou, X. Zhou, and W. Lu. *Applied Physics Letters*, 105:162102, 2014.

[8] D. L. Dheeraj, A. M. Munshi, M. Scheffler, A. T. J. van Helvoort, H. Weman, and B. O. Fimland. *Nanotechnology*, 24:015601 (8pp), 2013.

[9] D. Jacobsson, F. Panciera, J. Tersoff, M. C. Reuter, S. Lehmann, S. Hogmann, K. A. Dick, and F. M. Ross. *Nature*, 531:317, 2016.

[10] Y.-C. Chou, K. Hillerich, J. Tersoff, M. C. Reuter, K. A. Dick, and F. M. Ross. *Science*, 343:218, 2014.

[11] V. G. Dubrovskii, G. E. Cirlin, N. V. Sibirev, F. Jabeen, J. C. Harmand, and P. Werner. *Nano Lett.*, 11:1247–1253, 2011.

[12] F. Glas, J. C. Harmand, and G. Patriarche. *Physical Review Materials*, 99:146101, 2007.

[13] V. Zannier, D. Ercolani, U. P. Gomes, J. David, M. Gemmi, V. G. Dubrovskii, and L. Sorba. *Nano Lett.*, 16:7183, 2016.

[14] A. AlHassan, A. Davtyan, H. Küpers, R. B. Lewis, D. Bahrami, F. Bertram, G. Bussone, C. Richter, L. Geelhaar, and U. Pietsch. *Journal of Applied Crystallography*, 51(1387-1395), 2018.

[15] E. Dimakis, U. Jahn, M. Ramsteiner, A. Tahraoui, J. Grandal, X. Kong, O. Marquardt, A. Trampert, H. Riechert, and L. Geelhaar. *Nano Lett.*, 14(2604), 2014.

[16] G. Patriarche, F. Glas, M. Tchernycheva, C. Sartel, L. Largeau, and J-C Harmand. *Nano Lett.*, 8, 2008.

[17] J. Grandal, M. Wu, X. Kong, M. Hanke, E. Dimakis, L. Geelhaar, H. Riechert, and A. Trampert. *Appl. Phys. Lett.*, 105(121602), 2014.

[18] K. Tomioka, M. Yoshimura, and T. Fukui. *Nature*, 488(189), 2012.

[19] M. O. Hill, I. Calvo-Almazan, M. Allain, M. V. Holt, A. Ulvestad, J. Treu, G. Koblmüller, C. Huang, X. Huang, H. Yan, E. Nazaretski, Y. S. Chu, G. B. Stephenson, V. Chamard, L. J. Lauhon, and S. O. Hruszkewycz. *Nano Lett.*, 18(811819), 2018.

[20] A. Davtyan, T. Krause, D. Kriegner, A. Al Hassan, D. Bahrami, S M Mostafavi Kashani, R. B. Lewis, H. Küpers, A. Tahraoui, L. Geelhaar, M. Hanke, S. Leake, O. Loffeld, and U. Pietsch. *Journal of Applied Crystallography*, 50, 2017.

[21] Y. Zhang, H. A. Fonseka, M. Aagesen, J. A. Gott, A. M. Sanchez, J. Wu, D. Kim, P. Jurczak, S. Huo, and H. Liu. *Nano Lett.*, 17:49464950, 2017.

[22] H. Shtrikman, R. Popovitz-Biro, A. Kretinin, and M. Heiblum. *Nano Lett.*, 9, 2009.

[23] S. G. Ghalamestani, M. Heurlin, L.-E Wernersson, S. Lehmann, and K. A. Dick. *Nanotechnology*, 23:285601 (9pp), 2012.

[24] P. K. Mohseni and R. R. LaPierre. *Nanotechnology*, 20:025610, 2009.

[25] A. Davtyan, S. Lehmann, D. Kriegner, R. R. Zamani, K. A. Dick, D. Bahrami, A. AlHassan, S. J. Leake, U. Pietsch, and V. Holý. *J. Synchrotron Radiation*, 24(Pt 5):981–990, 2017.

[26] R. E. Algra, M. A. Verheijen, M. T. Borgström, L.-F. Feiner, G. Immink, P. van Enckevort, E. Vlieg, and E. P. A. M. Bakkers. *Nature*, 456, 20, 2008.

[27] Th. Kehagias, N. Florini, J. Kioseoglou, Th. Pavloudis, Ph. Komninou, T. Walther, K. Moratis, Z. Hatzopoulos, and N. T. Pelekanos. *Semicond. Sci. Technol.*, 30:114012, 2015.

[28] D. Kriegner, C. Panse, B. Mandl, K. A. Dick, M. Keplinger, J. M. Persson, P. Caroff, D. Ercolani, L. Sorba, F. Bechstedt, J. Stangl, and G. Bauer. *Nano Lett.*, 11:14831489, 2011.

[29] J. Johansson J. Bolinsson, M. Ek, P. Caroff, and K. A. Dick. *ACS Nano*, 6:61426149, 2012.

[30] M. J. L. Sourribes, I. Isakov, M. Panfilova, H. Liu, and P. A. Warburton. *Nano Lett.*, 14:1643–1650, 2014.

[31] R. S. Wagner and W. C. Ellis. *Appl. Phys. Lett.*, 4(89), 1964.

[32] H. Küpers, A. Tahraoui, R.B. Lewis, S. Rauwerdink, M. Matalla, O. Krüger, F. Bastiman, H. Riechert, and L. Geelhaar. *Semicond. Sci. Technol.*, 32(115003), 2017.

[33] H. Küpers, R. B. Lewis, A. Tahraoui, M. Matalla, O. Krüger, F. Bastiman, H. Riechert, and L. Geelhaar. *Nano Res.*, pages 1–9, 2018.

[34] H. Küpers, P. Corfdir, R. B. Lewis, T. Flissikowski, A. Tahraoui, H. T. Grahn, O. Brandt, and L. Geelhaar. *Phys. Status Solidi RRL*, (1800527), 2019.

[35] M. Kriz, S. Lancaster, D. MacFarland, M. Schinnerl, T. Zederbauer, A. Maxwell Andrews, W. Schrenk, and G. Strasser. *Journal of Vacuum Science and Technology B*, 35, 2017.

[36] H. Detz, M. Kriz, S. Lancaster, D. MacFarland, M. Schinnerl, T. Zederbauer, A. Maxwell Andrews, W. Schrenk, and G. Strasser. *Journal of Vacuum Science and Technology B, Nanotechnology and Microelectronics: Materials, Processing, Measurement, and Phenomena*, 35:011803, 2017.

[37] A. B. Mosberg, S. Myklebost, D. Ren, H. Weman, B. O. Fimland, and A. T. J. van Helvoort. *Journal of Physics: Conference Series*, 902:012020, 2017.

[38] K. L. Kavanagh, I. Saveliev, M. Blumin, G. Swadener, and H. E. Ruda. *J. Appl. Phys.*, 111(044301), 2012.

[39] S. J. Leake, V. Favre-Nicolin, E. Zatterin, M-I. Richard, S. Fernandez, G. Chahine, T. Zhou, P. Boesecke, H. Djazouli, and T. U. Schülli. *Materials & Design*, 119:470–471, 2017.

[40] G. Martínez-Criado, J. Villanova, R. Tucoulou, D. Salomon, J. P. Suuronen, S. Labouré, C. Guilloud, V. Valls, R. Barrett, E. Gagliardini, Y. Dabin, R. Baker, S. Bohic, C. Cohen, and J. Morse. *J. Synchrotron Radiat.*, 23(344), 2016.

[41] P. Boye, J. Feldkamp, J. Patommel, A. Schwab, S. Stephan, R. Hoppe, C. Schroer, M. Burghammer, C. Riekel, A. van der Hart, and M. Küchler. *Journal of Physics: Conference Series*, 186:012063, 2009.

[42] O. J. L. Fox, L. Alianelli, A. M. Malik, I. Pape, P. W. May, and K. J. S. Sawhney. *Opt. Express*, 22(7):7657–7668, 2014.

[43] L. Alianelli, K. J. S. Sawhney, R. Barrett, I. Pape, A. Malik, and M. C. Wilson. *Opt. Express*, 19(12):11120–11127, 2011.

[44] J. Grönqvist, N. Søndergaard, F. Boxberg, T. Guhr, S. óAberg, and H. Q. Xu. *J. Appl. Phys.*, 106(053508), 2009.

[45] O. Salehzadeh, K. L.Kavanagh, and S. P.Watkins. *J. Appl. Phys.*, 114(054301), 2013.

[46] Physical properties of semiconductors. `www.ioffe.ru/sva/nsm/semicond/`. Accessed: 09-06-2018.

[47] U. Pietsch, V. Holy, and T. Baumbach. *High resolution x-ray scattering: from thin films and multilayers*. Springer Verlag, New York., 2004.

[48] T. W.Victor, L. M. Easthon, M. Ge, K. H. OToole, R. J. Smith, X. Huang, H. Yan, K. N. Allen, Y. S. Chu, and L. M. Miller. *Scientific Reports*, 8:13415, 2018.

[49] P. M. Kopittke, T. Punshon, D. J. Paterson, R. V. Tapper, P. Wang, F. Pax C. Blamey, A. van der Ent, and E. Lombih. *Plant Physiol.*, 178, 2018.

[50] T. Punshon, M. Lou Guerinot, and A. Lanzirotti. *Annals of Botany*, 103:665672, 2009.

[51] G. A. Chahine, M.-I. Richard, R. A. Homs-Regojo, T. N. Tran-Caliste, D. Carbone, V. L. R. Jaques, R. Grifone, P. Boesecke, J. Katzer, I. Costina, H. Djazouli, T. Schroeder, and T. U. Schülli. *Journal of Applied Crystallography*, 47:762–769, 2014.

[52] P. G. Evans, D. E. Savage, J. R. Prance, C. B. Simmons, M. G. Lagally, S. N. Coppersmith, M. A. Eriksson, and T. U. Schülli. *Adv. Mater.*, 24:5217–5221, 2012.

[53] U. Jahn, J. Lahnemann, C. Pfüller, O. Brandt, S. Breuer, B. Jenichen, M. Ramsteiner, L. Geelhaar, , and H. Riechert. *Physical Review B*, 85(045323), 2012.

[54] T. B. Hoang, A. F. Moses, H. L. Zhou, D. L. Dheeraj, B. O. Fimland, and H. Weman. *Appl. Phys. Lett.*, 94(133105), 2009.

[55] Z. Zanolli, F. Fuchs, J. Furthmüller, U. von Barth, and F. Bechstedt. *Phys. Rev. B*, 75, 2007.

[56] M. Heiss, Y. Fontana, A. Gustafsson, G. Wüst, C. Magen, D. D. ORegan, J. W. Luo, B. Ketterer, S. Conesa-Boj, A. V. Kuhlmann, J. Houel, E. Russo-Averchi, J. R. Morante, M. Cantoni, N. Marzari, J. Arbiol, A. Zunger, R. J. Warburton, and A. Fontcuberta i Morral. *Nature Materials*, 12, 2013.

[57] Anders Gustafsson, Jessica Bolinsson, Martin Ek, and Lars Samuelson. *Journal of Physics: Conference Series*, 326:012042, 2011.

[58] J. Bolinsson, M. Ek, J. Trägårdh, K. Mergenthaler, D. Jacobsson, M.-E. Pistol, L. Samuelson, and A. Gustafsson. *Nano Research*, 7(4):473490, 2014.

[59] S. Biswas, J. Doherty, D. Saladukha, Q. Ramasse, D. Majumdar, M. Upmanyu, A. Singha, T. Ochalski, M. A. Morris, and J. D. Holmes. *Nat. Commun.*, 7(11405), 2016.

[60] H. Potts, M. Friedl, F. Amaduzzi, K. Tang, G. Tütüncüoglu, F. Matteini, E. A. Lladó, P. C. McIntyre, , and A. Fontcuberta i Morral. *Nano Lett.*, 16(637), 2016.

[61] K. Wei Ng, W. Son Ko, R. Chen, F. Lu, T.-T. D. Tran, K. Li, and C. Chang-Hasnain. *J. ACS Appl. Mater. Interfaces*, 6(16706), 2014.

[62] J. Treu, M. Bormann, H. Schmeiduch, M. Döblinger, S. Morkötter, S. Matich, P.Wiecha, K. Saller, B.Mayer, M.Bichler, M. C. Amann, J. J. Finley, G. Abstreiter, and G. Koblmüller. *Nano Lett.*, 13(6070), 2013.

[63] M. Keplinger, Th. Mårtensson, J. Stangl, E. Wintersberger, B. Mandl, D. Kriegner, V. Holý, G. Bauer, K. Deppert, and L. Samuelson. *Nano Lett.*, 9(1877), 2009.

[64] G. E. Ice, J. D. Budai, and J. W. L. Pang. *Science*, 334(1234), 2011.

[65] J. Segura-Ruiz, G. Martínez-Criado, C. Denker, J. Malindretos, and A. Rizzi. *Nano Lett.*, 14(1300), 2014.

[66] G. Martínez-Criado, A. Homs, B. Alén, J. A. Sans, J. Segura-Ruiz, A. Molina-Sánchez, J. Susini, J. Yoo, and 5829 (2012). G.-C. Yi, Nano Lett. 12. *Nano Lett.*, 12(5829), 2012.

[67] J. Wallentin, D. Jacobsson, M. Osterhoff, M. T. Borgström, and 4143 (2017). T. Salditt, Nano Lett. 17. *Nano Lett.*, 17(4143), 2017.

[68] D. Dzhigaev, T. Stankevič, Z. Bi, S. Lazarev, M. Rose, A. Shabalin, J. Reinhardt, A. Mikkelsen, L. Samuelson, G. Falkenberg, R. Feidenhansl, , and I. A. Vartanyants. *ACS Nano*, 11(6605), 2017.

[69] I. Giuntoni, L. Geelhaar, J. Bruns, and H. Riechert. *Opt. Express*, 24(18417), 2016.

[70] G. Bussone, H. Schäfer-Eberwein, E. Dimakis, A. Biermanns, D. Carbone, A. Tahraoui, L. Geelhaar, P. H. Bolívar, T. Schülli, and U. Pietsch. *Nano Lett.*, 15(981), 2015.

[71] R. B. Lewis, L. Nicolai, H. Küpers, M. Ramsteiner, A. Trampert, and L. Geelhaar. *Nano Lett.*, 17(136), 2017.

[72] V. Solé, E. Papillon, M. Cotte, P. Walter, and J. Susini. *Spectrochim. Acta, Part B*, 62(63), 2007.

[73] T. Stankevič, S. Mickevicius, M. S. Nielsen, O. Kryliouk, R. Ciechonski, G. Vescovi, Z. Bi, A. Mikkelsen, L. Samuelson, C. Gundlach, and R. Feidenhansl. *J. Appl. Crystallogr.*, 48(344), 2015.

[74] A. AlHassan, R. B. Lewis, H. Küpers, W.-H. Lin, D. Bahrami, T. Krause, D. Salomon, A. Tahraoui, M. Hanke, L. Geelhaar, and U. Pietsch. *PHYSICAL REVIEW MATERIALS*, 2(014604), 2018.

[75] T. Krause, M. Hanke, L. Nicolai, Z. Cheng, M. Niehle, and A. Trampert. *PHYS. REV. APPLIED*, 7(024033), 2017.

[76] F. Lenrick, M. Ek, D. Jacobsson, M. T. Borgström, and L. R. Wallenberg. *Microsc. Microanal.*, 20:133140, 2014.

[77] D. C. Watson, R. V. Martinez, Y. Fontana, E. Russo-Averchi, M. Heiss, A. Fontcuberta i Moral, G. M. Whitesides, and M. Lončař. *Nano Lett.*, 14(524-531), 2014.

[78] X. Dai, A. Messanvi, H. Zhang, C. Durand, J. Eymery, C. Bougerol, F. H. Julien, and M. Tchernycheva. *Nano Lett.*, 15(6958), 2015.

[79] Y.-W. Lan, W.-H. Chang, Y.-C-Chang, C.-S. Chang, and C.-D. Chen. *Nanotechnology*, 26(055705), 2015.

[80] H. Bender, A. Franquet, C. Drijbooms, B. Parmentier, T. Clarysse, W. Vandervorst, and L. Kwakman. *Semicond. Sci. Technol.*, 30(114015), 2015.

[81] M. Heiss, S. Conesa-Boj, J. Ren, H.-H. Tseng, A. Gali, A. Rudolph, E. Uccelli, F. Peiró, J. R. Morante, D. Schuh, E. Reiger, E. Kaxiras, J. Arbiol, and A. Fontcuberta i Morral. *Phys. Rev. B*, 83(045303), 2011.

[82] X. Yan, X. Zhang, J. Li, Y. Wu, J. Cui, and X. Ren. *Nanoscale*, 7(1110), 2015.

[83] L. Ahtapodov, J. Todorovic, P. Olk, T. Mjåland, P. Slåttnes, D. L. Dheeraj, A. T. J. van Helvoort, B.-O. Fimland, and H. Weman. *Nano Lett.*, 12(6090-5), 2012.

[84] L. Rigutti, G. Jacopin, L. Largeau, E. Galopin, A. De Luna Bugallo, F. Julien, J.-C. Harmand, F. Glas, and M. Tchernycheva (2011). Phys. Rev. B 83 155320. *hys. Rev. B*, 83(155320), 2011.

[85] A. Biermanns, A. Davydok, H. Paetzelt, A. Diaz, V. Gottschalch, T. H. Metzger, and U. Pietsch. *Journal of Synchrotron Radiation*, 16(6):796–802, 2009.

[86] O. H. Seeck, C. Deiter, K. Pflaum, F. Bertam, A. Beerlink, H. Franz, J. Horbach, H. Schulte-Schrepping, B. M. Murphy, M. Greveb, and O. Magnussenb. *J. Synchrotron Rad.*, 19:30–38, 2012.

[87] I. A. Vartanyants and I. K. Robinson. *Journal of Physics: Condensed Matter*, 13(10593), 2001.

[88] J. Johansson and K. A. Dick. *CrystEngComm*, 13(7175), 2011.

[89] Q. Zhang, P. W. Voorhees, and S. H. Davis. *J. Nanotechnol.*, 8:506513, 2017.

[90] L. Mancini, Y. Fontana, S. Conesa-Boj, I. Blum, F. Vurpillot, L. Francaviglia, E. Russo-Averchi, M. Heiss, J. Arbiol, A. Fontcuberta i Morral, and L. Rigutti. *Applied Physics Letters*, 105(243106), 2014.

[91] L. Balaghi, G. Bussone, R. Grifone, R. Hübner, J. Grenzer, M. Ghorbani-Asl, A. Krasheninnikov, H. Schneider, M. Helm, and E. Dimakis. *private communications*, 2018.

[92] P. Schroth, J. Jakob, L. Feigl, S. Kashani, U. Pietsch, and T. Baumbach. *MRS Communications*, 8(3):871–877, 2018.

[93] A. Davtyan, A. Biermanns, O. Loffeld, and U. Pietsch. *New J. Phys.*, 18:063021, 2016.

[94] A. Dobrovolsky, P. O. Å. Persson, S. Sukrittanon, Y. Kuang, C. W. Tu, W. M. Chen, and I. A. Buyanova. *Nano Lett.*, 15(40524058), 2015.

[95] J. Bao, D. C. Bell, and F. Capasso. *Nano Lett.*, 8:836841, 2008.

[96] R. L. Woo, R. Xiao, Y. Kobayashi, L. Gao, N. Goel, M. K. Hudait, T. E. Mallouk, and R. F. Hicks. *Nano Lett.*, 8:46644669, 2008.

[97] D. Spirkoska, J. Arbiol, A. Gustafsson, S. Conesa-Boj, F. Glas, I. Zardo, M. Heigoldt, M. H. Gass, A. L. Bleloch, S. Estrade, M. Kaniber, J. Rossler, F. Peiro, J. R. Morante, G. Abstreiter, L. Samuelson, and A. Fontcuberta i Morral. *Phys. Rev. B*, 80:245325, 2009.

[98] P. Krogstrup, H. I. Jørgensen, M. Heiss, O. Demichel, J. V. Holm, M. Aagesen, J. Nygard, and A. Fontcuberta i Morral. *Nat. Photonics*, 7(306), 2013.

[99] J. Lähnemann, M. O. Hill, J. Herranz, O. Marquardt, G. Gao, A. Al Hassan, A. Davtyan, S. O. Hruszkewycz, M. V. Holt, C. Huang, I. Calvo-Almazan, U. Jahn, U. Pietsch, L. J. Lauhon, and L. Geelhaar. *Nano lett.*, 2019.

[100] L. J. Lauhon, M. S. Gudiksen, C. L. Wang, and 57. C. M. Lieber, (2002). 420 (6911). *Nature*, 420(6911):57, 2002.

[101] A. Senichev, P. Corfdir, O. Brandt, M. Ramsteiner, S. Breuer, J. Schilling, L. Geelhaar, and P. Werner. *Nano Res.*, 11:4708, 2018.

[102] A. Biermanns, T. Rieger, G. Bussone, U. Pietsch, D. Grützmacher, and M. I. Lepsa. *Appl. Phys. Lett.*, 102(4):043109, 2013.

[103] X. Shi, G. Xiong, X. Huang, R. Harder, and I. Robinson. *New Journal of Physics*, 14:063029 (13pp), 2012.

[104] S. M. Polvino, C. E. Murray, Ö. Kalenci, I. C. Noyan, B. Lai, and Z. Cai. *Applied Physics Letters*, 92:224105, 2008.

[105] F. De la Pena. *HyperSpy*, 1.3, 2018.

[106] R. K. Hart, T. F. Kassner, and J. K. Maurin. *Phil. Mag.*, 21:467, 1970.

[107] J. T. Fourie. *Optik*, 65:9195, 1978.

[108] H. J. Hagemann, W. Gudat, and C. Kunz. *J. Opt. Soc. Am.*, 52:7424, 1975.

[109] S. M. Mominuzzaman, K. M. Krishna, T. Soga, T. Jimbo, and M. Umeno. *Japan. J. Appl. Phys.*, 38:65863, 1999.

[110] O. Demichel, M. Heiss, J. Bleuse, H. Mariette, and A. Fontcuberta i Morral. *Appl. Phys. Lett.*, 97(201907), 2010.

[111] J. Lähnemann, T. Flissikowski, M. Wölz, L. Geelhaar, H. T. Grahn, O. Brandt, and U. Jahn. *Nanotechnology*, 27:455706, 2016.

[112] T. Rieger, M. I. Lepsa, T. Schäpers, and D. Grützmacher. *Journal of Crystal Growth*, 378:506–510, 2013.

[113] Z. Y. Zhou, C. X. Zheng, W. X. Tang, D. E. Jesson, and J. Tersoff. *App. Phy. Lett.*, 97:121912, 2010.

[114] T. E. Haynes, W. K. Chu, T. L. Aselage, and S. T. Picraux. *J. Appl. Phys.*, 63:1168, 1988.

[115] P. Smolyanskiy, B. Bergmann, G. Chelkov, S. Kotov, U. Kruchonak, D. Kozhevnikov, Y. Mora Sierra, I. Stekl, and A. Zhemchugov. *JINST*, 13:T02005, 2018.

[116] G. Lioliou and A. M. Barnett. *Nuclear Instruments and Methods in Physics Research A*, 836:T3745, 2016.

[117] S. P. Hau-Riege. *High-Intensity X-Rays - Interaction with Matter: Processes in Plasmas, Clusters, Molecules and Solids.* Willey-VCH Verlag, Weinheim, Germany,, 2011.

[118] N. Medvedev, Z. Li, and B. Ziaja. *Phys. Rev. B*, 91:054113, 2015.

[119] N. Medvedev, Z. Fang, C. Xia, and Z. Li. *Phys. Rev. B*, 99:144101, 2019.

[120] V. Tkachenko, N. Medvedev, Z. Li, P. Piekarz, and B. Ziaja. *Phys. Rev. B*, 93:144101, 2016.

[121] D. Cui, D. Pavlidis, and A. Eisenbach. *Conference Proceedings. International Conference on Indium Phosphide and Related Materials*, pages 526–529, 2000.

[122] W. Li and M. Pessa. *Physical Review B*, 57:23, 1998.

[123] W. E. Hoke, P. J. Lemonias, D. G. Weir, H. T. Hendriks, and G. S. Jackson. *J. Appl. Phys.*, 69, 1991.

Acknowledgments

"I've learned through the years that it's not where you live, it's the people who surround you that make you feel at home." - J.B. McGee

- First of all, I would like to express my gratitude and appreciation to my instructor, Professor Dr. Ullrich Pietsch (Ulli), for his continuous scientific and financial support throughout my studies. Most of all, thank you for accepting me as a member of your group. It was nothing but a pleasure working under your supervision and hopefully I have reached your expectations.

- To Professor Dr. Olivier Thomas, Professor Dr. Carsten Busse and Professor Dr. Markus Risse, for accepting my invitation to take part in my defense review committee.

- To the always forgotten, our beloved secretary, Kerstin Semma, thank you for all the help with the paper work and for always answering my mistakes with a smile.

- To my colleagues and very good friends, Dr. Arman Davtyan and Danial Bahrami, thank you for cooperating and joining most of my beam times as well as offering help whenever needed. But most important, thank you for your friendship that will never be forgotten.

- To the beamline scientists who were present and willing to give a hand during experiments I have participated in, Dr. Christian Sternemann (BL9 of DELTA), Dr. Florian Bertram, Dr. Genziana Bussone and Dr. Karthick Perumal (P08 of PETRA III), Dr. Steven Leake, Dr. Carsten Rechter and Dr. Gilbert Chahine (ID01 of ESRF) and Dr. Damian Salomon (ID16b of ESRF).

- To our collaborators, Dr. Lutz Geelhaar, Dr. Ryan B. Lewis, Dr. Hanno Küpers, Dr. Jonas Lähnemann from the Paul-Drude-Institut for the fruitful scientific discussions and for always supplying us with samples. To Dr. Michael Lepsa and Dr.